

# **NASA Contractor Report 3718**

NASA  
CR  
3718  
c.1

## **Toughening Mechanism in Elastomer-Modified Epoxy Resins — Part 1**

**A. F. Yee and R. A. Pearson**

**CONTRACT NAS1-16132  
AUGUST 1983**



25th Anniversary  
1958-1983

**NASA**





## **NASA Contractor Report 3718**

# **Toughening Mechanism in Elastomer-Modified Epoxy Resins — Part 1**

**A. F. Yee and R. A. Pearson**  
*General Electric Company*  
*Schenectady, New York*

**Prepared for**  
**Langley Research Center**  
**under Contract NAS1-16132**



**National Aeronautics  
and Space Administration**

**Scientific and Technical  
Information Branch**

**1983**

## 1. INTRODUCTION

It is well-known that some brittle epoxies can be toughened by an order of magnitude by the addition of a rubbery phase. The purpose of this work is to investigate the micromechanical mechanisms that contribute to the toughness of rubber-modified epoxies. It is hoped that the understanding resulting from this investigation will lead to concepts for optimizing the mechanical properties. In this section some of the proposed theories on toughening mechanisms will be briefly reviewed.

A great deal of controversy still exists on the nature of the toughening mechanisms; much of the dispute surrounds the issues of whether the rubber (1-3) or the matrix (3-11) absorbs most of the energy, and of whether the matrix undergoes massive crazing (4,5,10,11) or simply voiding (3, 6-9). In view of the continued interest on the latter issue and the findings of this investigation, it is appropriate to review the relevant aspects of cavitation processes, viz., crazing and voiding, in polymeric solids. The general subject of cavitation in polymers has been discussed (12,13). Crazing, a very special mode of cavitation, has also been extensively reviewed (14-16).

### 1.1 CRAZING

Crazing usually initiates at an interface. It is sometimes referred to as normal yielding (17), because in isotropic polymers it occurs in planes normal to the major principal tensile stress. A craze is sandwiched by two relatively well-defined, nearly parallel walls of solid polymer material. The craze material can range from ellipsoidal voids separated by thin cell walls, to thin strands of highly drawn fibrils forming a network that spans the two

craze walls. Its exact morphology depends on the type of polymer, the molecular weight, the environment for growth, and the stage of growth. The craze voids range in size from a few to a few tens of nm (18), and constitute 40-60% of the volume of the craze material. A craze is initiated by hydrostatic tension, but grows only with a stress bias.(19) It thickens by drawing strands of material from the craze walls. Thus, on a unit volume basis the growth of a craze absorbs a large amount of energy. Another consequence of the way a craze deforms is that its apparent Poisson's ratio is zero.(20) The arrangement of interconnected voids in a plane also provides a natural path for crack propagation, unless the opening of the craze into a crack is prevented by, say, the presence of a rubber particle. In such a case, the strain energy becomes available for initiating and propagating still more crazes, until fracture finally occurs. This entire process makes possible the toughening mechanism known as massive crazing.(20) The role played by the rubber particle is crucial; to be effective it must be compliant and adhere well to the matrix. The rubber particles must also be at least as large as the thickness of a characteristic craze.(21)

## 1.2 VOIDING

Voiding is also initiated by hydrostatic tension at or in a heterogeneity in the solid. Unlike crazes, voids can grow without a stress bias; they also do not grow preferentially in a plane normal to the major principal tensile stress. Unless the volume fraction of voids becomes very large, voids in a plane do not provide as easy a path for crack propagation as do crazes. In uniaxial plane stress tension, even as the voids grow, the specimen cross-sectional area continues to diminish.(22) If a rubber-modified polymer

deforms by voiding, an important function of the rubber particles is to be the initial void nucleant. To be effective in such a role, the rubber must have substantially different moduli from the matrix, and a sharp interface should presumably exist between the two. What other roles these particles might play is an important question to be addressed by the present investigation.

### 1.3 TOUGHENING THEORIES

General theories on toughening of plastics are discussed by Bucknall.(20) A review of relevant work on epoxies published up to ca. 1978 is contained in the dissertation by Kunz(1). The principal theories, together with some of the more recent findings, are outlined here.

### 1.4 TOUGHENING BY CRAZING

McGarry and co-workers(4,5) found that small ( $<0.1 \mu\text{m}$ ) rubber particles did not toughen epoxies, whereas large ( $1\text{--}22 \mu\text{m}$ ) particles increased the fracture toughness  $G_{Ic}$  by at least an order of magnitude. In studying the biaxial yield behavior of these epoxies, Sultan and McGarry(5) found that the yield criterion could be expressed in a modified von Mises form:

$$\tau_{\text{oct}} = \tau_o - \mu P \quad (1.1)$$

where  $\tau_{\text{oct}}$  is the octahedral shear yield stress,  $\tau_o$  is the intrinsic shear strength of the material,  $P$  is the mean hydrostatic pressure, and  $\mu$  is the pressure coefficient.  $\mu$  is  $\geq 0$  and expresses the sensitivity of the material to the hydrostatic stress component. For an unmodified epoxy and an epoxy modified by a highly soluble carboxyl-terminated butadiene nitrile rubber (CTBN) which resulted in small ( $0.040 \mu\text{m}$ ) particles,  $\mu$  was found to be 0.175.

But for an epoxy modified by a less soluble CTBN rubber, which resulted in large ( $1.2\text{ }\mu\text{m}$ ) particles, two pressure coefficients were necessary to describe the failure locus:  $\mu = .210$  in the first (tension-tension) quadrant, and  $\mu = .175$  in the rest of the stress field. This result, together with the stress whitening observed in the first quadrant, suggested to them that microcavitation taking place at the crack tip was the toughening mechanism. They identified this microcavitation as crazing. This theory was cited by several workers (23,24) to explain the toughness of other rubber-modified epoxy systems. It should be pointed out, as others have (25-27), that stress whitening can be caused by voiding as well as crazing. In the present case, simple voiding of or around the rubber particles would also produce the increased pressure coefficient (larger  $\mu$ ) observed. Studies on other rubber-modified systems show that voiding and crazing result in very similar macroscopic biaxial tensile failure behavior(28). In any case, if the yield behavior observed by Sultan and McGarry is due to crazing, then the Sternstein stress bias criterion(19) would have described the data more closely. The issue here is not whether the correct kind of failure criterion has been used to describe their first quadrant data, but this: if a maximum octahedral shear stress or distortional energy type failure criterion (Eq. 1.1) accurately describes the data, then crazing which requires a hydrostatic component, is unlikely as a major mechanism. Unfortunately, the scatter in the data was such that either of the two criteria mentioned above could describe the first quadrant equally well. The micrographic evidence offered by these workers(4,5,23,24) actually support the idea that simple voiding in or around the rubber particles rather than crazing, was a major deformation mechanism. No concrete evidence for crazing such as unambiguous micrographs or large volume dilatation, was presented.

## 1.5 TOUGHENING BY SHEAR AND CRAZING

Bucknall and co-workers proposed that shear flow and massive crazing are the two energy absorbing mechanisms in rubber-modified plastics(20). They used dilatometry in tensile creep to study these mechanisms in rubber-modified epoxies(10,11). Their technique assumes that shear flow creates no volume change, whereas crazing does. They proposed that the slope of the volume strain  $\frac{\Delta V}{V_0}$  vs. longitudinal strain  $\epsilon_1$  curve equals zero for a pure shear flow process, and equals 1 (one) for a pure crazing process. Intermediate slopes would be produced by proportionate mixing of the two processes, i.e., a rule of mixtures was assumed. These assumptions are not strictly correct because they ignore the Poisson's effect in the linear viscoelastic range,(27) the small but finite contraction of a massively crazed specimen in tension, and the volume increase and subsequent densification in a shear yielding process.(27) These are, however, relatively minor objections compared to the assumption that volume dilatations can be exclusively attributed to crazing. Voiding can also cause volume dilatation.(22) The dilatation behavior of a system that deforms by a combination of small amounts of crazing and large amounts of shear flow is particularly difficult to distinguish from one that voids. In any case Bucknall and Yoshii found that in rubber-modified epoxies volume strain increased with rubber content, as did fracture toughness, and concluded that a combination of shear flow and massive crazing were the toughening mechanisms. They also showed an electron micrograph of a craze in epoxy(11,20).

As previously mentioned, volume dilatation cannot be unambiguously and exclusively attributed to crazing.(25-27) Other types of evidence for massive

crazing must be presented to corroborate the volume strain data. In fact, doubts of the existence of crazes in a tightly cross-linked glassy polymer have been voiced by several authors (1,2,29,30) despite reports of observations.(11,31,32) The real question is not whether or not crazes can exist in cross-linked glassy polymers, but how much they contribute to the toughness of these materials. This subject is another important objective of this investigation.

It has been shown by Bascom and co-workers that plastic zone sizes are directly related to the toughness of rubber-modified epoxy adhesives, and it was proposed that cavitation caused by the triaxial tension ahead of the crack tip increases the size of the plastic zone(3, 6-9). They also proposed, that, in addition to the cavitation, plastic flow of the epoxy matrix and elongation of the particles also contribute to the toughness.(3) Their theory is undoubtedly the most comprehensive one yet proposed. It will be shown later that their theory is qualitatively in accord with the findings of this investigation.

## 1.6 RUBBER STRETCHING AND TEARING

Recently a quantitative theory was advanced by Kunz and Beaumont (1,2), based on the idea that elastic energy stored in the rubber during stretching is dissipated irreversibly when the particles fail. This is the only theory proposed thus far that attributes the toughness enhancement of rubber-modified epoxies entirely to the rubber particles. This quantitative theory can account for an increase of a factor or two in the fracture toughness, which was the amount found by these authors. Unfortunately, others (3-11) have found increases that are an order of magnitude greater. The rubber-modified

epoxies Kunz and Beaumont prepared achieved a level of toughness much lower than that achieved in the present investigation as well as those reported in the literature. The discrepancy in reported toughness values points out a common problem in these materials, i.e., the sensitivity of the material properties to the curing agent and the conditions of curing(33). The large stress-whitened zones reported by all other investigations(3-11, 23,24) strongly suggest that plastic deformation of the matrix must be considered a major contributor to the toughness. Nevertheless, the work by Kunz, et al. has perhaps quantified the order of magnitude of the contribution to toughness from the rubber particles alone. A recent publication by these workers (34) on low temperature results is also considered by these authors to support their theory.

It is clear from the foregoing that the issue of the toughening mechanisms in rubber-modified epoxies is far from settled. Nearly every possible mechanism has been proposed and has found some support. But the debate is important. Once the important mechanisms have been identified, then, presumably, the material parameters responsible for the mechanism can be enhanced or modified to produce an optimal combination of properties. The purpose of this work is to add to the existing data, fill in some of the missing information, and help in elucidating the deformation mechanisms in this complex material.

## 2. EXPERIMENTAL APPROACH

The tensile dilatometric technique used by Bucknall and co-workers(20) is a powerful tool for studying toughening mechanisms, provided that care is taken to (a) distinguish between simple voiding and crazing, (b) properly account for the difference in time scale of the dilatometric and the fracture toughness experiments, and (c) insure that the difference in stress configuration between the tensile and the plane-strain fracture toughness experiments, (i.e., the differences in the magnitudes of the deviatoric and the hydrostatic components) is considered. Tensile dilatometry was used as a major tool in this work. To satisfy condition (a), a combination of scanning (SEM) and transmission (TEM) electron microscopy, optical microscopy (OM), and small angle x-ray scattering (SAXS), was employed to examine the relative importance of simple voiding and crazing mechanisms. For condition (b), the tensile dilatometric experiments were performed in a constant-displacement-rate mode over several decades of rates; furthermore these experiments were carried out at sub- and super- ambient temperatures to extend the equivalent strain-rate range by using the time-temperature equivalence concept. Condition (c) is the most difficult to satisfy because the hydrostatic stress component in a plane-strain fracture experiment is inherently much larger than that in a uniaxial tensile experiment. Fortunately, for systems that fail with extensive inhomogeneous dilatation, the yield stress has relatively little sensitivity to the magnitude of the hydrostatic stress component, as long as the major principal stress is tensile(28) and the dominant mode of deformation does not vary. This line of argument will be examined more closely when the results are presented and discussed in a later section.

The experimental techniques are described in the following section.

## 2.1 FRACTURE TOUGHNESS $G_{Ic}$

Given the well-known batch-to-batch variability of toughness values of cured epoxy materials, it is necessary to ascertain whether material from a given plaque has indeed been properly prepared, i.e., has the correct toughness. For this purpose, it is impractical to use a fracture specimen shape that uses large amounts of materials, such as the double cantilever beam or the compact tension types, because insufficient material would be left over from the typical 250mm x 250mm cast plaques for tensile testing after the fracture specimens has been cut from them. This problem is resolved by using single edge notch (SEN) specimens in three-point bending (3PB). These specimens are small, and several can be obtained from each plaque. The technique of determining  $G_{Ic}$ , the critical energy release rate, from 3PB-SEN specimens by applying linear elastic fracture mechanics has been described in detail by Williams and co-workers(35,36), and by Brown(37). Hence, only an abbreviated account will be given here.

A SEN specimen loaded in 3PB is shown in Figure 1. When a load  $P$  is applied to the specimen, a deflection  $\Delta$  is produced:

$$\Delta = CP \quad (2.1)$$

where  $C$  is the compliance. The stored elastic energy  $U$  is given by:

$$U = \frac{1}{2}P\Delta \quad (2.2)$$

if the load deflection curve appears as in Figure 2. It can be shown(35,36) that the energy change per unit cracked area  $A$  is:

$$\frac{dU}{dA} = \frac{1}{2} P^2 \frac{dC}{dA} \quad (2.3)$$

This is a consequence of the linear elastic assumption. Since the critical strain energy release rate,  $G_{Ic}$ , is the energy released per unit crack area, i.e.,

$$\frac{dU}{dA} = G_{Ic} \quad (2.4)$$

Combining Eqs. 2.1 - 2.4 and rearranging, one gets

$$U = G_{Ic} \left( \frac{C}{dC/dA} \right) \quad (2.5)$$

Thus, in principle,  $G_{Ic}$  can be found from either Eq. 2.4 or 2.5. But, as pointed out by Williams(36), Eq. 2.4 is valid only for stable crack propagation. In the unstable crack propagation case, which is appropriate for most fracture tests in this work, Eq. 2.5 must be used. Thus, a function for the change in compliance with crack area must be found. The term  $\frac{C}{dC/dA}$  in Eq. 2.5 may be rewritten in terms of the geometric parameters B, the specimen width, D, the specimen depth, and X, the ratio of the crack length a to D, i.e.,

$$X = \frac{a}{D}$$

$$\frac{C}{dC/dA} = BD \frac{C}{dC/dX} = BD\Phi \quad (2.6)$$

The function  $\Phi$  has been computed for the Charpy geometry(35). Combining Eq. 2.5 and 2.6, one gets

$$U = G_{Ic} BD\Phi \quad (2.7)$$

Thus,  $G_{Ic}$  can be calculated from tests on specimens with various crack lengths by measuring the fracture energy and using the value of  $\Phi$  for a given

crack length. In these experiments it was found that the experimentally determined compliance function  $\Phi_{exp}$  was considerably different from the theoretical  $\Phi$ , especially at short crack lengths. A comparison of a typical  $\Phi_{exp}$  with the theoretical  $\Phi$  will be shown in a later section. The discrepancy at short crack lengths results in abnormally high  $G_{Ic}$  values if the theoretical  $\Phi$  is used. This situation has not been reported by other workers. All  $G_{Ic}$  values reported here are calculated from  $\Phi_{exp}$ , which is determined by measuring  $C$  for various crack lengths and numerically differentiating a polynomial fitted to the data by computer.

Another problem encountered in these experiments is the dependence of the apparent toughness on the manner that the crack is introduced. Rectangular (11mm x 6mm x 100mm) specimens were cut from the cast epoxy plaques. Each specimen was notched using a jeweler's saw. A crack which appears sharp could be produced by a few taps with a hammer on a fresh razor blade inserted into the cut notch.  $G_{Ic}$  results on the specimens prepared in this manner are abnormally high, especially for the unmodified epoxy. Observation of the initial crack tips in the microscope with polarized light revealed a zone of birefringence ahead of the crack tip. This zone is undoubtedly produced by pressing the razor blade into the material. It was discovered that if the razor blade is first chilled in liquid nitrogen, then very sharp cracks can be formed by the wedging action of the blade. This latter technique does not produce visible birefringence at the crack tips. The dependence of apparent fracture toughness on the manner of crack introduction has been discussed by Cessna and Sternstein(38). It may be one of the causes of variations in the reported fracture toughness values of toughened epoxies in the literature.

The determination of  $G_{Ic}$  using the technique described is a laborious process. Since many material compositions were studied in this work, to determine the  $G_{Ic}$  for each composition would have required a disproportionate amount of effort. Furthermore, in compositions with high rubber content, the U/BD vs.  $\dot{\delta}_{exp}$  relationship exhibits nonlinear behavior. This is probably because these materials cannot be described by linear elastic mechanics. To circumvent these two problems, a simplified procedure for determining fracture energy at a constant crack area was used. Sharp cracks approximately 3mm in length were introduced, and U/BD was measured and reported. This is, of course, just an instrumented Charpy test carried out at low rates, except that the crack is sharp, and that plane strain fractures are usually produced. The validity of this method was verified by comparison with the measured  $G_{Ic}$ . The advantage of this technique is that many fewer specimens are required, and the compliance function  $\dot{\delta}_{exp}$  need not be determined.

Testing of the SEN-3PB specimens was performed in a screw-driven Instron (Model 1125) operated at rates of  $4.23 \times 10^{-1}$  mm/sec or 2.12 mm/sec. The higher rate is necessary to avoid the ductile failure of some high-rubber content epoxies at the lower rate. The Instron chart recorder was operated at up to  $42 \text{ mm-sec}^{-1}$ , a rate sufficiently high to capture the data accurately. The pen in this chart recorder is capable of speeds up to  $250 \text{ mm-sec}^{-1}$ . Thus the load data are considered reliable. A minimum of seven SEN specimens was used to determine  $G_{Ic}$ . Only three specimens were used to determine U/BD at constant crack area.

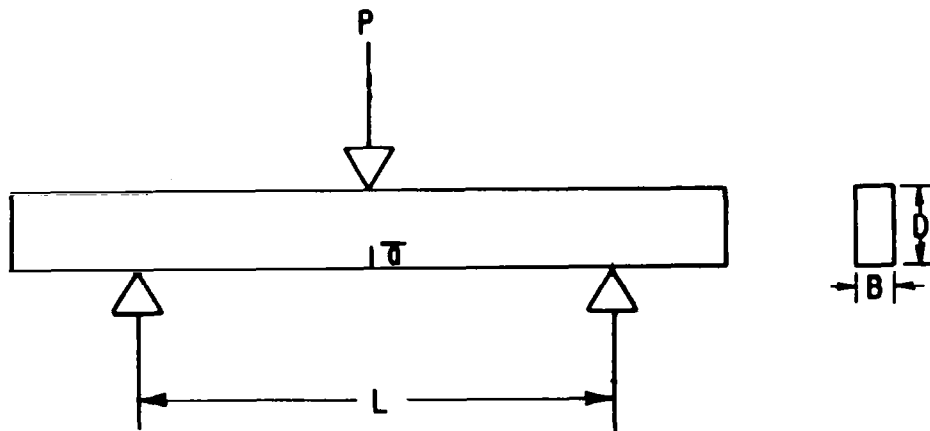
## 2.2 UNIAXIAL TENSILE DILATOMETRY

The technique of tensile dilatometry was modelled after that used by Bucknall and co-workers(20), except that constant displacement rate, rather than constant load, was used. Parts of the present technique have been described elsewhere(27). Dog-bone shaped specimens having gauge-section dimensions of 12.7mm W x 6.3mm T x 60mm L and overall length of ca. 150mm were cut from cast epoxy plaques with a high speed router and a steel template. Cut surfaces were polished with fine emery paper. No specimens were taken from near the edges of the cast plaques to avoid edge-related stresses arising from curing. Specimens with obvious voids and those found to have failed from macroscopic voids visible to the naked eye were rejected. From two to three specimens of each material were tested at each set of conditions. This small number of specimens was sufficient to indicate unambiguous trends in behavior due to the effects of material and testing variables. A servo-hydraulic testing machine (either an Instron or a MTS machine) was used at rates up to 254mm - sec<sup>-1</sup>. Two extensometers with the requisite sensitivity were used to measure the longitudinal and the width strains. The thickness strain was assumed to be identical to the width strain. The longitudinal extensometer was fastened to the specimen with rubber bands. Knife-edges on the extensometer formed the contacts. Some fractures, especially those obtained at low temperature, were induced by the sharp knife-edges, but this is judged to have little influence on the volume dilatation behavior, since only the maximum strain was affected. The transverse extensometer was likewise equipped with knife-edges, except that these knife-edges act as bearing surfaces against the sides of the specimen. Thus, the knife-edges also serve the important function of aligning the transverse extensometer. This clutched arrangement is

quite convenient to use and provides highly reproducible results. The load and the two displacements were simultaneously recorded into a four-channel digital oscilloscope (Norland 3001) with 0.025% of full scale resolution. This oscilloscope was also equipped with data processing capabilities, so that the stress and the two strains and the volume strain were all directly calculated. These results were either recorded onto an X-Y plotter or stored on magnetic discs for later use. The volume strain  $\frac{\Delta V}{V_0}$  was calculated using the following formula:

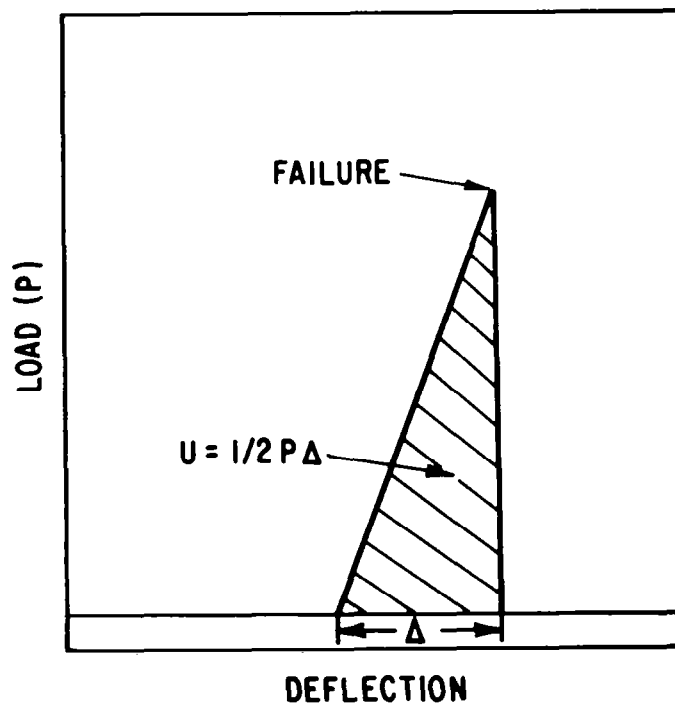
$$\frac{\Delta V}{V_0} = (1 + \varepsilon_1) (1 + \varepsilon_t)^2 - 1 \quad (2.8)$$

where  $\Delta V$  is the change in volume,  $V_0$  is the original volume, and  $\varepsilon_1$  and  $\varepsilon_t$  are the longitudinal and transverse engineering strains, respectively. The experiments were run at constant displacement rates, which meant that the strain rate was approximately constant only in the initial 1-2% region. This initial value is reported here as the strain rate,  $\dot{\varepsilon}$ . The initial slope of the stress-strain curves is reported here as the Young's modulus,  $E$ . The maximum in the engineering stress is reported here as the yield stress,  $\sigma_y$ . In those cases where the material formed a neck, such as those deformed at low rates and high temperatures,  $\frac{\Delta V}{V_0}$  is reported only up to the yield strain,  $\varepsilon_y$ , defined as the strain where  $\sigma_y$  was reached. Indeed, one shortcoming of the present technique is that volume changes in a localized zone, such as in a neck, cannot be assessed. Temperature variations in these experiments were provided by a chamber equipped with a Eurotherm temperature controller. Cooling was effected by injecting liquid nitrogen into the chamber.



**P = LOAD**  
**a = CRACK LENGTH**  
**L = SPAN**  
**D = DEPTH**  
**B = WIDTH**

2.1 SEN-3PB Test Specimen Configuration



2.2 A Typical Load-Deflection Curve of SEN-3PB Test

### 3. MATERIALS

#### 3.1 Material Preparation

The materials used in our investigation consisted of an epoxide resin, Epon 828, a liquid diglycidyl ether of bisphenol-A (DGEBA) produced by Shell Chemical Co., cured with piperidine, which was used as received (Aldrich Chemical Co.). The rubbers used were Hycar<sup>R</sup> CTBN 1300X8, Hycar CTBN 1300X13 and Hycar CTBN 1300X15 produced by B.F. Goodrich Chemical Co. These rubbers are liquid copolymers of butadiene and acrylonitrile with carboxyl end groups. Manufacturer's published properties for these liquid rubbers is shown in Table 3.1. Bisphenol-A (BPA), the resin modifier, was a reagent grade solid 4,4'-isopropylidenediphenol from the Aldrich Chemical Co.

The first set of materials investigated consisted of 100 parts Epon 828, five parts piperidine and, when rubber modified, either 5,10,15,20 or 30 parts Hycar CTBN. The preparation procedure for a 250mm x 250mm x 6mm plaque was as follows: Epon 828 (500 grams) and Hycar CTBN (25, 50, 75, 100 or 150 grams) were placed in a mixing jar. The mixture was placed in an oven at 70°C for approximately three hours. It was then taken out of the oven and mechanically stirred under a vacuum until it was thoroughly degassed. The vacuum was produced by a mechanical pump. Caution was taken to prevent extreme foaming by increasing the stirring rate and the vacuum slowly. The vacuum was then reduced and piperidine (29ml) was added via a syringe while stirring slowly. It was stirred rapidly again under a full vacuum until it is thoroughly degassed. The mixture was next poured into a Teflon<sup>R</sup>-coated mold that had been preheated to 120°C. It was cured for 16 hours at 120°C. The mold was then cooled at room temperature for approximately three hours to avoid warping

the plaque upon removal.

The second set of materials consisted of 100 parts Epon 828, 24 parts bisphenol-A, five parts piperidine, and when rubber modified, either 5,10,15, or 20 parts Hycar CTBN. The preparation procedure was as follows. The bisphenol-A (96 grams) was melt mixed into Epon 828 (400 grams) by placing them into a glass mixing jar and heating the mixture to ca. 160°C with a heating mantle while stirring with a mechanical stirrer. The mixture was cooled to room temperature. When rubber modified, the rubber (20,40,60 or 80 grams) was added to the Epon 828/BPA mixture and heated in an oven for 1 hr. at 50°C. The remainder of the procedure was similar to that for the 828 system.

To designate the various rubber-modified materials, the notation shown in Table 3.2 is adopted:

**TABLE 3.1**  
**Table of Properties of Several Hycar<sup>R</sup> CTBN Elastomers**  
**Published by B.F. Goodrich Chemical Company**

	Hycar <sup>R</sup> 1300X15 CTBN	Hycar <sup>R</sup> 1300X8 CTBN	Hycar <sup>R</sup> 1300X13 CTBN
Viscosity, Brookfield, mPa.s or cP at 27°C (81°F)	55,000	125,000	625,000
Percent carboxyl	2.47	2.37	2.40
Molecular weight	3,500	3,500	3,500
Functionality	1.9	1.85	1.85
Acrylonitrile content, %	10	17	27
Solubility parameter	8.45	8.77	9.14
Heat loss, 2 hours at 130°C (266°F), %	<2.0	<2.0	<2.0
Specific gravity at 25°C/25°C (77°F)	0.924	0.948	0.960

**TABLE 3.2\***  
**Table of the Rubber-Modified Epoxies Investigated in this Study**  
**and Their Corresponding Designations.**

Resin	Amount BPA(phr)**	Type Of Rubber	Amount Of Rubber(phr)**	Designation	T <sub>g</sub> °C***
Epon 828		-	-	828	84.2
Epon 828		Hycar CTBN 1300X8	5	828-8(5)	-
Epon 828		Hycar CTBN 1300X8	10	828-8(10)	85.6
Epon 828		Hycar CTBN 1300X8	15	828-8(15)	-
Epon 828		Hycar CTBN 1300X8	20	828-8(20)	87.5
Epon 828		Hycar CTBN 1300X8	30	828-8(30)	82.4
Epon 828		Hycar CTBN 1300X15	5	828-15(5)	-
Epon 828		Hycar CTBN 1300X15	10	828-15(10)	84.2
Epon 828		Hycar CTBN 1300X15	15	828-15(15)	-
Epon 828		Hycar CTBN 1300X15	20	828-15(20)	89.4
Epon 828		Hycar CTBN 1300X15	30	828-15(30)	86.1
Epon 828		Hycar CTBN 1300X13	5	828-13(5)	-
Epon 828	24	-	-	828-BPA(24)	104.4
Epon 828	24	Hycar CTBN 1300X8	5	828-BPA(24)-8(5)	100.6
Epon 828	24	Hycar CTBN 1300X8	10	828-BPA(24)-8(10)	-
Epon 828	24	Hycar CTBN 1300X8	15	828-BPA(24)-8(15)	97.6
Epon 828	24	Hycar CTBN 1300X8	20	828-BPA(24)-8(20)	90.5

\* 5phr piperidine was used for all material

\*\* phr=parts per hundred parts resin by weight

\*\*\* T<sub>g</sub> was determined by DSC at 20°C/min from second heating

### 3.2 Morphology

Transmission Electron Microscopy (TEM) of osmium tetroxide ( $\text{OsO}_4$ ) stained rubber-modified materials was performed to investigate the differences in morphology. A quantitative analysis, using the method of Schwartz-Saltykov,(39) on TEM micrographs containing a total of at least 86 rubber particles per system was performed to determine rubber particle size distribution and the percent rubber volume.

#### 3.2.1 828-15 Systems

Figures 3.1 to 3.4 are typical TEM micrographs of  $\text{OsO}_4$  stained 828-15 materials with 5,10,20 and 30 phr rubber, respectively. The rubber particles are approximately spherical, and do not show any internal structure. The diameters of the particles range from submicron to  $>8\text{ }\mu\text{m}$  (see Figure 3.5). It is interesting to note that the mean diameter of the rubber particles increases with rubber content until 30 phr, where it begins to decrease. At the same time the particle size distribution becomes more uniform with increasing rubber content.

#### 3.2.2 828-8 System

Figures 3.6 to 3.10 are typical TEM micrographs of  $\text{OsO}_4$  stained 828-8 materials with 5,10,20 and 30 phr rubber, respectively. The rubber particles are spherical in shape. Diameters of these rubber particles are in a narrow range of  $.75\text{--}1.5\text{ }\mu\text{m}$ . Again, the mean diameter increases with rubber content. At 30 phr rubber a phase inversion has taken place. The rubber phase now forms the continuous matrix and the epoxy phase is dispersed (up to  $10\text{ }\mu\text{m}$  in diameter) with rubber inclusions  $.1\text{--}.5\text{ }\mu\text{m}$  in diameter.

### 3.2.3 828-BPA(24)-8 System

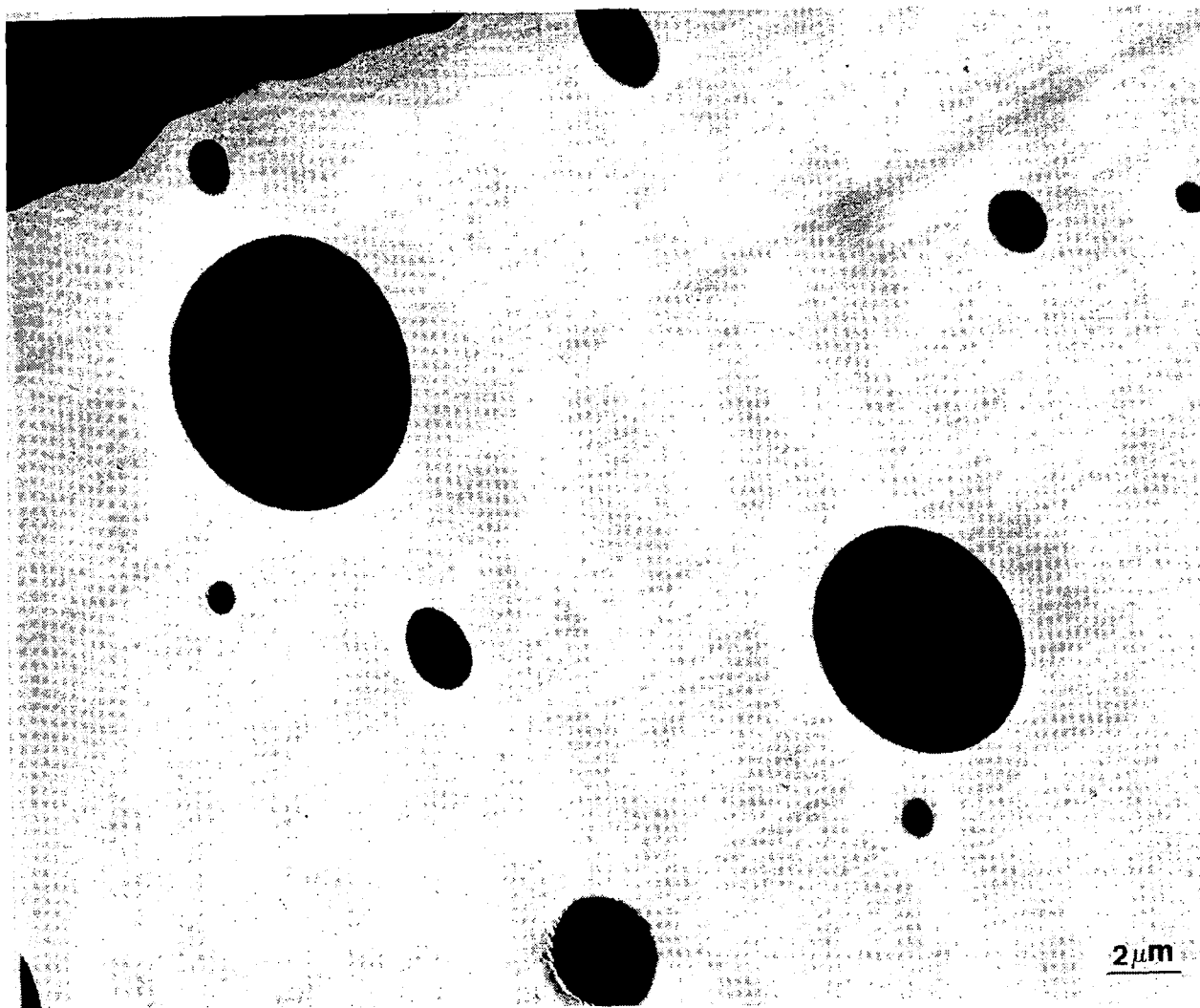
Figure 3.11 is a typical TEM micrograph of  $\text{OsO}_4$  stained 828-BPA(24)-8(15) material. There exist large, two-phase rubber particles ( $>1\ \mu\text{m}$ ) surrounded by small homogeneous rubber particles ( $<1\ \mu\text{m}$ ). Note that the materials in this BPA-modified system with lower rubber content contain only rubber particles without sub-inclusions.

Unlike Sayre et.al.(40), who found significant amounts of rubber unaccounted for in low magnification TEM micrographs, the rubber volume fraction found in this work corresponds well to calculated amounts. Figure 3.12 is a plot of the initial volume percent rubber added to the epoxy resin versus the volume percent of rubber precipitated out. The initial volume percent rubber is calculated using a density of 1.2 g/ml for Epon 828 and the manufacturer's published densities (see Table 3.1) for the rubbers. The  $45^\circ$  line is for the case of 100% precipitation. The CTBN-8 system nearly completely precipitates out, whereas the CTBN-15 system shows an excess volume. This indicates that some of the epoxy may have been included in the rubber phase.

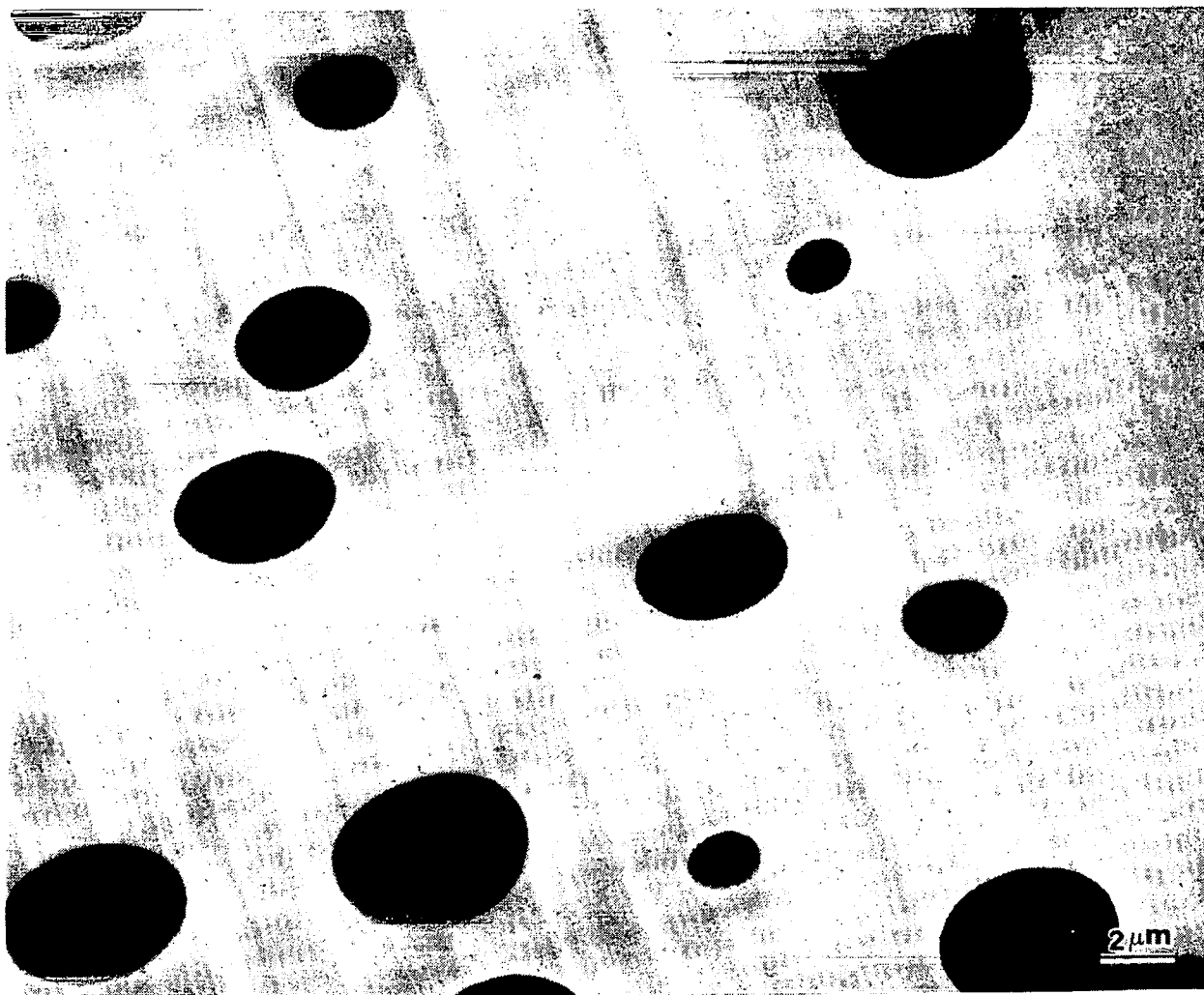
## 4. FRACTURE TOUGHNESS

In order to study the deformation mechanisms of rubber-modified epoxies, one must ascertain to what extent these materials are toughened. The SEN-3PB method was used to determine the strain energy release rate  $G_{IC}$ . It has been described in detail in Section 2.1.

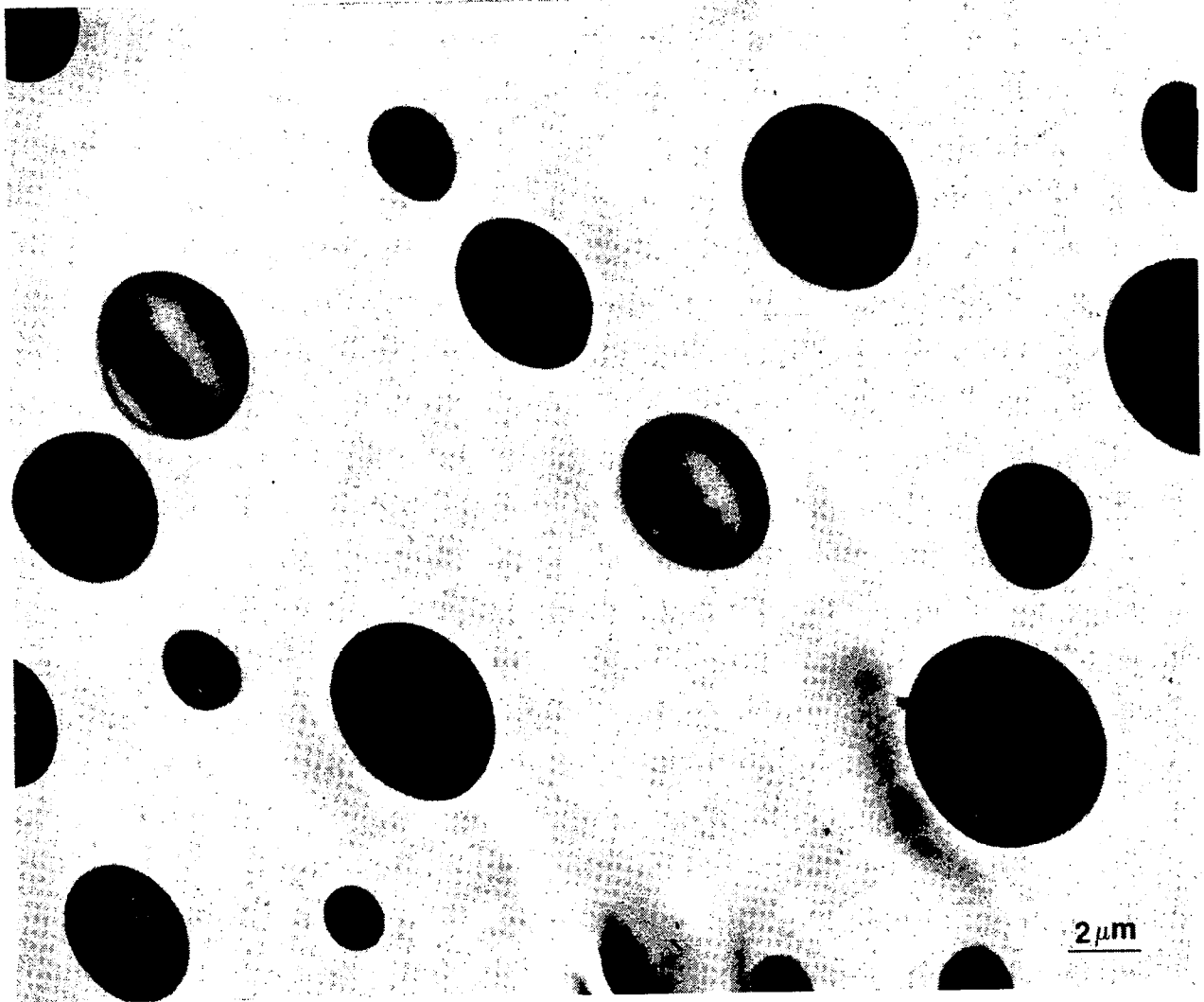
Several SEN-3PB specimens (11mm x 6mm x 100mm) were prepared for each material. Each specimen was notched using a jeweler's saw. Sharp cracks were



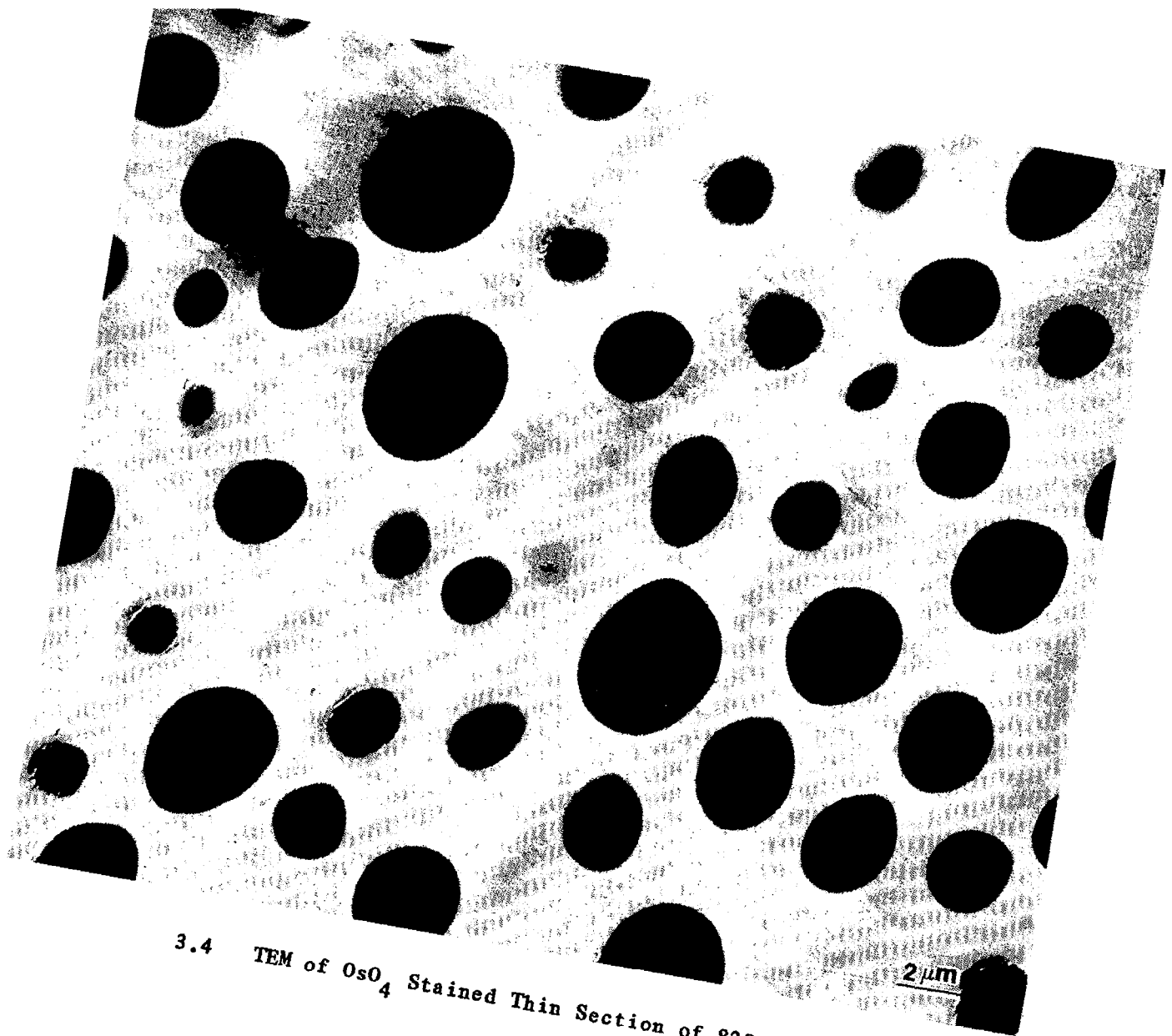
3.1 TEM of  $\text{OsO}_4$  Stained Thin Section of 828-15(5)



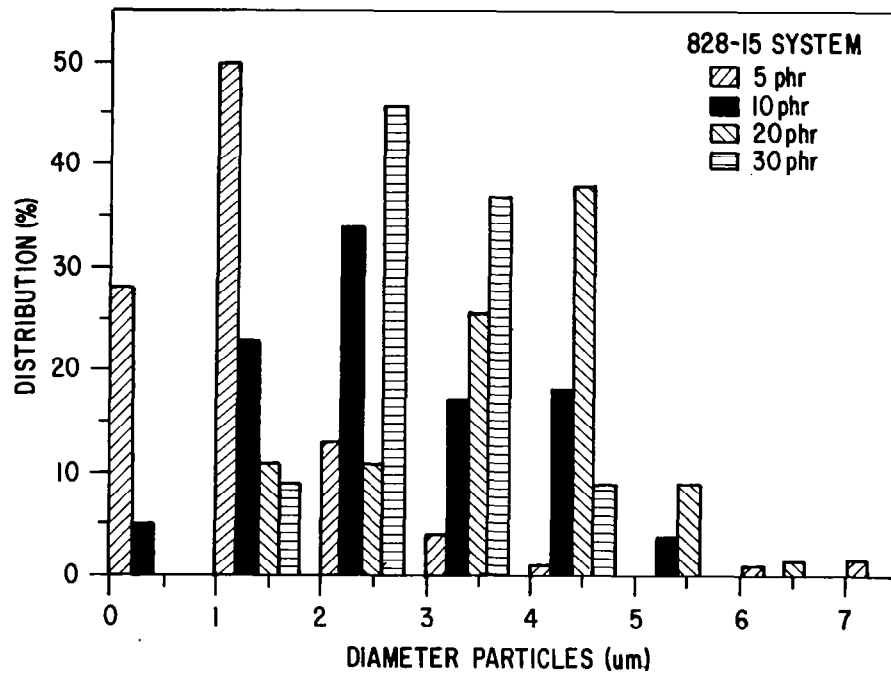
3.2 TEM of  $\text{OsO}_4$  Stained Thin Section of 828-15(10)



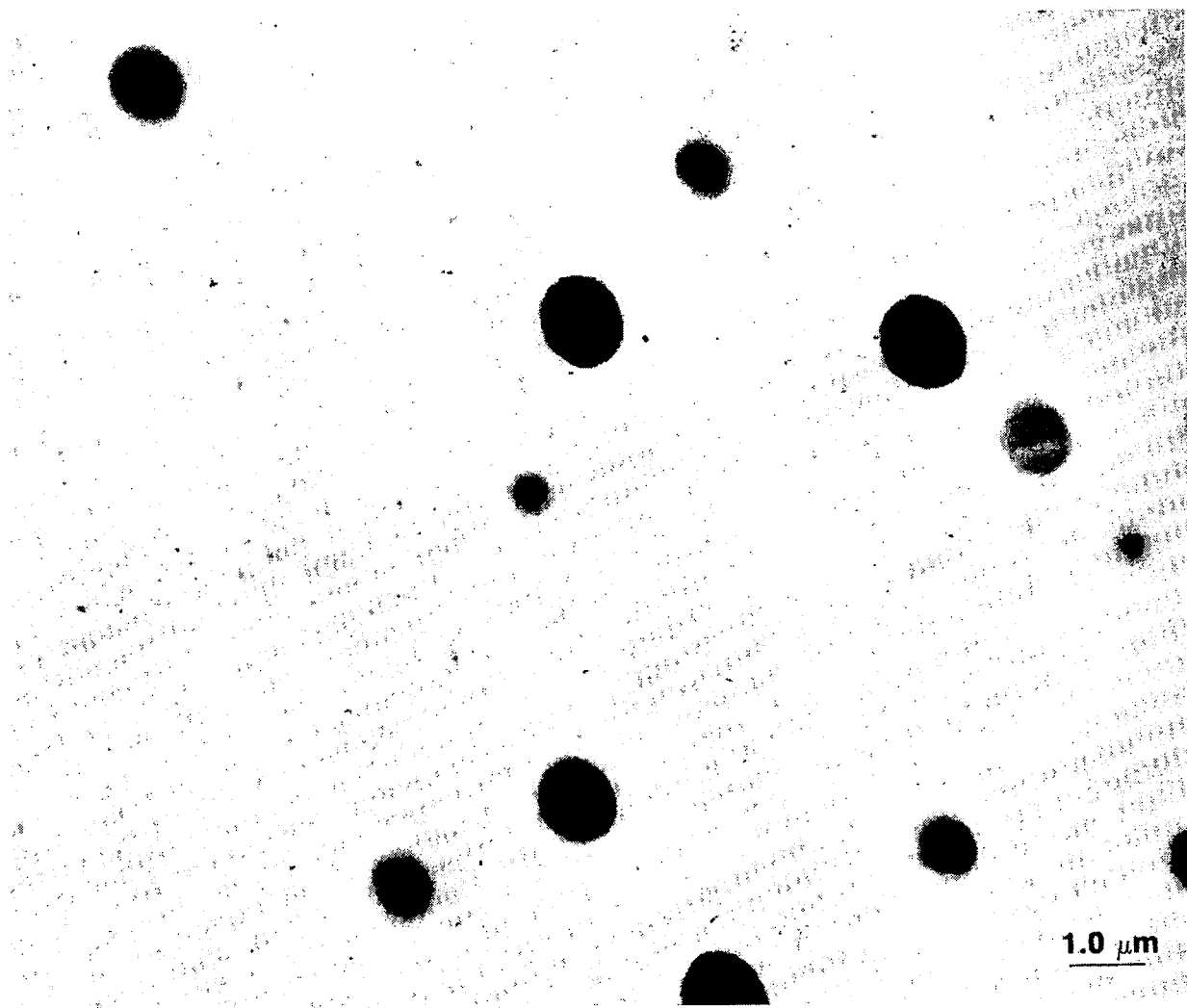
3.3 TEM of  $\text{OsO}_4$  Stained Thin Section of 828-15(20)



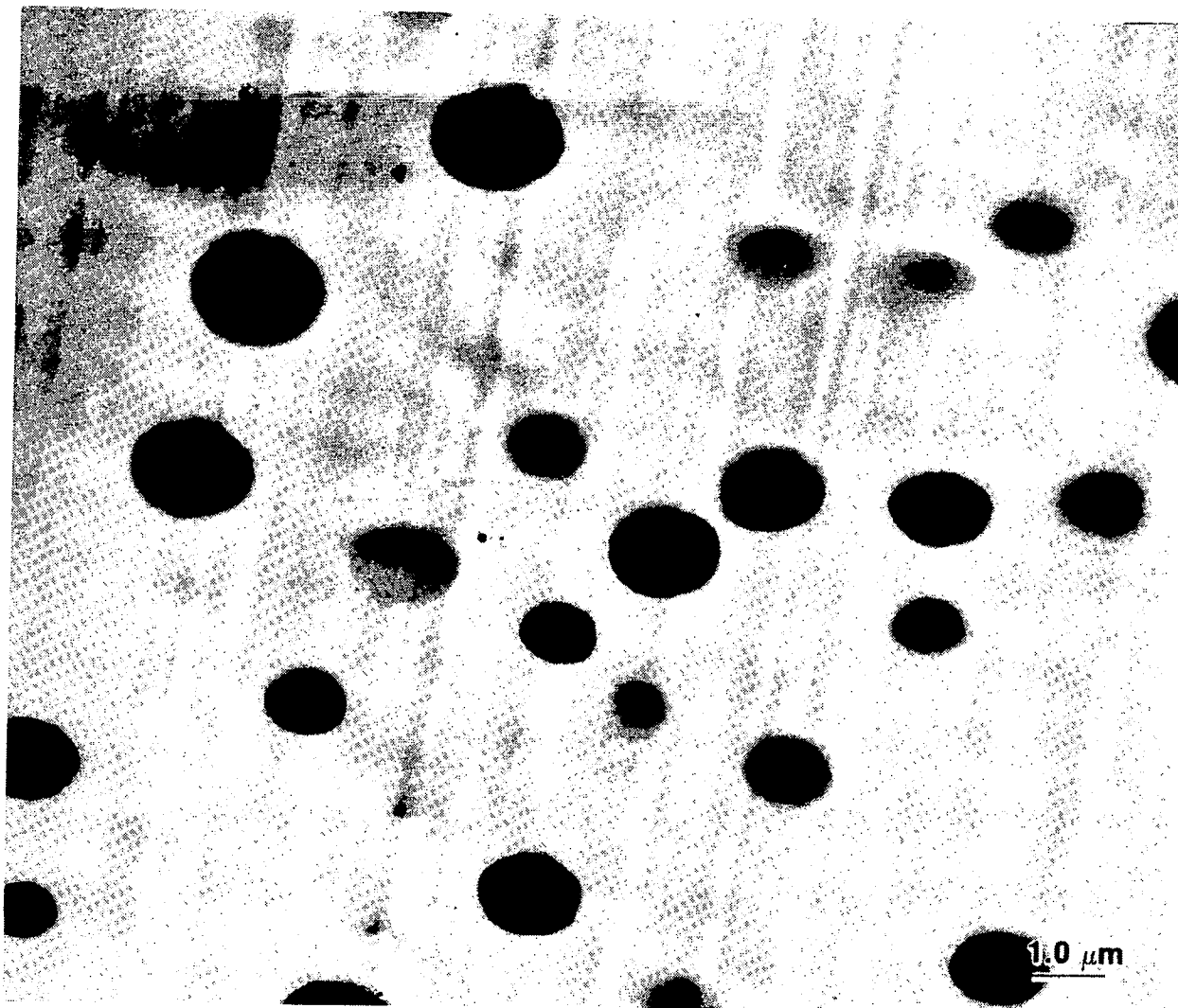
3.4 TEM of  $\text{OsO}_4$  Stained Thin Section of 828-15(30)



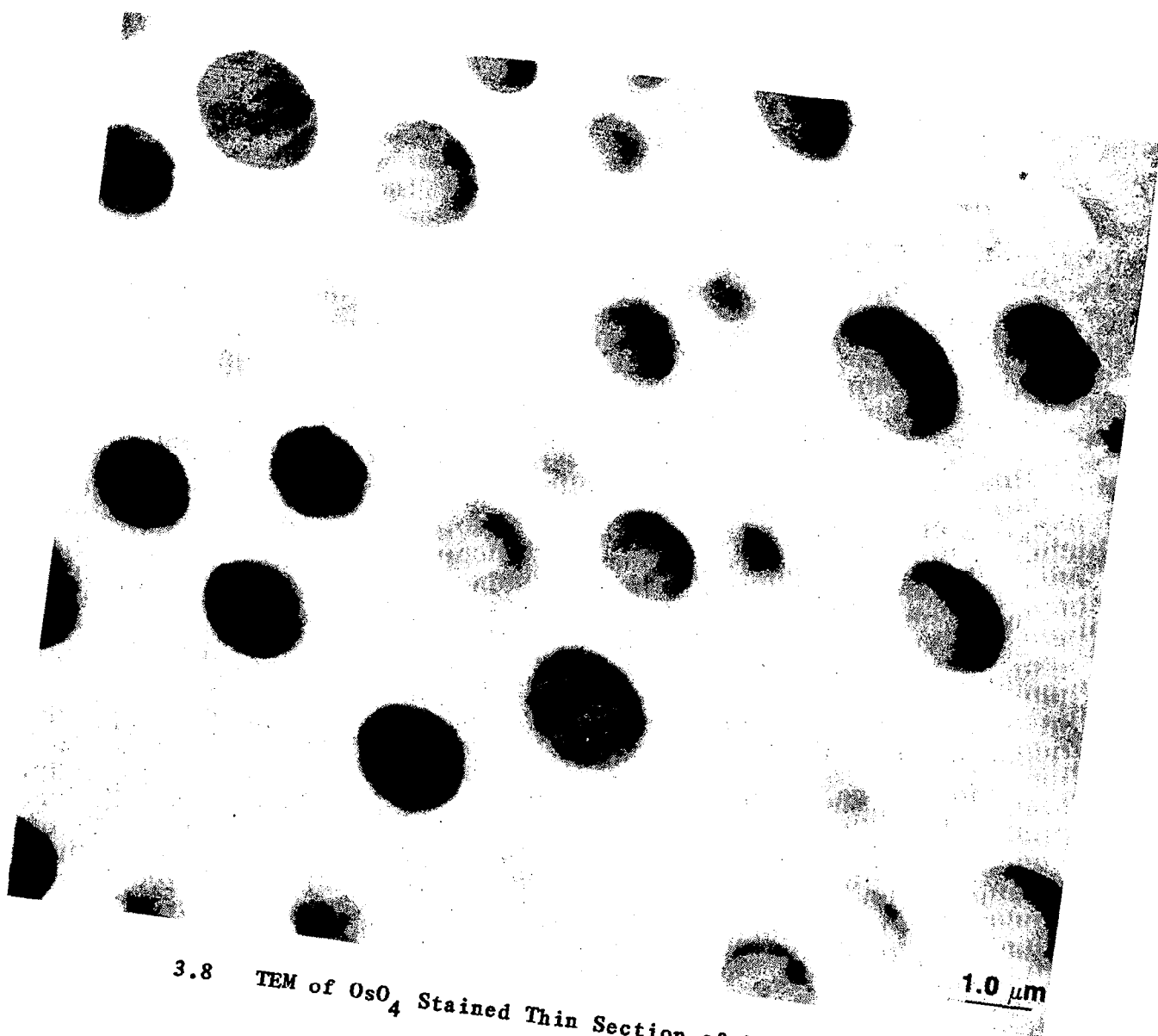
**3.5 Distribution of Rubber Particle Diameters for 828-15 Material**



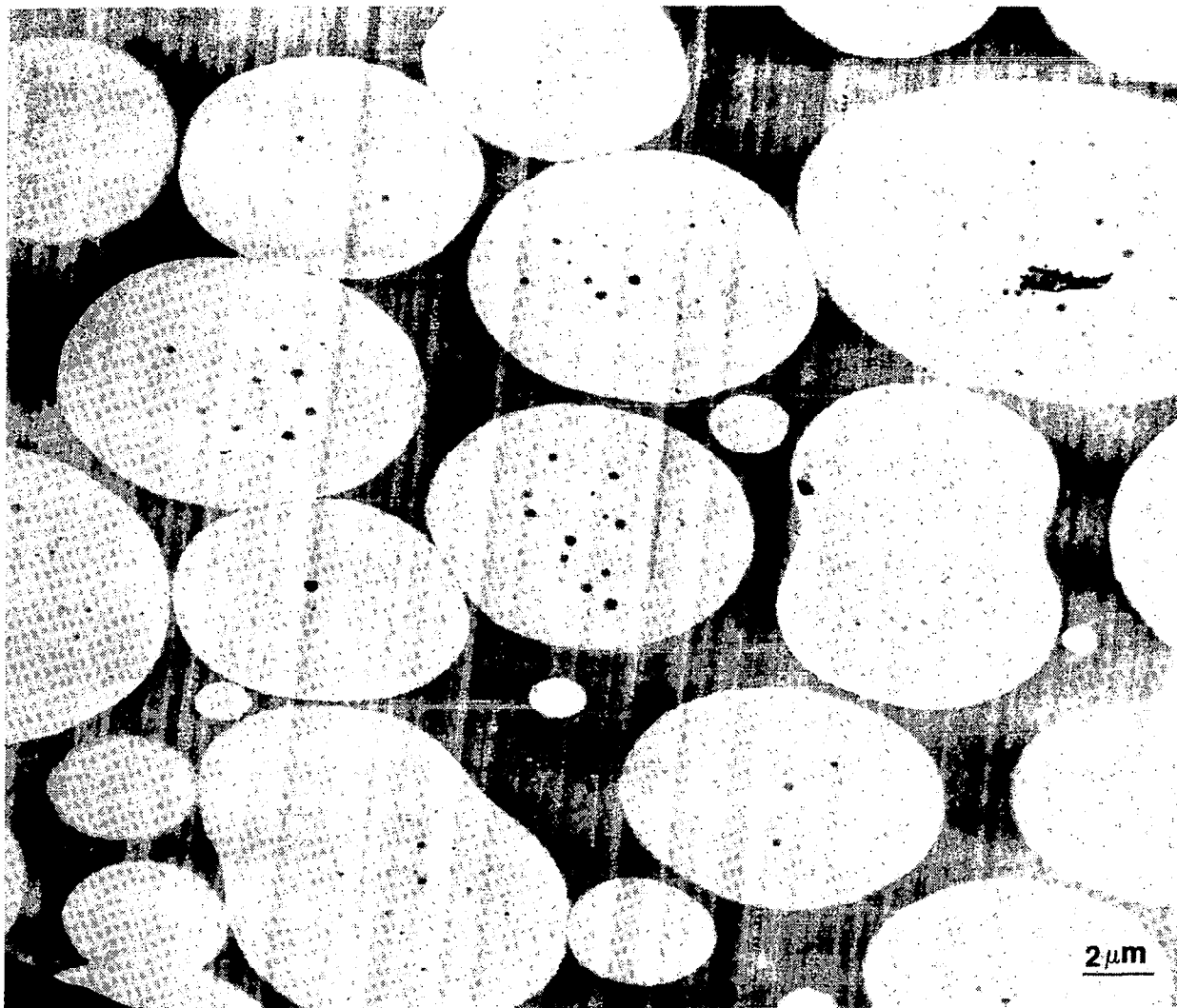
3.6 TEM of  $\text{OsO}_4$  Stained Thin Section of 828-8(5)



3.7 TEM of  $\text{OsO}_4$  Stained Thin Section of 828-8(10)



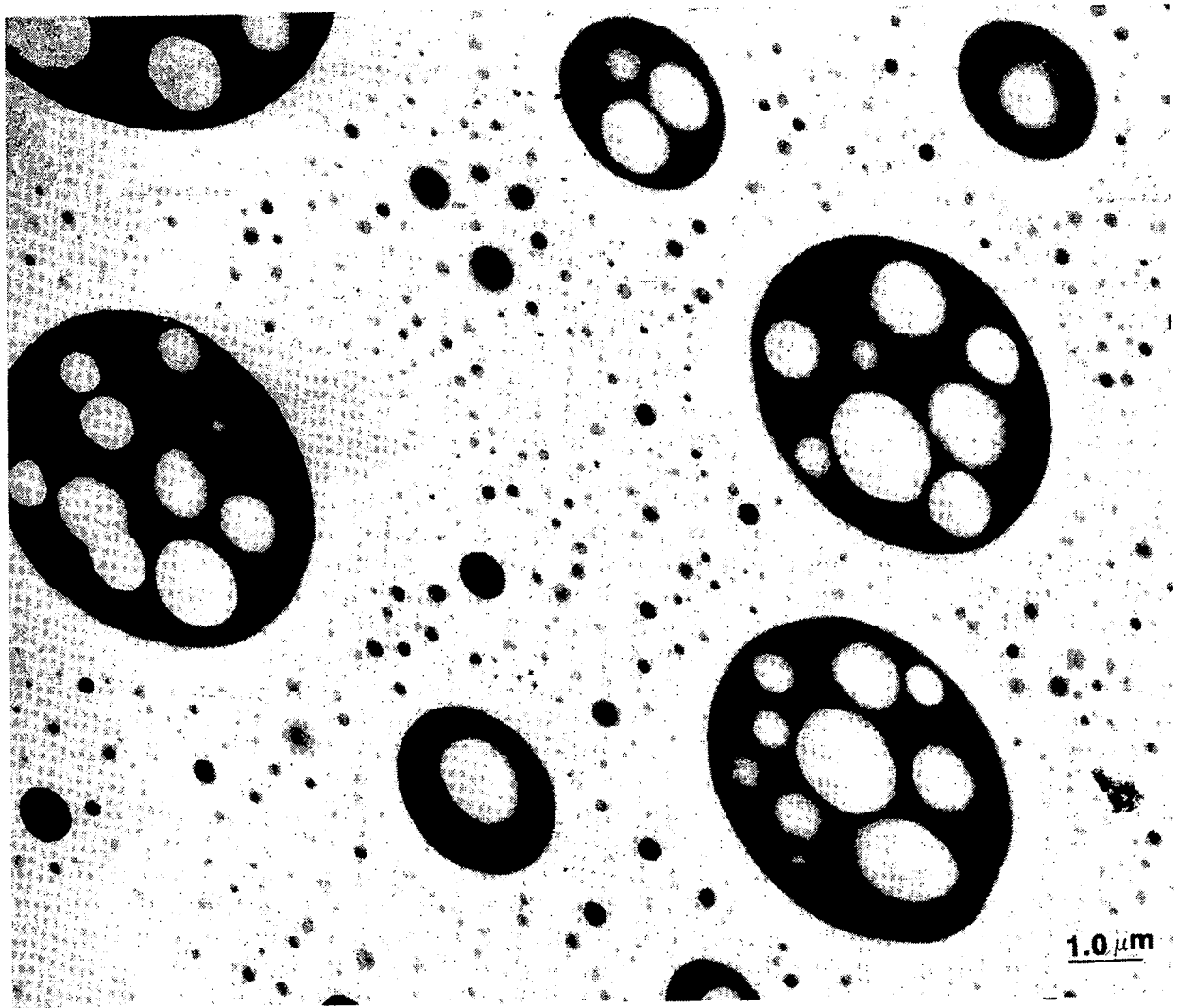
3.8 TEM of  $\text{OsO}_4$  Stained Thin Section of 828-8(20)



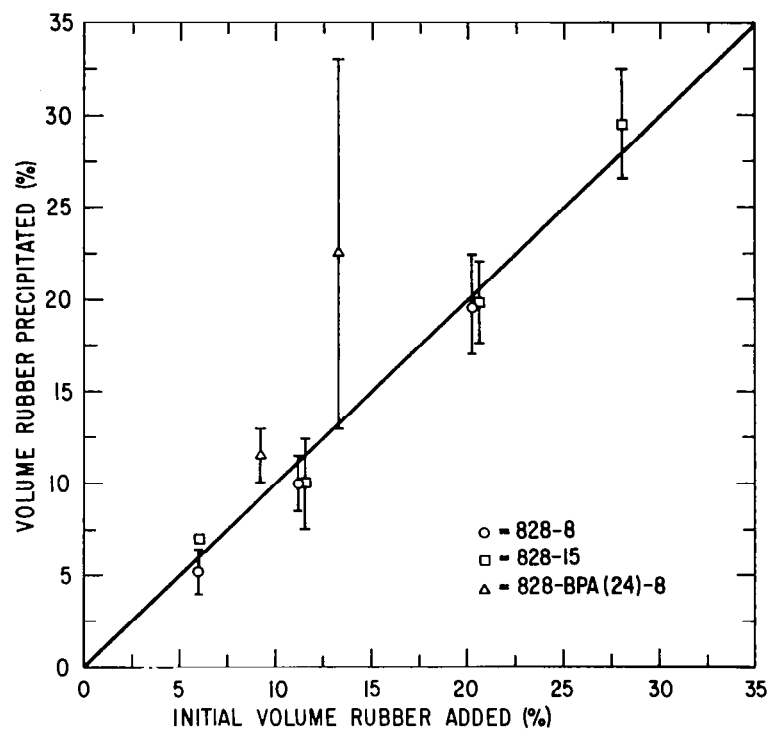
3.9 TEM of  $\text{OsO}_4$  Stained Thin Section of 828-8(30)



3.10 TEM of  $\text{OsO}_4$  Stained Thin Section of 828-8(30)



3.11 TEM of  $\text{OsO}_4$  Stained Thin Section of 828-BPA(24)-8(15)



**3.12 Plot of Precipitated Volume Percent Rubber vs. Initial Volume Percent Rubber**

initiated by several taps with a hammer on a fresh razor blade which had been immersed in liquid nitrogen. However, with high rubber content materials, a small stress-whitened zone was always observed ahead of the crack tip. The specimens were tested in a screw driven Instron testing machine. Crack lengths were measured on the fracture surfaces by using either a microscope or magnified photographs. The span was kept constant at 66mm.

#### 4.1 Compliance Function $\Phi$

The significance of the compliance function  $\Phi$  has already been discussed in Section 2.1. In these experiments, it was found that the experimentally determined compliance function  $\Phi_{\text{exp}}$  was considerably different from the theoretical  $\Phi$ , especially at short crack lengths. The compliance,  $C$ , was determined in the following manner: In the case of the low rubber-content materials, the load-deflection curves were linear.  $C$  was then simply calculated by dividing the maximum load  $P_{\text{max}}$  by the total deflection  $\Delta$ . In the case of the high rubber-content materials, the load-deflection curves were non-linear at the deflection rate used.  $C$  was then calculated from the initial slope. In these cases, the measured  $C$  was most likely too high since a stress-whitened zone existed ahead of the crack tip. The measured  $C$  was then plotted against  $X=a/D$ . A polynomial was fitted to the  $C$  vs.  $X$  curve by computer. The slope  $dC/dX$  was determined by differentiating the polynomial. Typical results for a low and a high-rubber content material are shown in Figures 4.1 and 4.2, respectively. It is interesting to note that  $\Phi_{\text{exp}}$  for the high-rubber content material agrees with the theoretical  $\Phi$  over a wider range of crack lengths than for the low-rubber content material. Plati and Williams(35) found good agreement between  $\Phi_{\text{exp}}$  and  $\Phi$  using machined blunt-notch

specimens. Since in the high-rubber content materials tested here a stress-whitened zone existed ahead of the crack tip, the crack has effectively been blunted. This may be the reason why the agreement is better.

#### 4.2 $G_{Ic}$ Determination

As described in Section 2.1,  $G_{Ic}$  can be determined by plotting  $U/BD$  against  $\Phi$ , which should result in a linear curve whose slope is  $G_{Ic}$ . It was found in these experiments that if  $U/BD$  was plotted against the theoretical  $\Phi$ , and a straight line was fitted to the data, the line had a negative intercept on the abscissa. This result is physically impossible, because it would mean that a specimen with zero compliance would release energy to the testing machine. When the experimentally determined  $\Phi_{exp}$  was used instead, a positive intercept was always obtained if a straight line could be fitted to the data. The positive intercept is due to residual kinetic energy. Since the specimen geometry employed always produced unstable fracture, except at high-rubber contents, the specimens often jumped off their supports upon fracture from this residual kinetic energy.

##### 4.2.1 Neat Resin and Low Rubber-Content Materials

The  $U/BD$  vs.  $\Phi_{exp}$  results for the neat Epon 828 resin and four modified materials, each with 5 phr rubber, are shown in Figure 4.3. It can be seen that data scatter is relatively large, especially for the 828-13(5) system. Since the primary purpose of this work is to determine toughening mechanisms, and not to produce precise measurements of  $G_{Ic}$ , it is felt that obtaining

relative changes in toughness is sufficient, as long as the toughness is not different from literature values by a large amount. The low  $G_{Ic}$  values for the 828-13(5) system result from the failure of the rubber to precipitate as a dispersed phase.

The present results are compared against some results from the literature. These results are listed in Table 4.1. It is readily apparent that fracture energy values differ widely. This is perhaps not surprising, considering the large number of uncontrollable variables that can result from the variety of material preparation, specimen fabrication and testing techniques employed. Since it is not the purpose of this work to investigate the causes for the variations in literature values, it is felt that to have found a ten-fold increase in  $G_{Ic}$  in the 5phr rubber-modified epoxies is sufficient to satisfy the condition that the epoxies used in this work have indeed been properly toughened. The fact that the absolute values of  $G_{Ic}$  found in this work fall into the low range of literature values may be because the cracks were initiated at a lower temperature. It is quite possible that the cracks thus initiated are simply sharper.

TABLE 4.1  
Table of Fracture Toughness Measurements of Hycar<sup>R</sup> CTBN  
1300X8-Modified Epoxy for Several Test Geometries  
Fracture

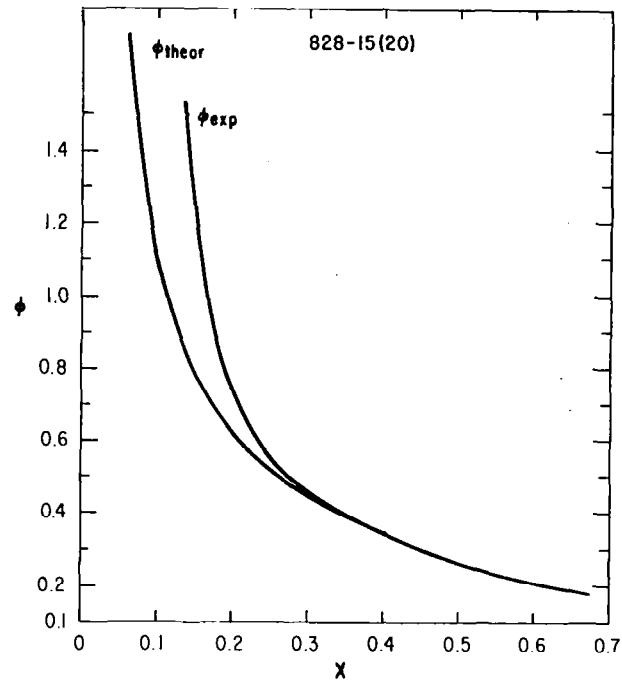
CTBN*	Concentration (wt%)	Energy $G_{Ic}$ (J/m <sup>2</sup> )	Test	Reference
	0	121	Tapered double Cantilever beam	W.D. Bascom, R.L. Cottingham R.L. Jones and P. Peyses, J. App. Polym. Sci., 19, 2524 (1975).
	4.5	1050		
	10.0	2720		
	15.0	3430		
	20.0	3590		
	0	154	Tapered double Cantilever beam	R.Y. Ting and R.L. Cottingham J. Appl. Polym. Sci., 25, 1815 (1980).
	4.5	1600		
	0	290	Notched impact	
	8.0	1100		
	0	180	Double cantilever beam	B.F. Goodrich Co., Hycar <sup>R</sup> product guide
	4.5	2630		
	4.5(BPA)	8600		
	0	79	SEN-3PB	This work
	4.5	790		
	4.5**	770		
	4.5(BPA)	906		

\*Hycar<sup>R</sup> CTBN 1300X8 except as noted

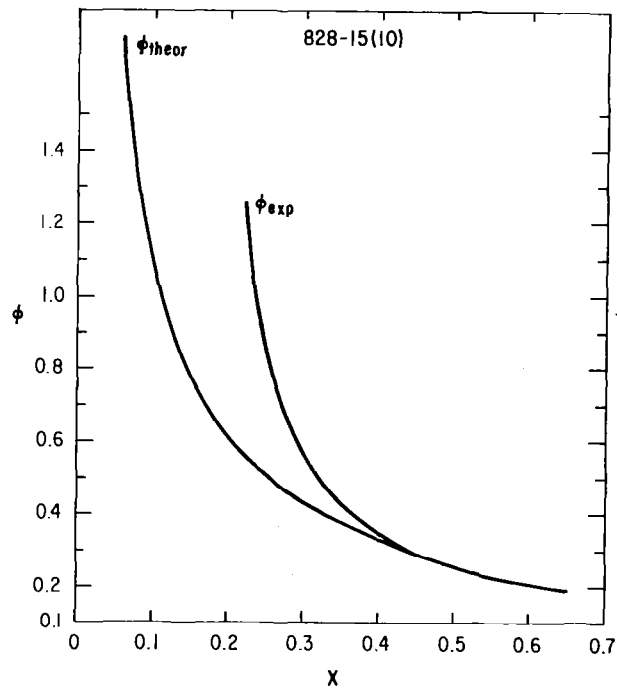
\*\*Hycar<sup>R</sup> CTBN 1300X15

#### 4.2.2 High Rubber Content Materials

The deflection rate was increased to 2.12mm/sec (5in/min) in order to obtain unstable fracture for the high rubber-content materials. For these materials, a linear  $P$  vs.  $\Delta$  curve was not always obtainable, especially at long crack lengths. Consequently, the  $U/BD$  vs.  $\bar{\Phi}_{exp}$  plot did not always exhibit a linear relationship. It is clear that linear elastic fracture mechanics cannot be applied to these materials under the given set of testing conditions. To circumvent this problem, it was decided not to attempt to measure  $G_{Ic}$  but instead to compare the energy absorbed per unit area at a constant crack length of 3mm. If the theoretical  $\bar{\Phi}$  is valid for all these materials, this would be equivalent to measuring the energy at a constant  $\bar{\Phi}$ . These results are shown in Figure 4.4. Note from Figure 4.3 that the  $G_{Ic}$  for 828-15(5),  $737 \text{ J/m}^2$ , is only 23% lower than the  $G_{Ic}$  for 828-BPA(24)-8(5), which is  $906 \text{ J/m}^2$ . However, in Figure 4.4, the energy per unit area for the latter system is nearly three times higher than that for the former system. This is due to the difference in  $\bar{\Phi}_{exp}$ . Consequently, the relative change in energy for the different rubber systems cannot be literally interpreted. Within one given rubber system, however, the relative change in energy with rubber content probably indicates the approximately correct trend in the true  $G_{Ic}$ . The change in energy at constant crack length with rubber volume for the 828-15 system is shown in Figure 4.5. Similar to the other two systems, the energy levels off at around 15 phr rubber. Since the modulus of this material decreases linearly with rubber content (see Section 5.2), large deformation non-linear behavior is probably responsible for the leveling off. Non-linear

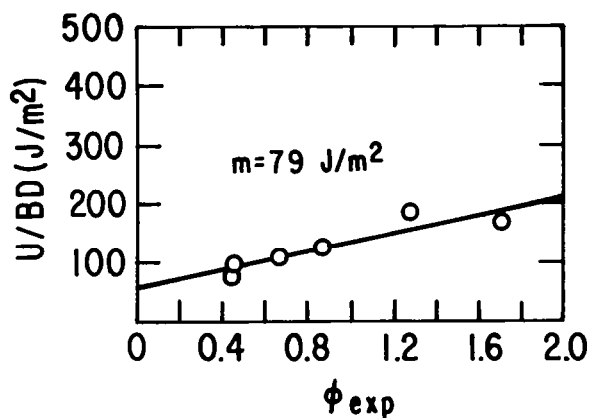


4.1 Comparison of Theoretical Compliance Function  $\phi$  and The Experimental Results  $\phi_{\text{exp}}$  for 828-15(20)

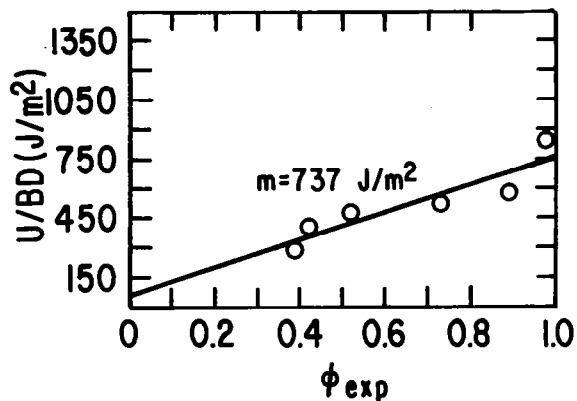


4.2 Comparison of Theoretical Compliance Function  $\phi$  and The Experimental Results  $\phi_{\text{exp}}$  for 828-15(10)

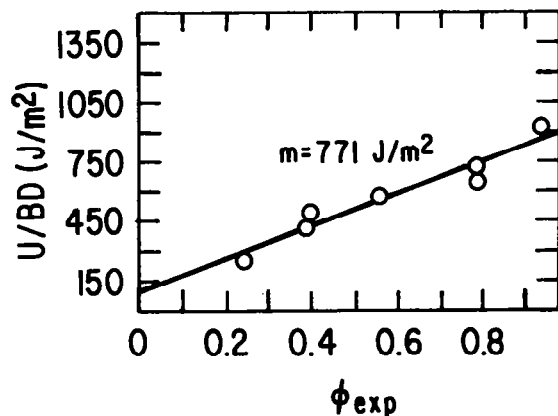
A. EPON 828/PIPERIDINE



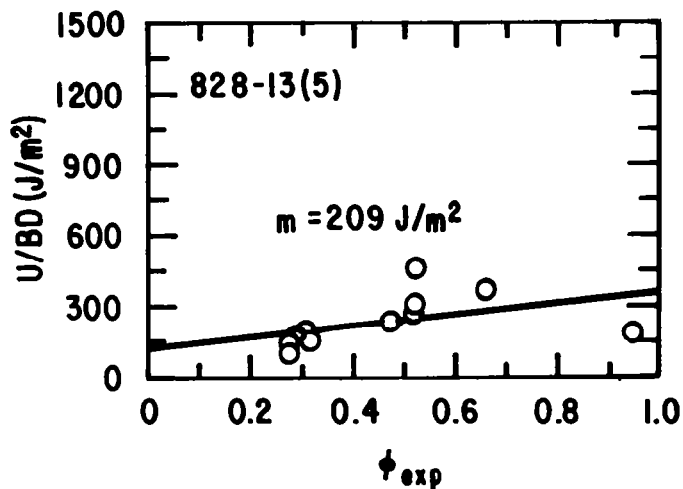
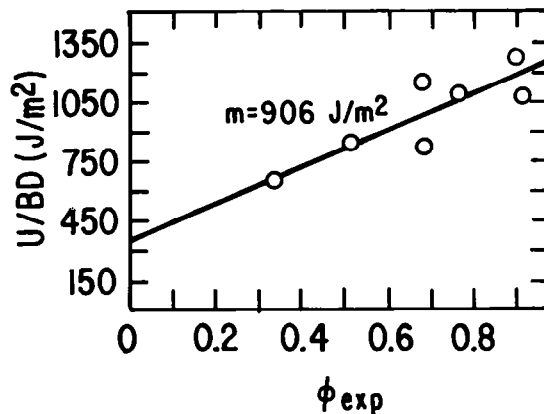
B. EPON 828/HYCAR 1300 X 15/PIPERIDINE



C. EPON 828/HYCAR 1300 X 8/PIPERIDINE

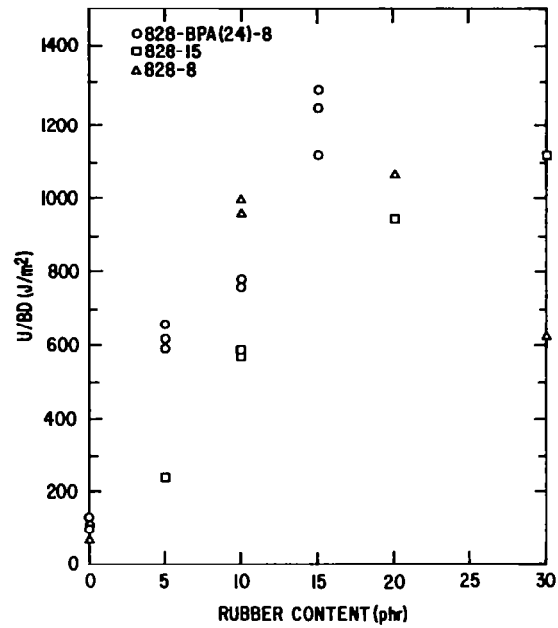


D. EPON 828/HYCAR 1300 X 8/BPA/PIPERIDINE

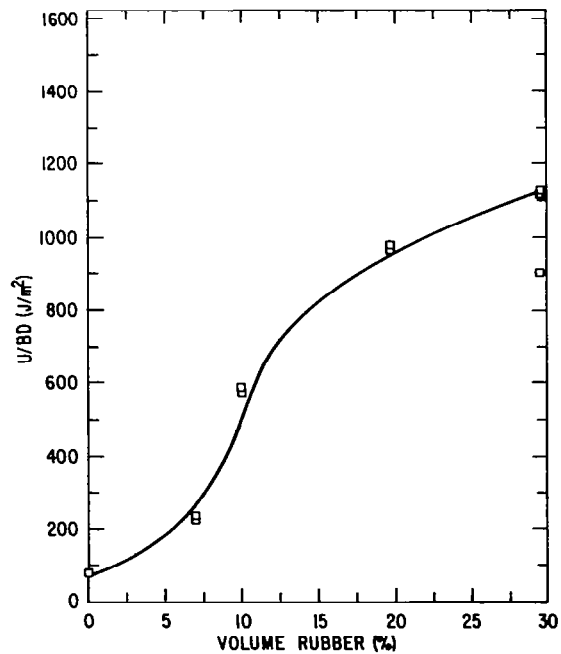


#### 4.3 $G_{Ic}$ Results For The Epon 828 Material and Four Rubber Modified

Materials with 5phr Rubber (Rate 1"/min)



#### 4.4 U/BD vs. Rubber Content (At a Cross Head Rate of 5"/min) For Three Rubber Systems



#### 4.5 U/BD vs. Volume Rubber for 828-15 Materials (Rate - 5in/min)

dependence on rubber content is also noted in the tensile yield behavior. The possible cause for these effects are discussed in Section 5.2.3 and when the micrographic studies are presented.

## 5. TENSILE DILATOMETRY

### 5.1 VOLUME DILATION EXPERIMENTS

#### 5.1.1 Neat Resins

##### 5.1.1A. 828 System

Figure 5.1 is a plot of volume strain ( $\Delta V/V_0$ ) versus elongational strain ( $\epsilon_1$ ) at  $27 \pm 3^\circ\text{C}$  for several strain rates. The initial, approximately linear, portion of these curves is due to homogeneous deformation with a constant lateral contraction ratio, i.e., a constant rate of dilation ( $\Delta \dot{V}/V_0 = \frac{d\Delta V/V}{d\epsilon_1} =$  constant). Before the yield stress is reached,  $\Delta V/V_0$  exhibits a maximum, followed by a subsequent decrease. This decrease signifies the onset of the shear flow process. The possible mechanisms for the decrease in  $\Delta \dot{V}/V_0$  is discussed in Section 5.1.4. Subsequent visual examination showed that shear bands had formed prior to rupture. The effect of increasing strain rates is one of delaying and increasing the  $\Delta V/V_0$  maximum in a manner similar to its effect on the yield stress. Thus, at sufficiently high strain rates the shear flow process could be delayed so much that brittle failure might occur.

Figure 5.2 is a plot of  $\Delta V/V_0$  versus  $\epsilon_1$  at  $65 \pm 2^\circ\text{C}$  for several strain rates. The curves again show an initial constant rate of dilatation and then

shear flow. At the lowest strain rate there is evidence that the shear flow process begins at the low strain of 1%.

#### 5.1.1B. 828-BPA(24) System:

Figure 5.3 is a plot of  $\Delta V/V_0$  vs.  $\epsilon_1$  at  $27 \pm 3^\circ\text{C}$  for several strain rates. Again the curves show an initial constant rate of dilatation and then shear flow. Shear banding is also visually evident in this material. The strain rate dependence of the  $\Delta V/V_0$  maximum is even more pronounced in this system than in the 828 system. Thus, the possibility of delaying the shear flow process by increasing the strain rate appears even greater for the 828-BPA(24) system.

#### 5.1.2 Rubber Modified Systems

##### 5.1.2A. 828-15 System

Figure 5.4 is a plot of  $\Delta V/V_0$  versus  $\epsilon_1$  at  $27 \pm 3^\circ\text{C}$  with varying rubber content. The curves show an initial constant  $\dot{\Delta V}/V_0$  portion followed by an increasing  $\dot{\Delta V}/V_0$  portion that is indicative of a voiding process. These are then followed by decreasing  $\dot{\Delta V}/V_0$ , signifying the onset of the shear flow process. Increasing rubber content delays the onset of the voiding process. The effect of strain rate on  $\Delta V/V_0$  of the 828-15(20) material is shown in Figure 5.5. Again, high strain rates delay the shear flow process and accentuate voiding.

Figure 5.6 is a plot of  $\Delta V/V_0$  versus  $\epsilon_1$  at  $-16 \pm 2^\circ\text{C}$  with varying rubber

content. The curves show an initial constant  $\Delta\dot{V}/V_0$  portion, an accelerated voiding portion and another constant  $\Delta\dot{V}/V_0$  portion. The onset of rapid void growth occurs at lower  $\epsilon_1$  than at room temperature. Increasing rubber content retards this rapid voiding process but increases the total volume strain at yield. Figure 5.7 is a plot of  $\Delta V/V_0$  versus  $\epsilon_1$  of the 828-15(20) material at  $-16\pm 2^\circ\text{C}$  for several strain rates. At increasing strain rates, the onset of rapid void growth occurs at increasing  $\epsilon_1$ . The effect of increasing strain rates, however, is not as significant as that of increasing rubber content. Note that in contrast to higher temperature behavior, the voiding portion is not succeeded by decreasing  $\Delta\dot{V}/V_0$ . Instead, the second volume strain rate is even higher than the initial rate by an amount predicted by assuming that the "Poisson's ratio" of the material is reduced by a factor equal to the volume fraction of the epoxy matrix. This interesting result is discussed in further detail in the section on Fracture Surface Morphology.

#### 5.1.2B. 828-8 System

Figure 5.8 is a plot of  $\Delta\dot{V}/V_0$  versus  $\epsilon_1$  at  $27\pm 3^\circ\text{C}$  with varying rubber content. The curves again show an initial constant  $\Delta V/V_0$  portion and some sign of voiding, although the amount of voiding that increases with rubber content is not as obvious as in the 828-15 system. The 828-8(20) material shows evidence for shear flow even at low  $\epsilon_1$ . The effect of strain rate on the 828-8(20) material is shown in Figure 5.9. Here again increasing strain rates retard the shear flow process and promote voiding.

At  $-16 \pm 2^\circ\text{C}$  the volume strain behavior is shown in Figure 5.10. There is no rapid voiding as exhibited by the 828-15 system. At a given  $\epsilon_1$ , increasing rubber content suppresses the volume strain. The 828-8(20) does void gradually. Figure 5.11 shows the effect of strain rate on  $\Delta V/V_0$  for the 828-8(20) material. Accelerated void growth is evident after  $\epsilon_1 = 3\%$ , but the trend with respect to strain rate is not clear. The volume strain behavior for the 828-8(20) material at  $65 \pm 2^\circ\text{C}$  is shown in Figure 5.12. At the lowest strain rate shear flow begins very early, so that an initial constant  $\dot{\Delta V}/V_0$  portion is barely noticeable.

#### 5.1.2C. 828-BPA(24)-8 System

Figure 5.13 is a plot of  $\Delta V/V_0$  versus  $\epsilon_1$  at  $25 \pm 3^\circ\text{C}$  with varying rubber content. At 5 and 10 phr rubber the  $\dot{\Delta V}/V_0$  curves show a constant  $\Delta V/V_0$  portion and then the onset of the shear flow process. At 15phr the  $\Delta V/V_0$  curve exhibits only a constant  $\dot{\Delta V}/V_0$  behavior. The effect of strain rate on the volume dilation behavior of the 828-BPA(24)-8(15) material is shown in Figure 5.14. Two distinct types of behavior are noted. It is evident that the shear process is very rate sensitive in this material. High strain rates retard shear and promote voiding. Figure 5.15 is a plot of  $\Delta V/V_0$  versus  $\epsilon_1$  for the 828-BPA(24)-8(15) material at  $-16 \pm 2^\circ\text{C}$  for strain rates of  $32 \times 10^{-1} \text{sec}^{-1}$  and  $3.2 \times 10^{-4} \text{sec}^{-1}$ . At this low temperature the shear process is suppressed even at the low strain rate of  $3.2 \times 10^{-4} \text{sec}^{-1}$ .

#### 5.1.3 Summary of Volume Dilation Results

The results presented exhibit several patterns in behavior:

#### 5.1.3A. The effect of rubber content

Increasing rubber content invariably prolonged the initial constant volume strain rate, and, therefore, presumably homogeneous dilatation, region. Subsequent behavior depended on the strain rate and temperature. It appears that increasing rubber content also increased total final volume strain. This is confirmed by SEM micrographs to be shown later. It is difficult to determine from these results alone if particle-particle interaction increases with rubber content. This question will be taken up again in the final section.

#### 5.1.3B. The effect of strain rate

In most cases the effect of strain rate was surprisingly significant. At low rates some of the rubber-modified materials behaved no differently from the neat resin. The accelerated voiding process was evident only at higher rates. Except at the lower temperatures, the voiding region was sometimes followed by a region of decreasing volume strain rate. This is strongly indicative of shear localization promoted by the presence of numerous voids. The effect of strain rate on the neat resins showed that localized (inhomogeneous) deformation, i.e., shear banding, was retarded by high rates. When the rubber particles are added the ability of the matrix to form shear bands was enhanced by these stress concentrators. However, as inhomogeneous shear deformation became increasingly difficult with high rates, the hydrostatic tensile stress was unrelieved. At this point, either interfacial failure between the rubber and the matrix, or cohesive failure in the matrix or the rubber itself had to take place, resulting in the accelerated volume strain. SEM micrographs in the Fracture Surface Morphology section give conclusive evidence that the

hydrostatic tensile stress was relieved by cavitation and fracture of the rubber particles.

#### 5.1.3C. The effect of temperature.

The low and high temperature experiments were performed both to discover the behavior of these materials at various temperatures and to ensure that the tensile experiments cover the same effective strain rate range as in a fracture experiment. The low temperature results shown here are dramatically different from the room temperature results in that the region of accelerated voiding is not followed by enhanced shear flow. The implications for fracture toughening mechanism are obvious. Fortunately, the SEM micrographs show that low temperature tensile fracture surfaces are quite unlike those obtained in SEN-3PB. Therefore, although the low temperature tensile behavior is interesting in itself, the room temperature tensile volume dilation behavior will suffice for the purpose of determining fracture toughening mechanisms.

#### 5.1.4 Discussion

There appears to be two possible mechanisms for the pre-yield decrease in volume strain rate observed in these experiments. Both of these proposed mechanisms involve shear localization, i.e., shear banding. The first proposal argues that as shear bands are formed the strain in the surrounding matrix is elastically unloaded. Since unloading reduces the volume strain, and shear banding does not, the argument goes, the volume strain rate is decreased. This proposed mechanism makes the implicit assumption that the shear bands and the surrounding matrix are connected in series. For this to be true, the shear band (or bundles of shear bands) must span the entire cross-section. Since shear bands are strain-softening (41), the material would have already

yielded, by definition. (Strain softening in these materials is described and discussed in Section 5.2) The argument can be modified to conform more closely to realistic deformation behavior, i.e., the shear bands do not span the entire cross-section. In this case, as the shear bands form, the material adjacent to them not only is not unloaded, but must actually bear an increased portion of the load, because while the shear bands strain soften, the overall load is still increasing. Thus, this argument cannot account for the pre-yield decrease in volume strain rate.

A second, more plausible, mechanism proposes that as shear bands form, the material can deform partly by a slipping process. It is easy to see that, in the hypothetical case of a rectangular tensile specimen that is criss-crossed by a pair of intersecting shear bands, each at  $45^\circ$  to the tensile axis, the specimen can deform entirely by slippage along the shear bands while the bands thicken. In this case the apparent Poisson's ratio can be as high as 1. The hypothetical situation is depicted in Figure 5.16. If, in the pre-yield region, the material contains a number of shear bands, the propagation of these bands and the attendant ease in slippage would increase the average apparent Poisson's ratio. This mechanism explains the negative slope of the volume strain curves close to yield. This proposed mechanism finds support in the shape of a typical necking rupture and in the fact that the necked material has a higher density (42).

## 5.2 Tensile Yield Behavior

### 5.2.1 Epon 828

Engineering stress-strain data were obtained simultaneously with the

volume dilatation data during the tensile tests. In the interest of brevity not all the stress-strain curves are shown in this report; only those that represent typical effects of the variables are presented.

Figure 5.17 shows the behavior of the Epon 828 neat resin at  $\dot{\epsilon} = 3.2 \times 10^{-5} \text{ sec}^{-1}$ . Several volume dilatation curves are included as an aid in interpretation. The pronounced maximum and subsequent drop in the nominal stress is impressive. From the amount of volume dilatation (0.4%) and tensile strain at yield (4.2%), it can be calculated that the true yield stress is higher than the nominal stress by only ~3.8%. By assuming that the material deforms after the yield point at constant volume, the correction for true stress is only an additional ~3.3%, i.e., a total correction of 7.1% at rupture. Thus, the true stress behavior also exhibits a pronounced intrinsic strain softening effect. According to Bowden (41,42), this strain softening is due to the formation of shear bands. Visual inspection of the tested specimens confirmed the formation of shear bands. This observation corroborates the statement made in the last section on the volume dilatation curves, where the leveling off and subsequent decrease of the  $\Delta \dot{V}/V_0$  curve is interpreted to be the result of shear band formation.

#### 5.2.2 828-BPA

Results for the BPA modified Epon 828 neat resin are shown in Figure 5.18. By comparison with Epon 828, this material has a lower modulus, reaches the maximum in the nominal stress at a slightly higher strain, and exhibits a less pronounced intrinsic strain softening. Shear bands were also observed in the tested specimens. The effect of strain rate was to delay the departure

from approximate linearity in both the stress and the volume strain. The deviation from linearity in the stress strain curves is clearly due to the formation of shear bands even before the maximum in stress is reached. The shear banding process in this material is more severely retarded by increasing strain rate than in Epon 828.

### 5.2.3 Effect of Rubber Content

Adding rubber particles has the expected effect, viz., both the Young's modulus and the nominal yield stress decreased with increasing rubber content. This situation is shown in Figures 5.19, 5.20 and 5.21. These Figures show that at the testing conditions given, increasing rubber content did not significantly increase the elongation to break. It will be shown later that strain rate has a more significant effect on ductility. Figure 5.22 shows that the modulus of the 828-BPA(24)-8(15) system deviates from linear behavior. This is probably due to the significant difference in the morphology of the rubber particles, viz., the existence of glassy inclusions. This effect is also seen in the yield stress, shown in Figure 5.23. The yield stress of the 828-15 system also shows significant deviation from linearity, and is lower than the yield stress of the 828-8 system by ca. 5-10%, except at 20 phr rubber. Since the moduli of the two systems are very similar, this lowering of yield stress must be due to non-linear processes that occur near yield. The broad distribution of particle sizes in this system, which resulted in small interstitial particles inbetween the larger particles in the 5, 10 and 15 phr systems, may be the cause for the reduction in yield stress. The effect of void size distribution on yield and ductility of elasto-plastic solids has been investigated (43), with theoretical results that generally agree with the observa-

tions made here. The particle size distribution of the 828-15(20) system is more uniform, hence its yield stress is nearly the same as that of the 828-8(20) system, which also has a very uniform particle size distribution.

#### 5.2.4 Effect of Strain Rate

The well-known effect of strain rate on the yield stress is also observed in these experiments. Figures 5.24 to 5.29 show the behavior of the various systems studied. It is seen in Figures 5.24 and 5.25 that the effect of strain rate on the initial modulus is minor, but the effect on the yield stress is quite significant. As in the case of the neat resins, the effect on the mode of deformation was also profound. These materials changed from shear banding at low rates to voiding at high rates. At the highest rate tested, when the true stress is estimated from the volume strain, it is readily seen that very little "intrinsic" strain softening has taken place. This observation, however, is somewhat misleading, as voiding processes probably obscure what shear banding may be occurring. Of course, as has been pointed out earlier in this section, at high rates the matrix is inherently less prone to shear band formation. The failure of the matrix to form shear bands may actually encourage deformation by inhomogeneous bulk processes to dissipate the strain energy.

The strain rate dependence of the yield stress of the various materials can be described approximately as log-linear. This relationship is shown in Figures 5.26 to 5.29. The slight curvature could be due to an intrinsic distribution in the time constant of the flow processes, or it could be an artifact caused by plotting the nominal stress rather than the true stress. It can be readily demonstrated that since the volume dilatation at yield is

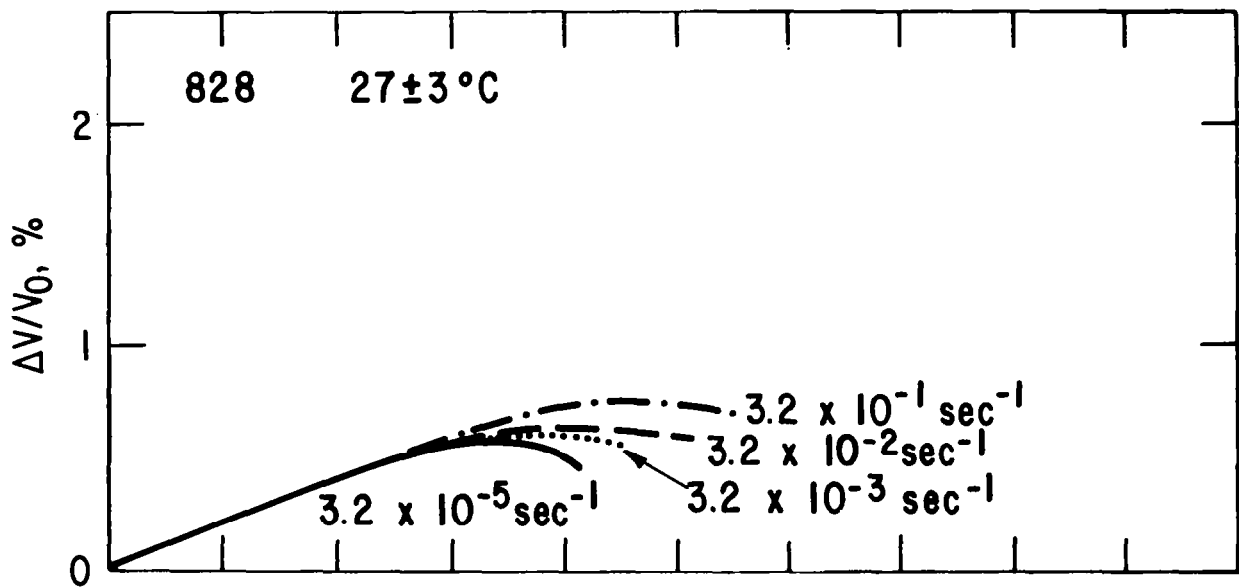
rate dependent, the amount of true stress correction is also rate dependent. In the rubber-modified systems, the deformation mechanism has already been shown to be rate dependent. It is not surprising, therefore, to find that the slopes of the curves in Figures 5.26 to 5.29 are different from those of the neat resins.

#### 5.2.5 Effect of Temperature

The effect of temperature on the yield behavior of the various epoxies is shown in Figure 5.30 to 5.36. At  $-16^{\circ}\text{C}$  all epoxies tested broke brittly in the sense that little average plastic strain was observed. Nevertheless, as can be seen in Figure 5.35, significant deformation on the micro-scale has occurred. The large increase in volume strain is accompanied by a significant and abrupt decrease in the slope of the stress-strain curves. The cause for this behavior is discussed in some detail in the Fracture Surface Morphology section. The effect of higher temperatures is, as expected, to enhance the shear flow process immensely.

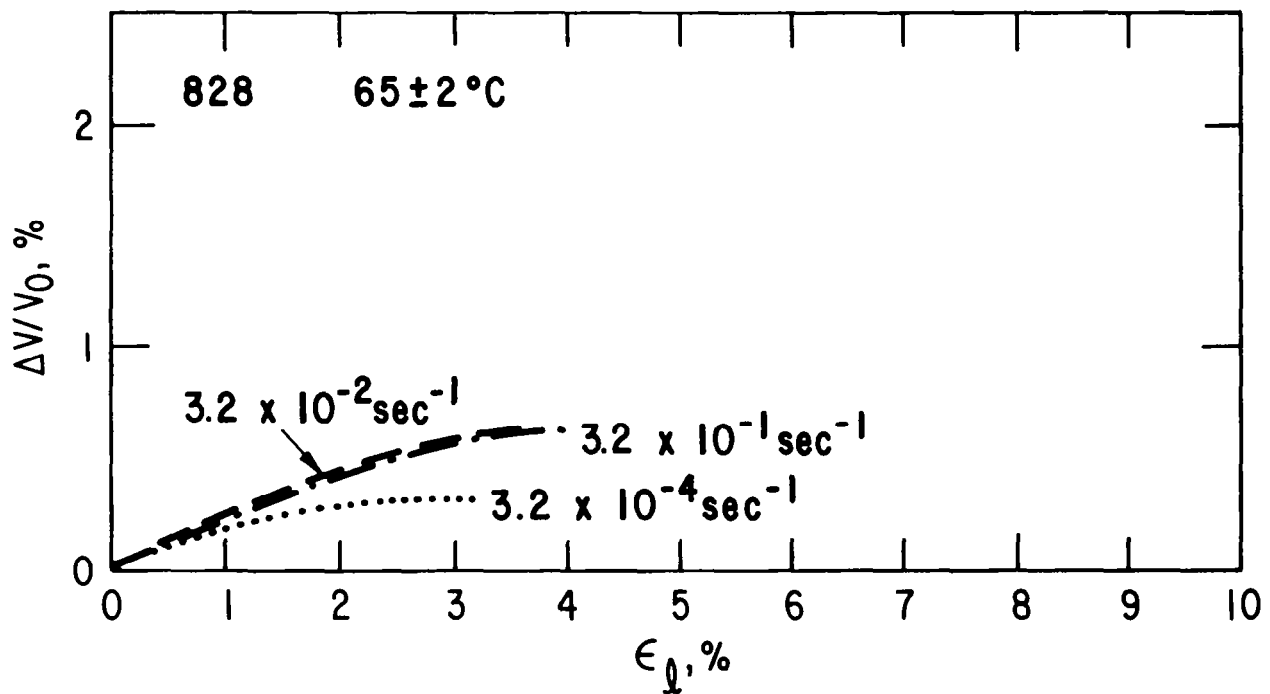
### 6. FRACTURE SURFACE MORPHOLOGY

SEM and back-scattered electron analysis were performed on the fracture surfaces of the various materials tested in the 3PB. Subsurface studies of the damage zone are presented in the next section. The major tool used in the following studies was an ISI Super II scanning electron microscope. SEM specimens were coated with a film of Au-Pd alloy by sputtering. Specimens for the back-scattered electron study were stained with an aqueous solution of  $\text{OsO}_4$  in tetrahydrofuran. The  $\text{OsO}_4$  preferentially adds to the double bonds in CTBN, thus providing contrast. To facilitate identification and discussion of



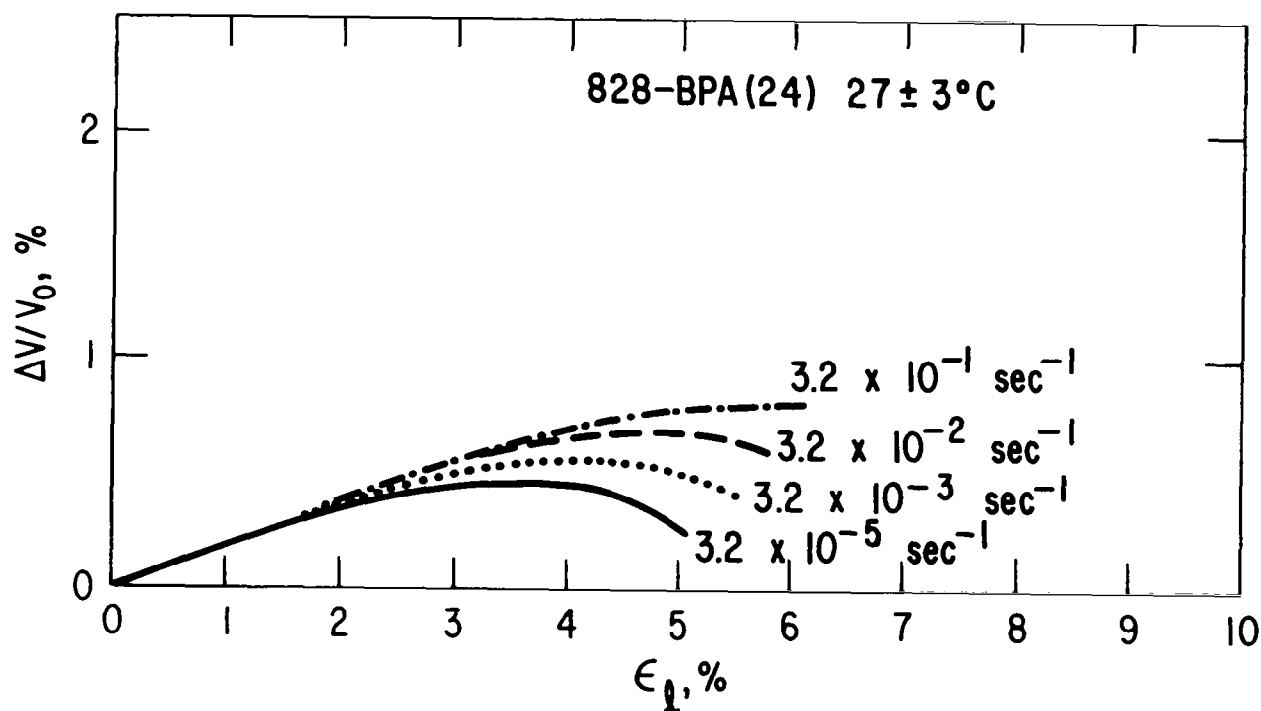
5.1 Volume Strain Behavior for 828 Material at  $27 \pm 3^\circ \text{C}$  for Several

$\dot{\epsilon}$

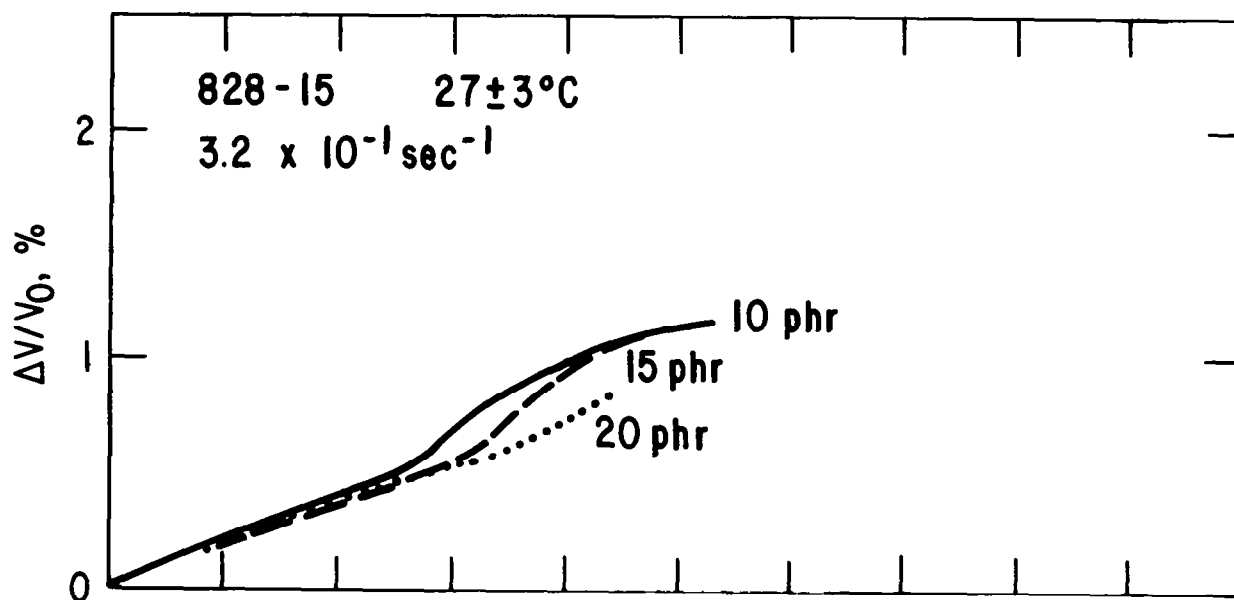


5.2 Volume Strain Behavior for 828 Material at  $65 \pm 2^\circ \text{C}$  for Several

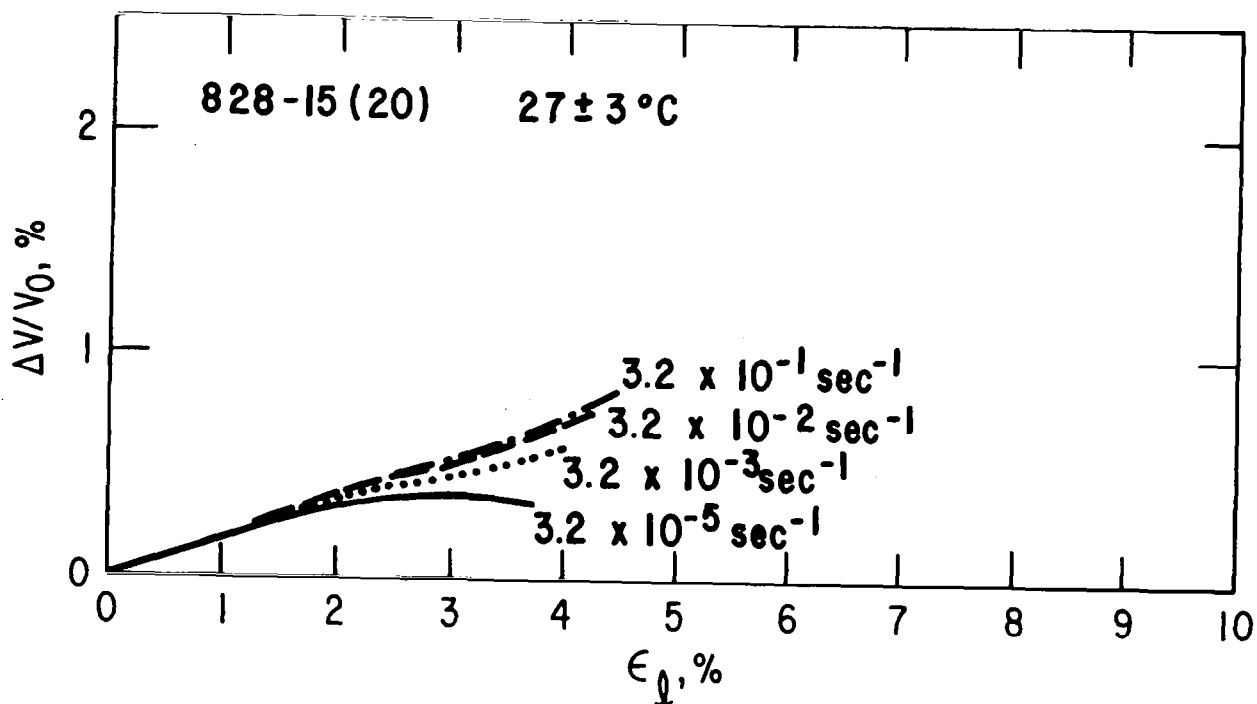
$\dot{\epsilon}$



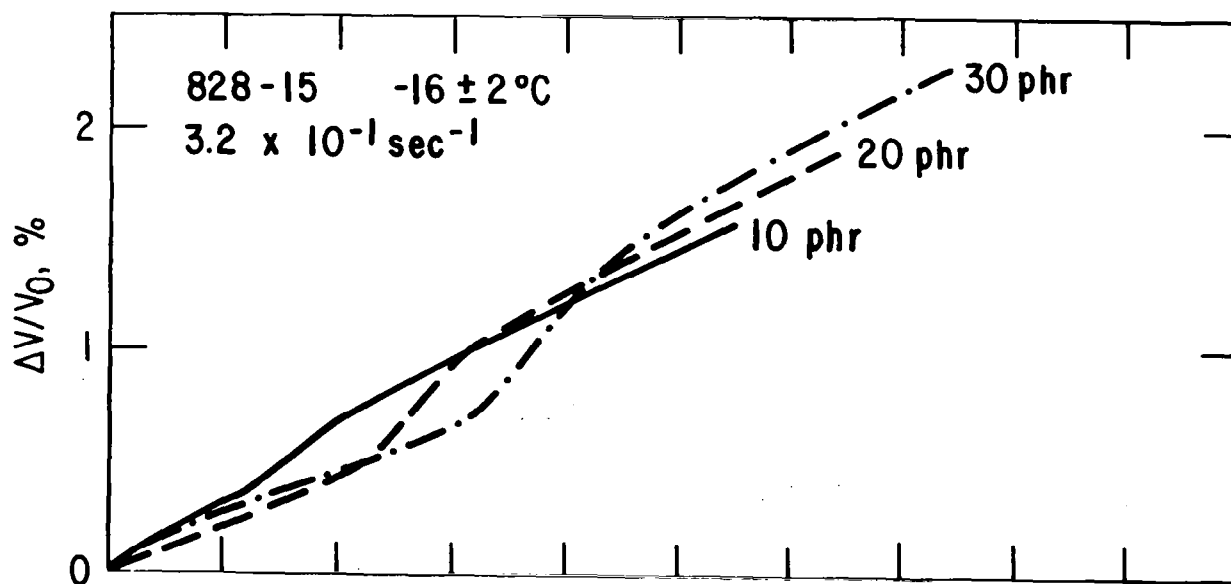
5.3 Volume Strain Behavior for 828-BPA(24) Material at  $25 \pm 3^\circ\text{C}$   
for Several  $\dot{\epsilon}$



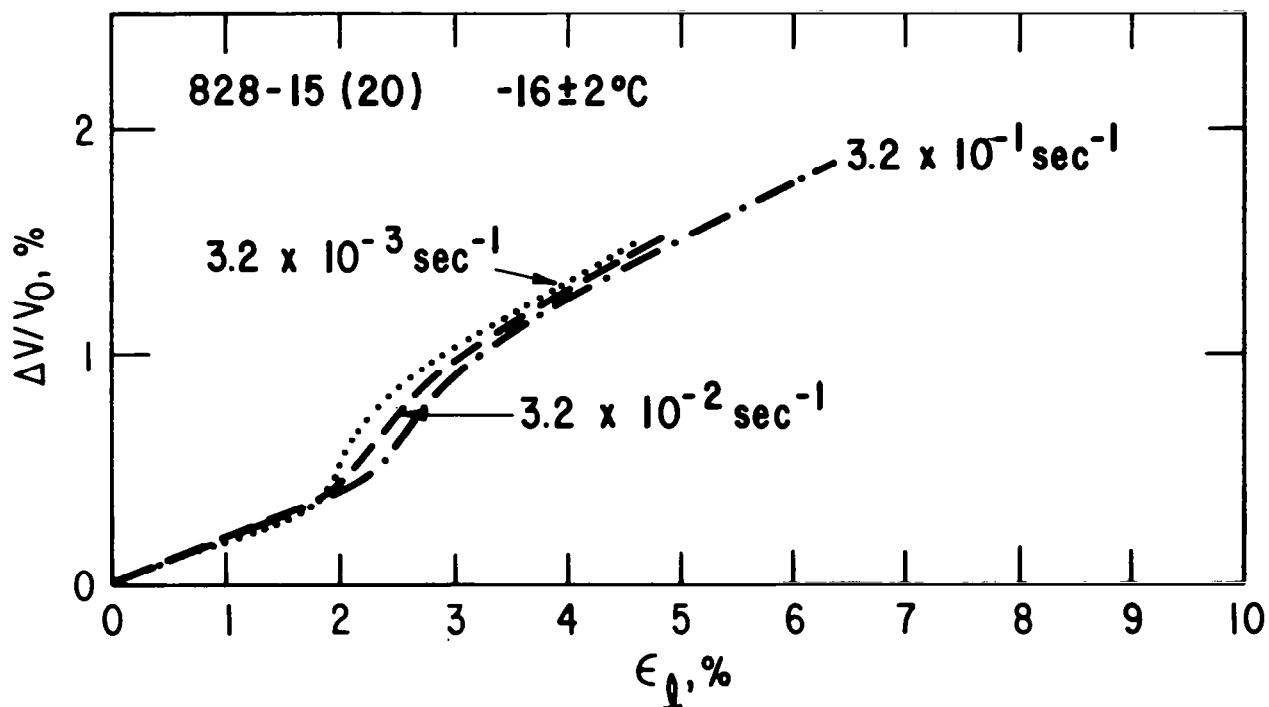
5.4 Volume Strain Behavior for 828-15 Material at  $27 \pm 3^\circ\text{C}$  for  
Several Rubber Contents



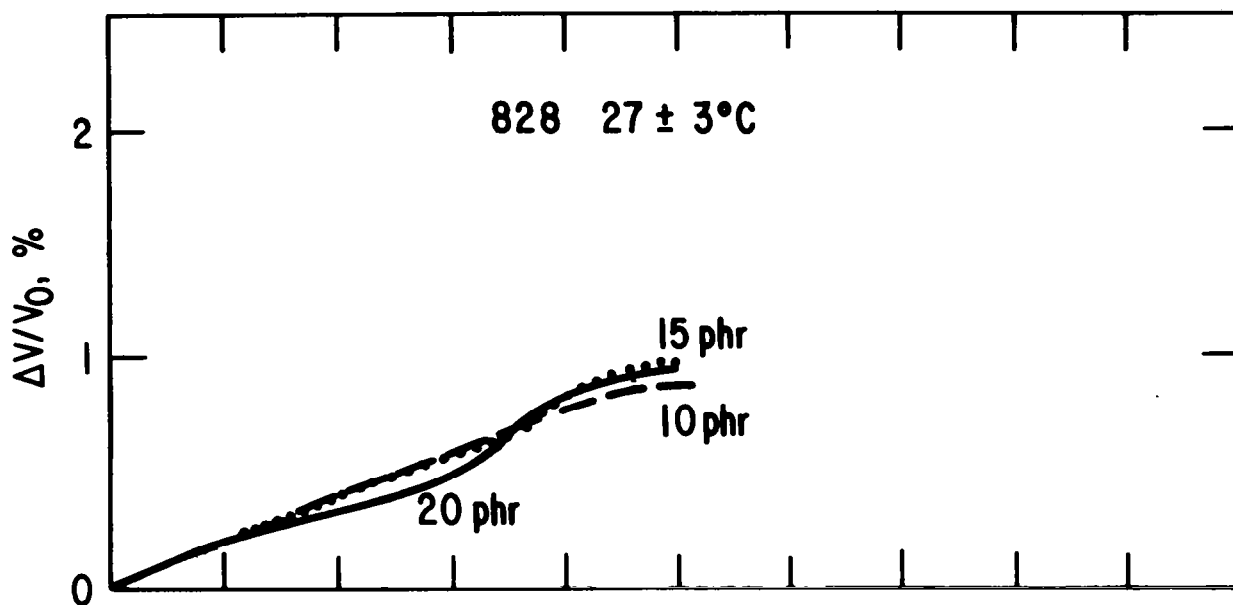
5.5 Volume Strain Behavior for 828-15(20) Material at  $27 \pm 3^\circ \text{C}$  for  
for Several  $\dot{\epsilon}$



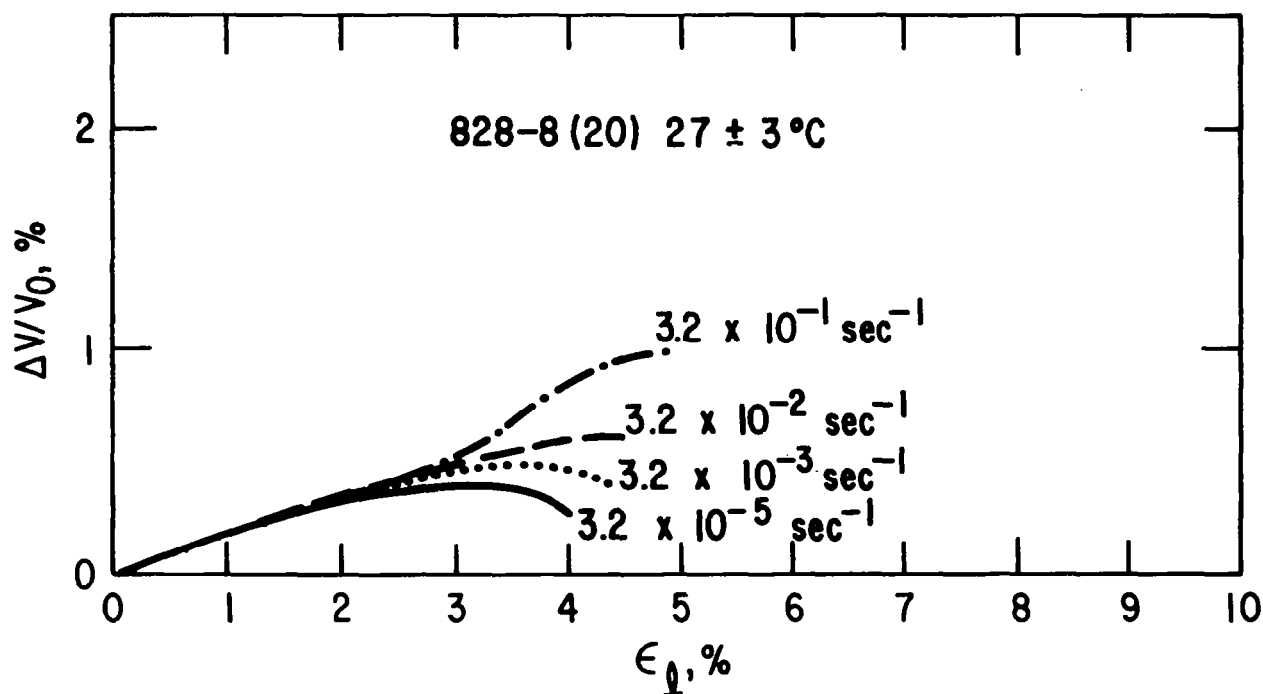
5.6 Volume Strain Behavior for 828-15 Material at  $-16 \pm 2^\circ \text{C}$  for  
Several Rubber Contents



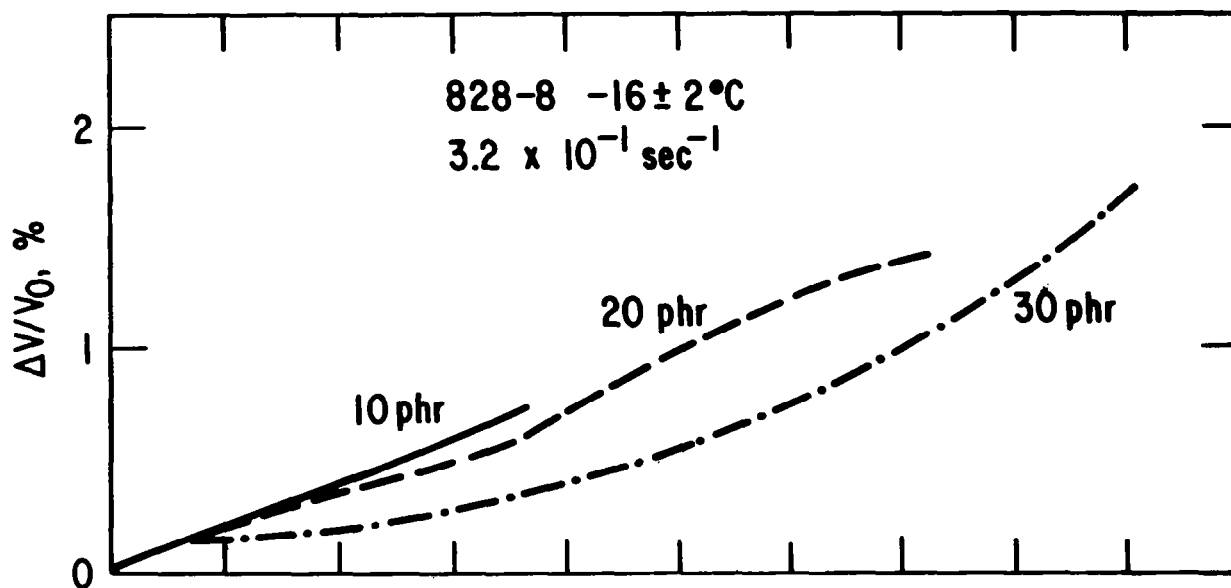
5.7 Volume Strain Behavior for 828-15(20) Material at  $-16 \pm 2^\circ\text{C}$  for  
for Several  $\dot{\epsilon}$



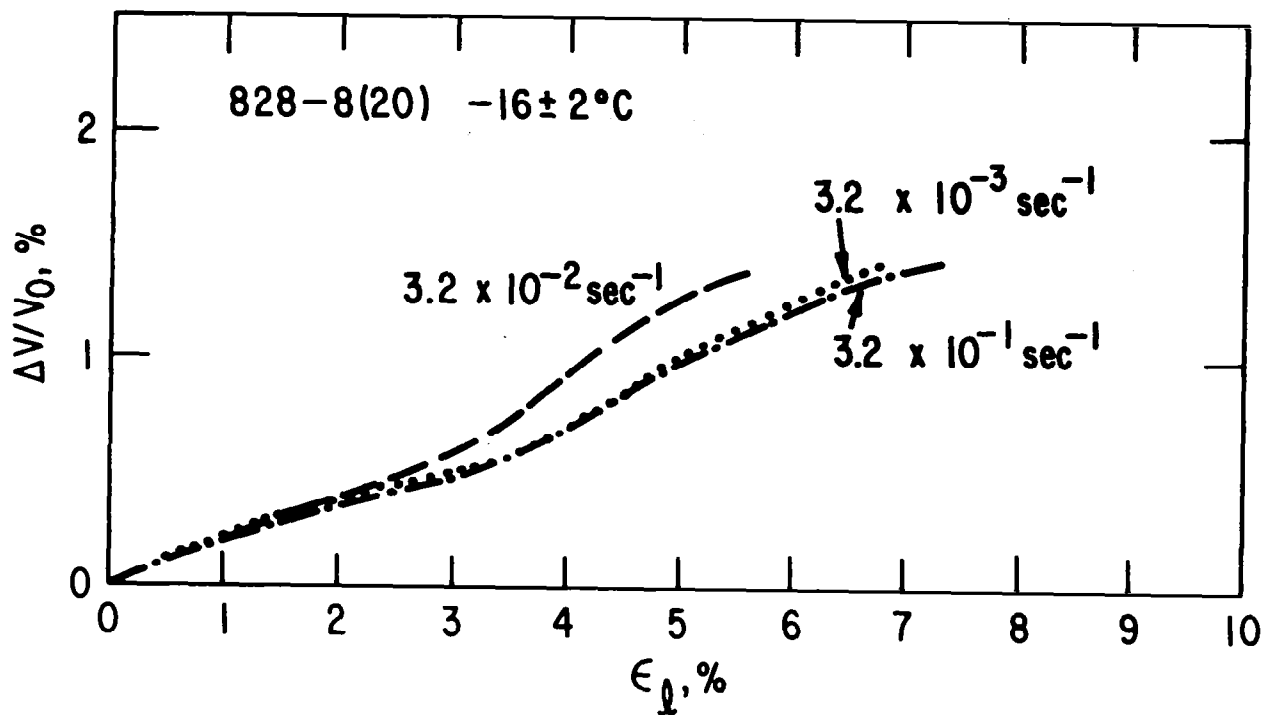
5.8 Volume Strain Behavior for 828-8 Material at  $27 \pm 3^\circ\text{C}$  for  
Several Rubber Contents



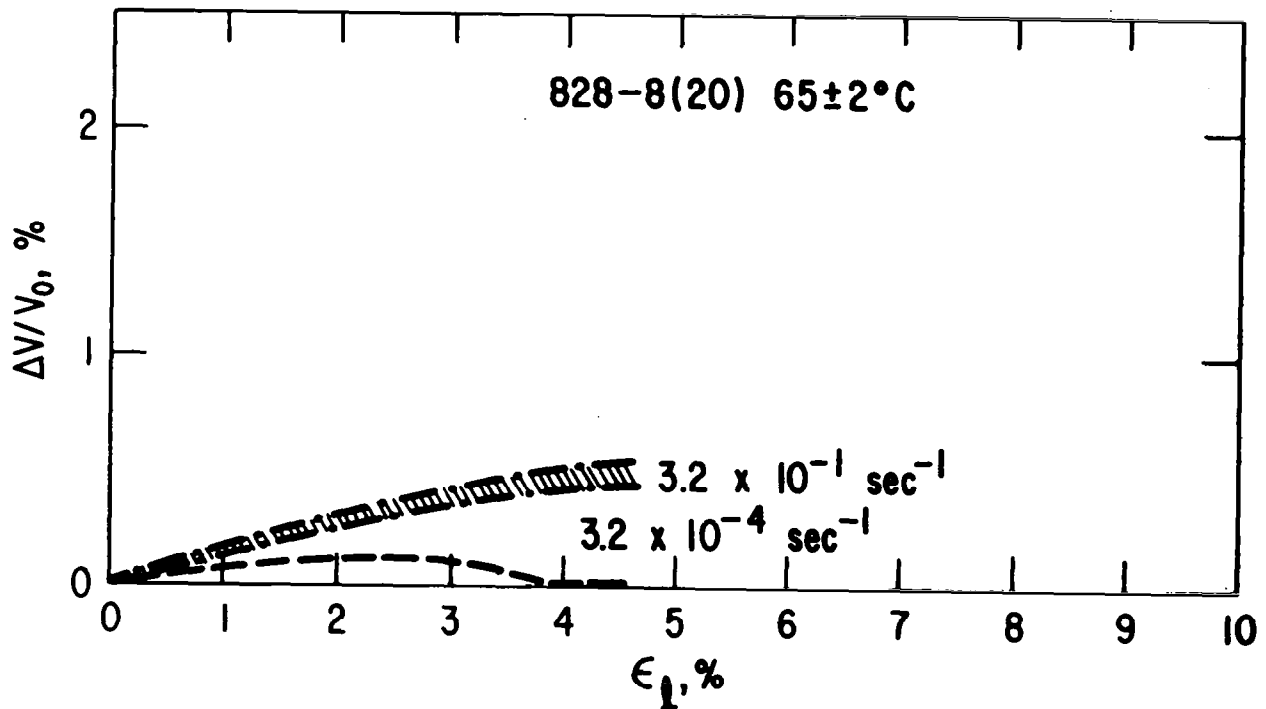
5.9 Volume Strain Behavior for 828-8(20) Material at  $27 \pm 3^\circ\text{C}$  for  
for Several  $\dot{\epsilon}$



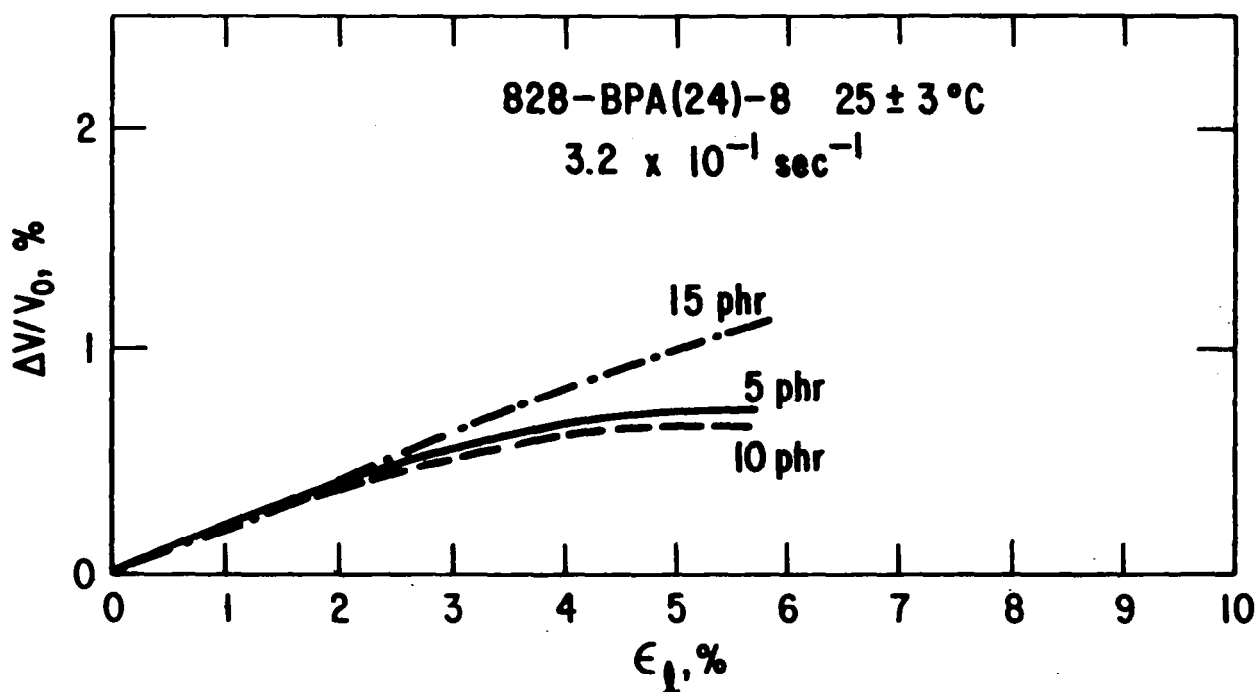
5.10 Volume Strain Behavior for 828-8 Material at  $-16 \pm 2^\circ\text{C}$  for  
Several Rubber Contents



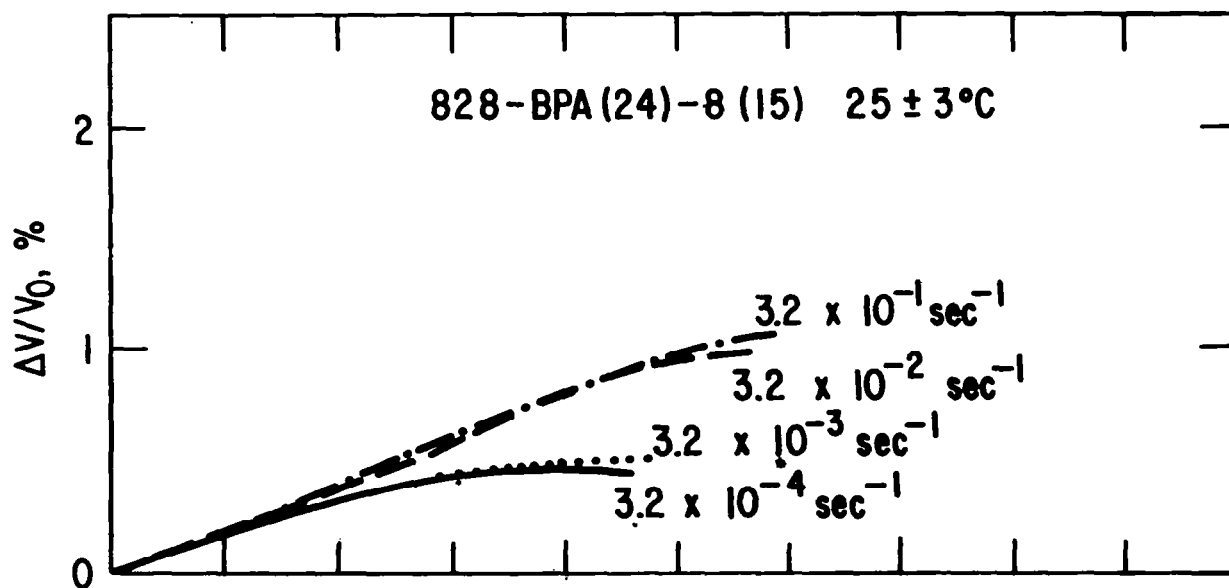
5.11 Volume Strain Behavior for 828-8(20) Material at  $-16 \pm 2^\circ\text{C}$  for  
for Several  $\dot{\epsilon}$



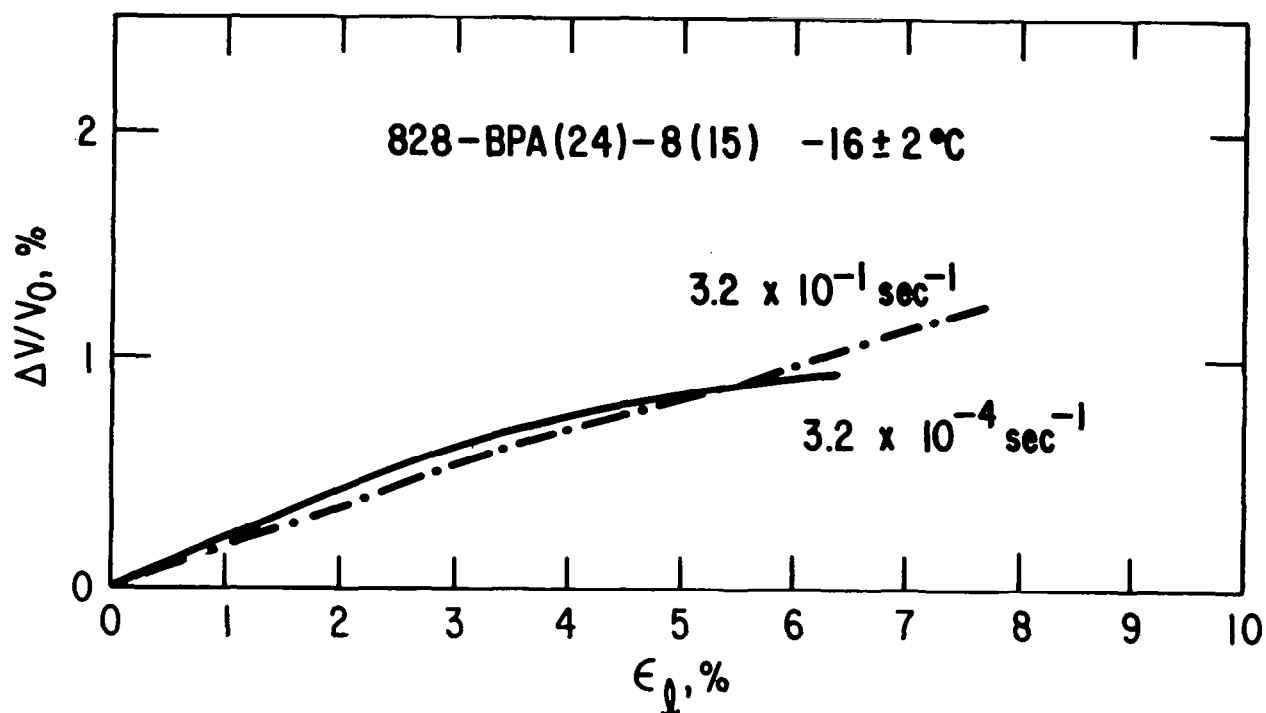
5.12 Volume Strain Behavior for 828-8(20) Material at  $65 \pm 2^\circ\text{C}$  for  
Several  $\dot{\epsilon}$



5.13 Volume Strain Behavior for 828-BPA(24)-8 Material at  $25 \pm 3^\circ\text{C}$   
 for Several Rubber Contents

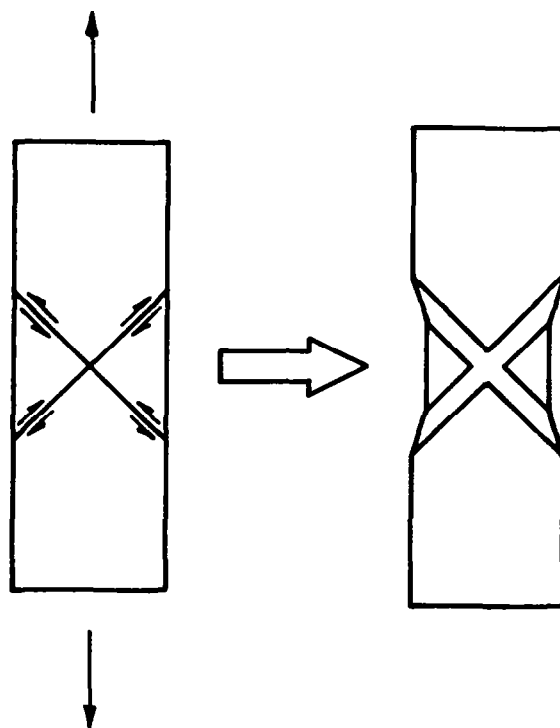


5.14 Volume Strain Behavior for 828-BPA(24)-8(15) Material at  
 $25 \pm 2^\circ\text{C}$  for Several  $\dot{\epsilon}$

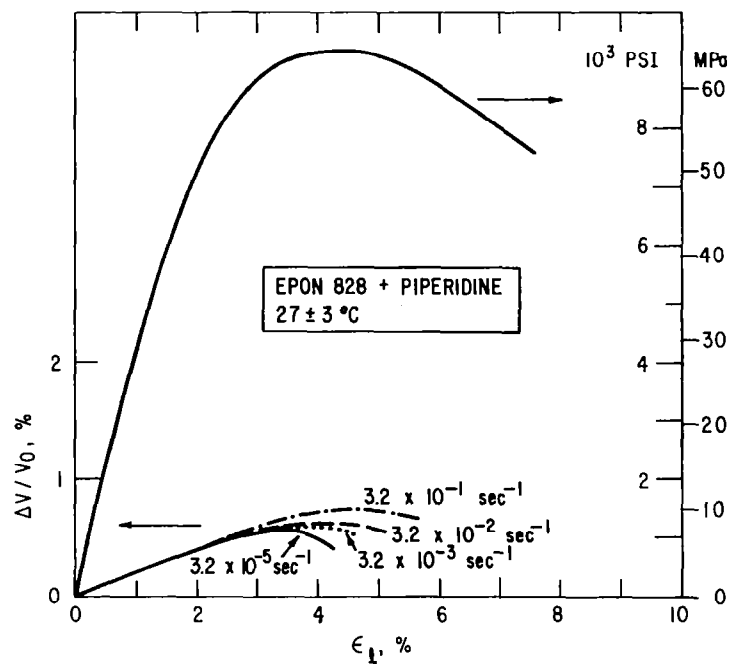


5.15 Volume Strain Behavior for 828-BPA(24)-8(15) Material at

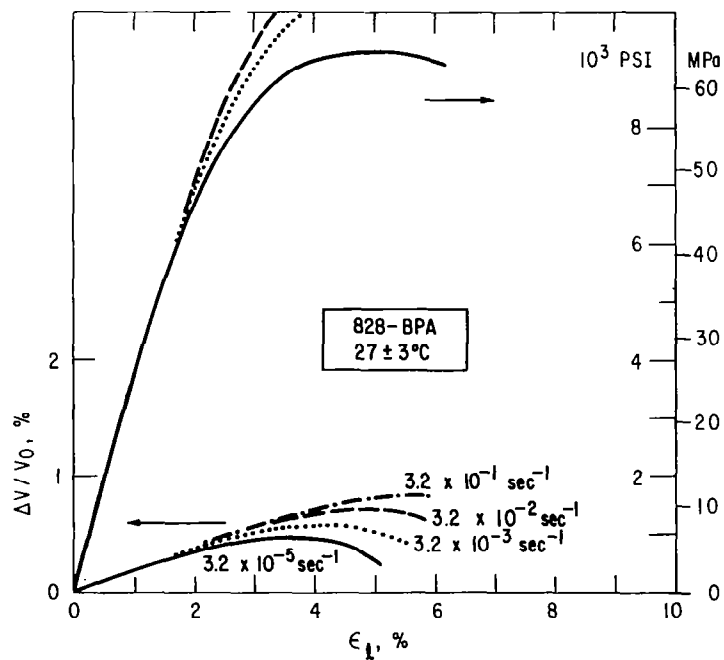
$-16 \pm 2^\circ \text{C}$  for Several  $\dot{\epsilon}$



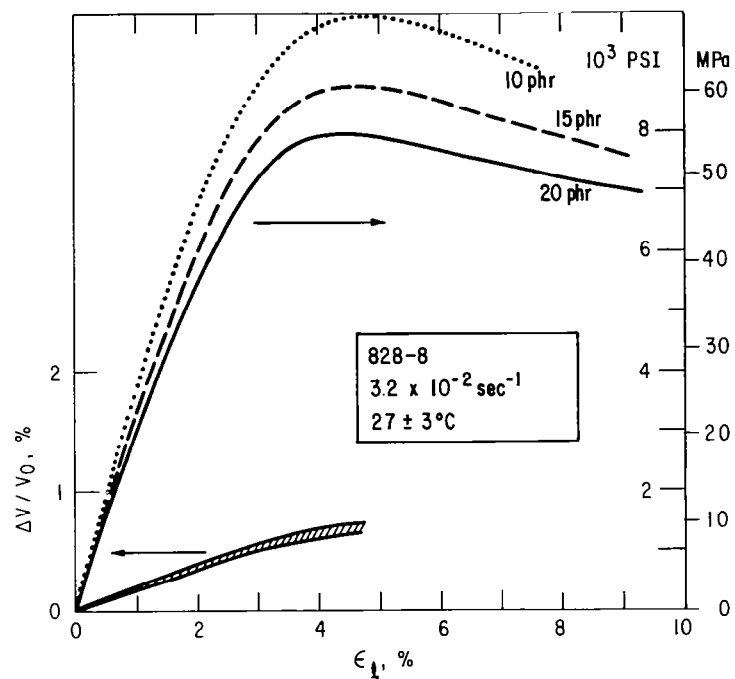
5.16 Schematic Representation of the Slipping Process in a Tensile Specimen  
With Crossed Shear Bands



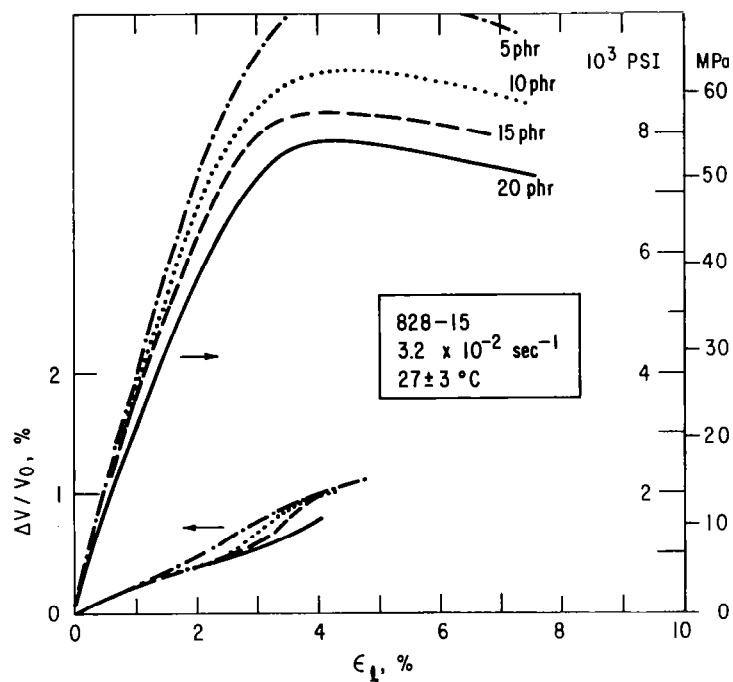
5.17 Tensile Behavior for 828 at 27±3°C



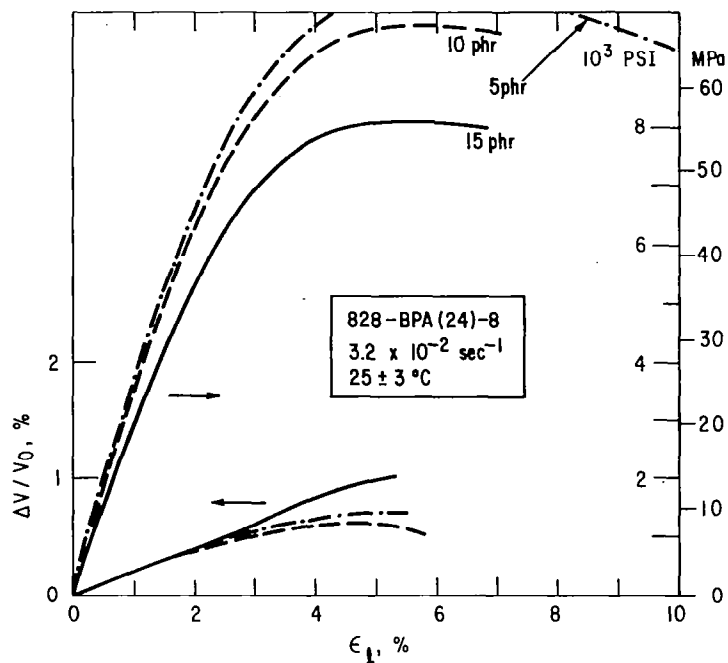
5.18 Tensile Behavior for 828-BPA(24) at 27±3°C



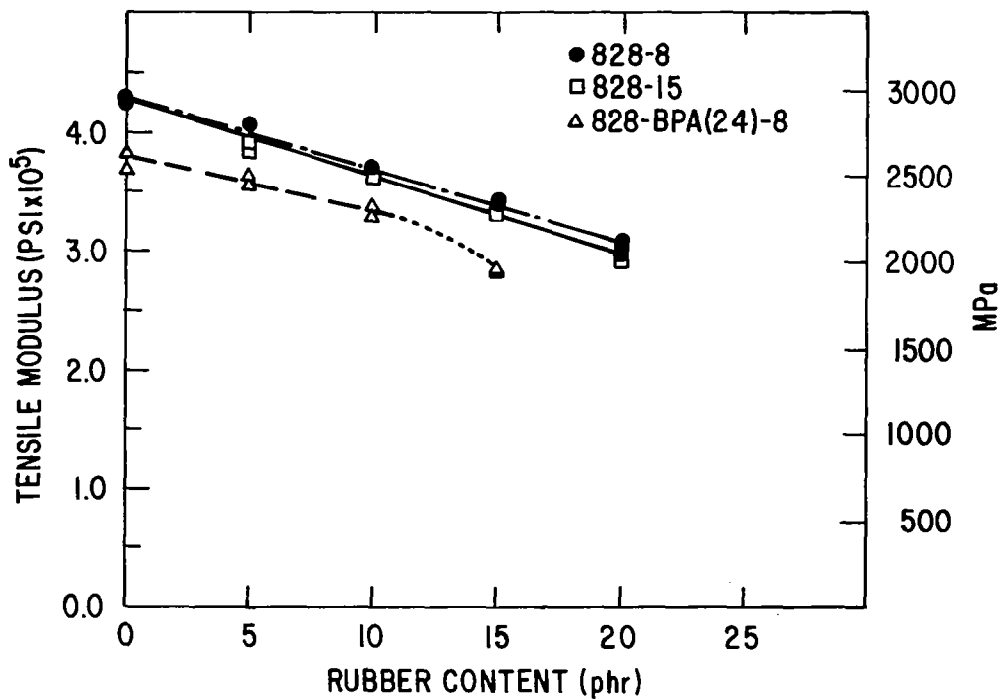
5.19 Tensile Behavior for 828-8 with Increasing Rubber Content



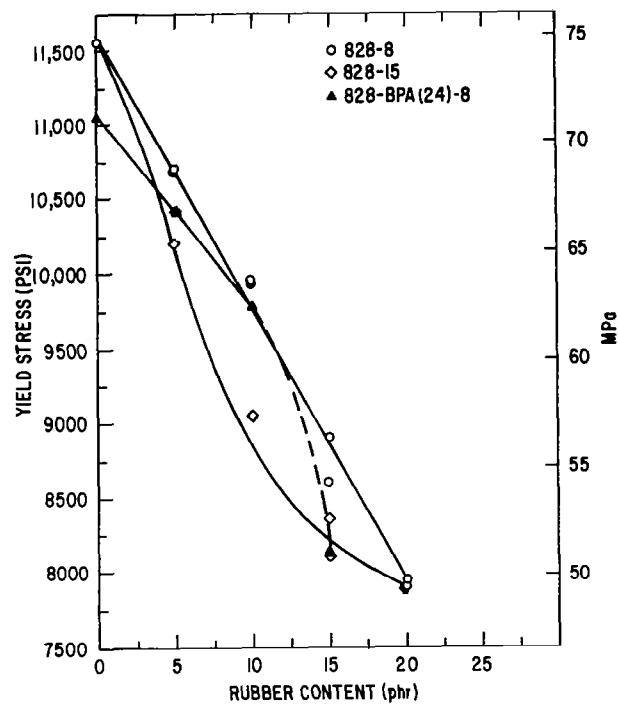
5.20 Tensile Behavior for 828-15 with Increasing Rubber Content



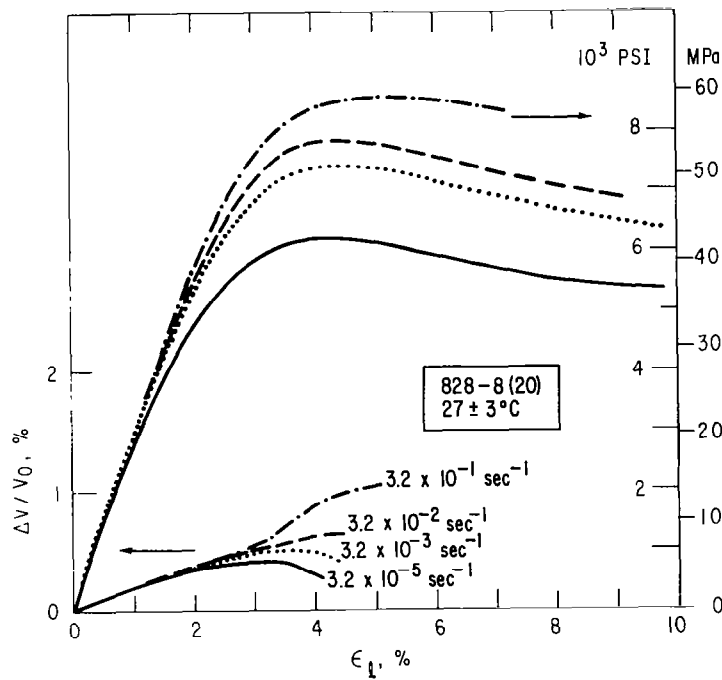
5.21 Tensile Behavior for 828-BPA(24)-8 with Increasing Rubber Content



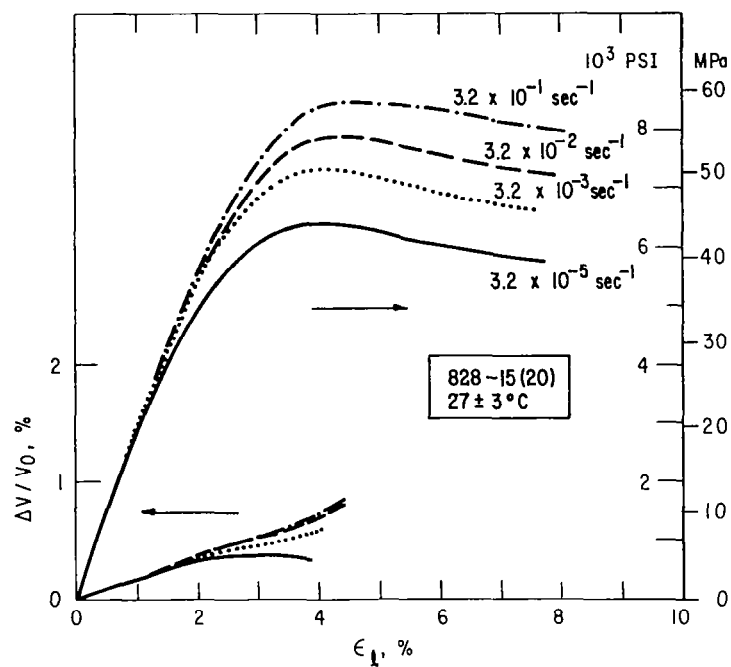
5.22 The Effect of Rubber Content on Tensile Modulus at  $27 \pm 3^{\circ}\text{C}$  at  $3.2 \times 10^{-2} \text{ sec}^{-1}$



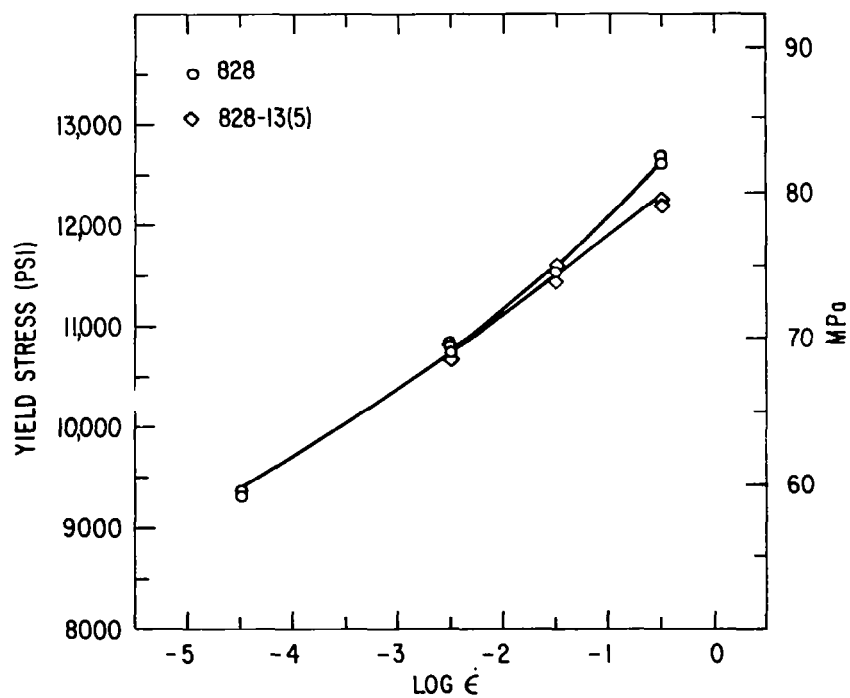
5.23  $\sigma_y$  vs. Rubber Content at  $27 \pm 3^\circ\text{C}$  at  $3.2 \times 10^{-2} \text{ sec}^{-1}$



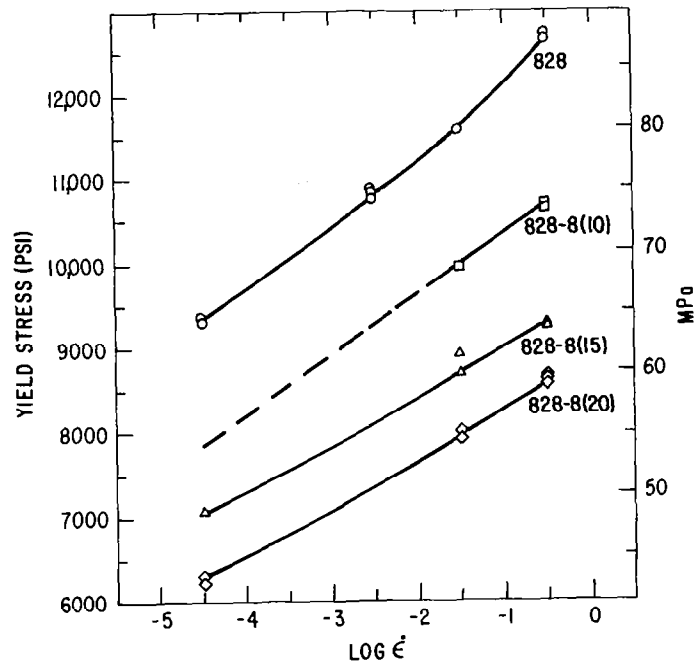
5.24 Tensile Behavior for 828-8(20) for Several  $\dot{\epsilon}$



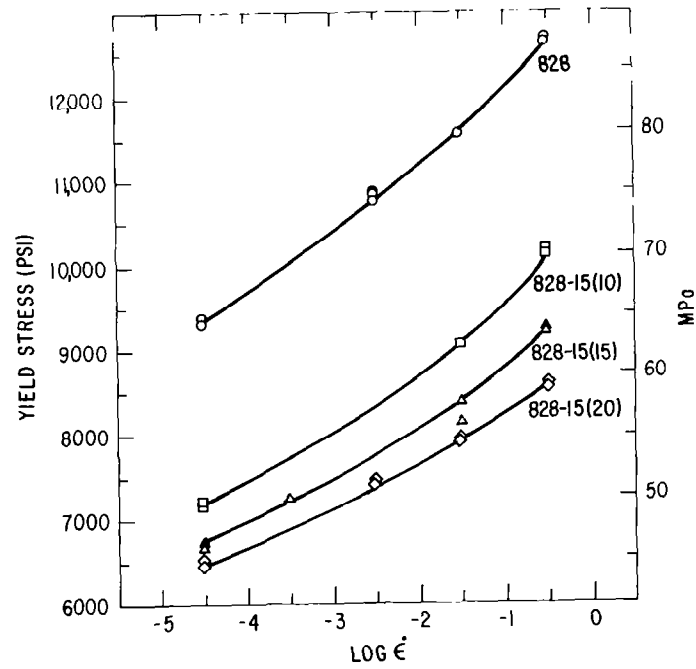
5.25 Tensile Behavior for 828-15(20) for Several  $\dot{\epsilon}$



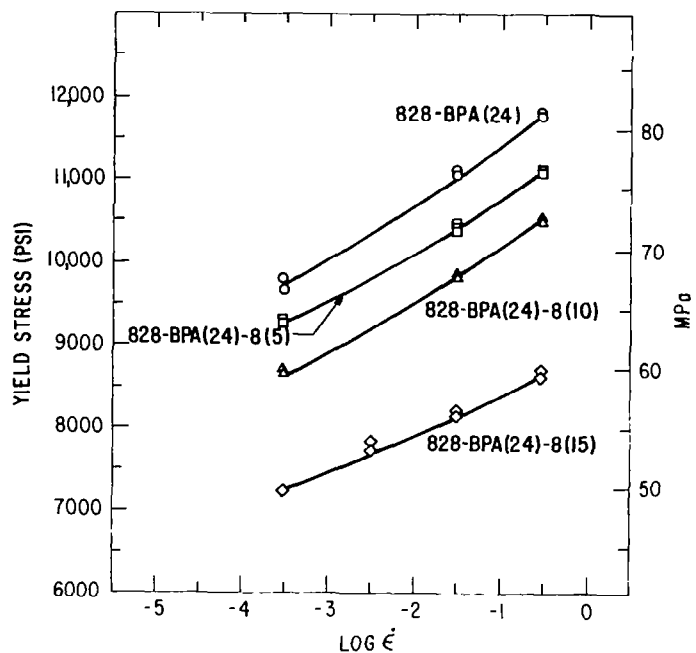
5.26 The Effect of  $\dot{\epsilon}$  on  $\sigma_y$  for 828 and 828-13(5)



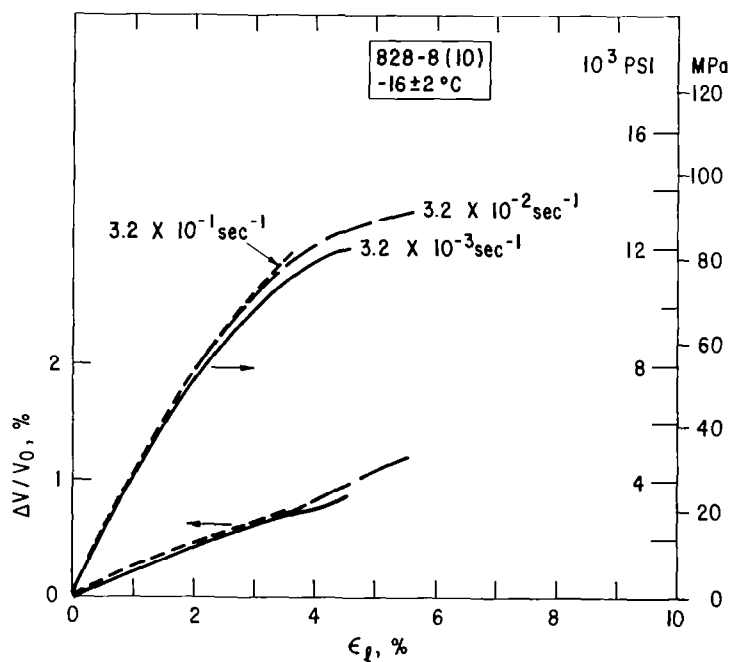
5.27 The Effect of  $\dot{\epsilon}$  on  $\sigma_y$  for 828 and 828-8



5.28 The Effect of  $\dot{\epsilon}$  on  $\sigma_y$  for 828 and 828-15

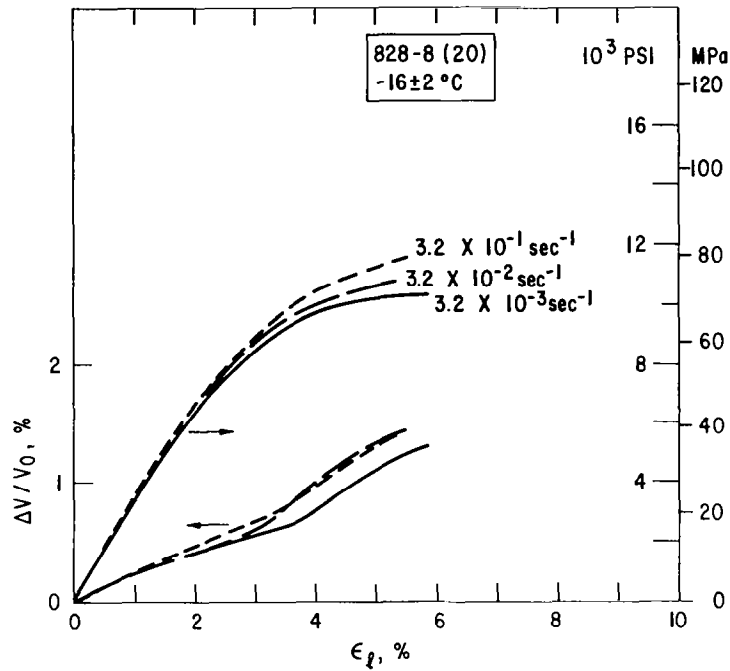


5.29 The Effect of  $\dot{\epsilon}$  on  $\sigma_y$  for 828-BPA(24) and 828-BPA(24)-8



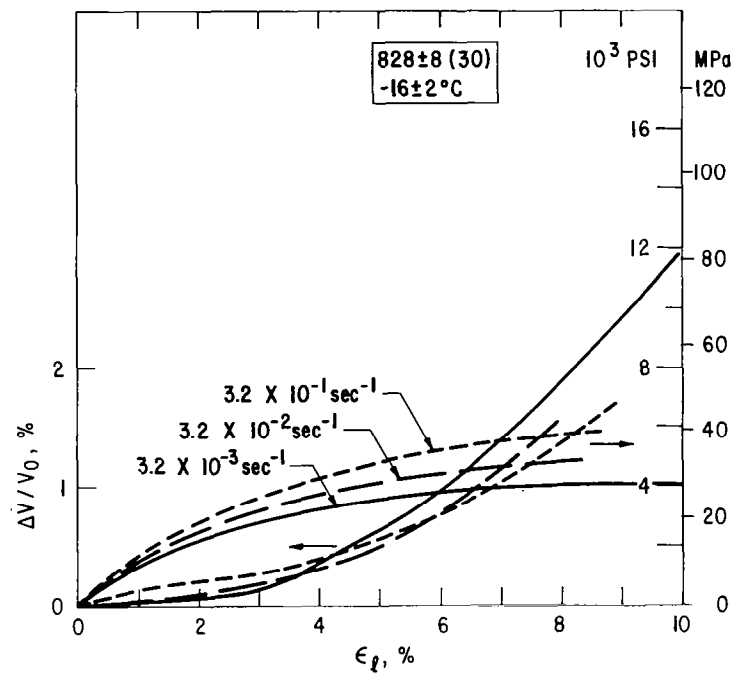
5.30 Tensile Yield Behavior for 828-8(10) at  $-16 \pm 2^\circ\text{C}$  for Several

$\dot{\epsilon}$



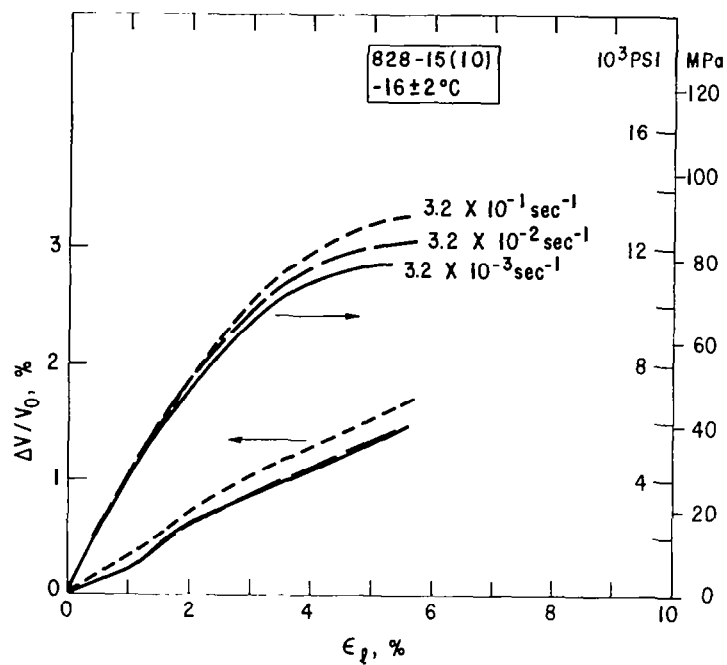
5.31 Tensile Yield Behavior for 828-8(20) at  $-16\pm 2^{\circ}\text{C}$  for Several

•  
ε



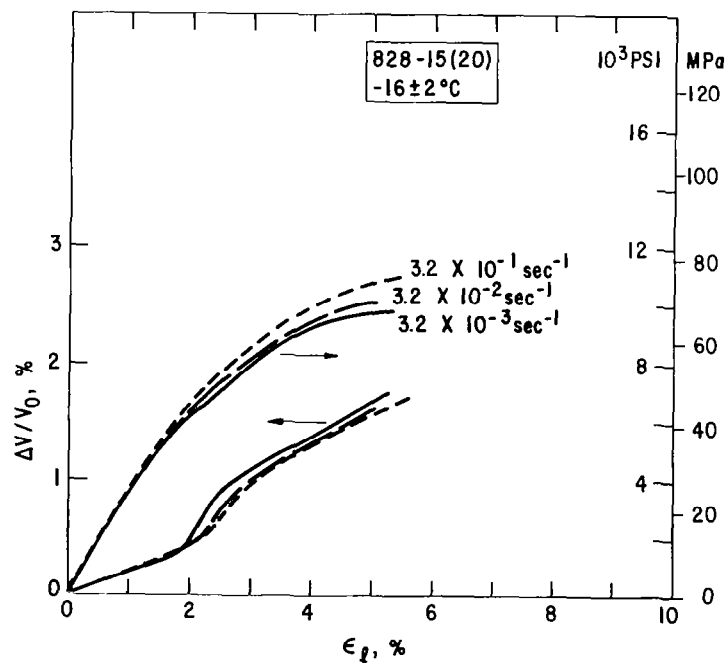
5.32 Tensile Yield Behavior for 828-8(30) at  $-16\pm 2^{\circ}\text{C}$  for Several

•  
ε



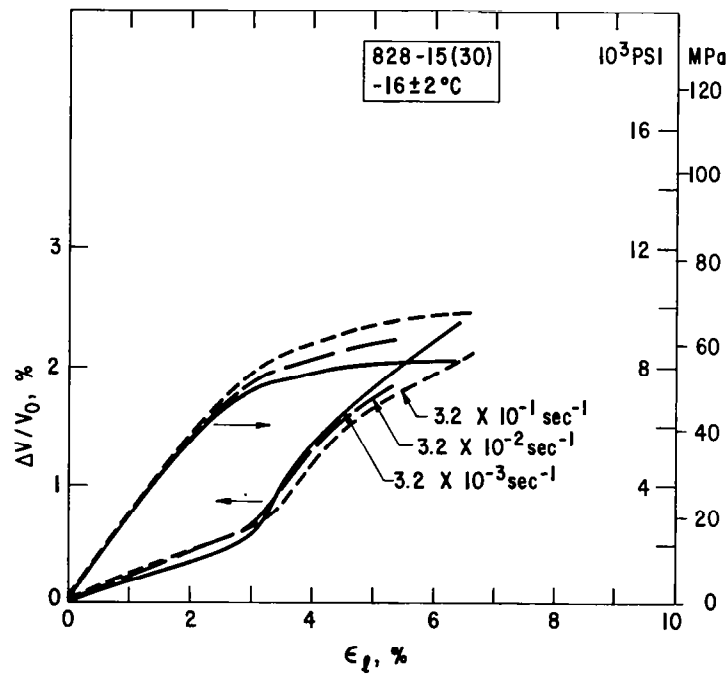
5.33 Tensile Yield Behavior for 828-15(10) at  $-16 \pm 2^\circ \text{C}$  for Several

•  
8



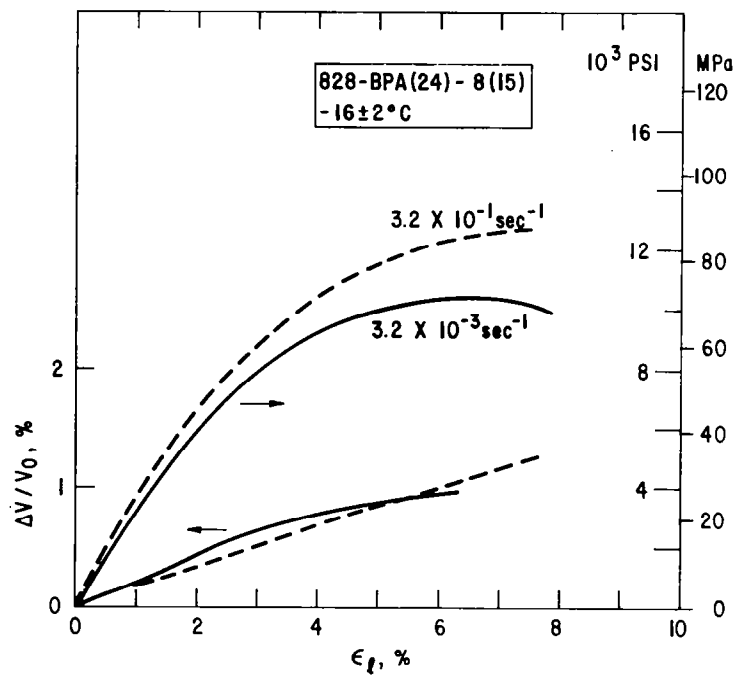
5.34 Tensile Yield Behavior for 828-15(20) at  $-16 \pm 2^\circ \text{C}$  for Several

•  
8



5.35 Tensile Yield Behavior for 828-15(30) at -16±2°C for Several

ε



5.36 Tensile Yield Behavior for 828-BPA(24) at -16±2°C for Several

ε

the micrographs obtained from different regions of the specimens, the schematic representation of the fracture surfaces is used as shown in Figure 6.1.

#### 6.1 SEN-3PB Fracture Surfaces

It is useful to recall here the SEN-3PB test. In the majority of cases the load rises linearly to a maximum, then drops as the crack propagates. In the rising load portion, the specimen develops a stress-whitened zone ahead of the starter crack. For an unstable plane strain fracture, the rising load portion accounts for the total energy, thus the stress-whitening is directly related to the energy absorbing mechanism. The subsequent rapid crack propagation leaves a fracture surface without whitening. Stress whitening is due to the scattering of visible light from a layer of scattering centers, in this case voids, as will be shown in the micrographs. The absence of whitening does not necessarily imply the absence of scattering centers, merely that the scattering layer is insufficiently thick, i.e., less than 1  $\mu\text{m}$ . Both of the fracture surfaces produced after stress whitening and that after fast fracture will be examined here.

The SEN-3PB fracture specimens of the control epoxy and that modified with CTBN 13 (5 phr) did not show any stress whitening. The fracture surfaces are basically featureless up to a magnification of 5000X, although some approximately 0.1  $\mu\text{m}$  graininess is discernible in the rubber modified material. The absence of significant visible deformation concentration in spite of the presence of the rubber correlates well with the lack of toughness improvement. Typical SEM micrographs of these surfaces are shown in Figure 6.2. In contrast, the fracture surfaces of the SEN-3PB specimens of 828-8(5)

and 828-15(5) all showed a narrow band of stress-whitening just ahead of the starter crack, followed by an unwhitened region. This type of morphology is exactly as depicted in Figure 6.1. SEM details of the stress-whitened region are shown in Figure 6.3, and the fast fracture zone in Figure 6.4. The sizes of the voids in Figure 6.4 are essentially the same as those of the rubber particles in undeformed specimens as determined by transmission electron microscopy. By comparison the sizes of the voids in the stress-whitened zone are significantly larger. No major difference in fracture morphology is discernable between the two materials, even though the CTBN 15 particles are two to three times larger in diameter than the CTBN 8 particles. The relative uniformity of the voids in the stress-whitened region implies that the cracks preferentially travelled along the equatorial planes of the particles relative to the major principal stress direction. Since the particles are not all on the same plane, fracture steps are developed on the surface, corresponding to different equatorial planes all approximately parallel to each other. The fast fracture surfaces are, on the other hand, fairly flat and contain voids of various sizes and depths. Since the crack propagates rapidly, the matrix voids do not have time to grow, hence, they are essentially of the same size as the rubber particles.

## 6.2 828-15 System

Fracture surfaces of higher rubber content 828-15 materials are discussed in this section. Micrographs from the stress whitened areas of SEN-3PB specimens are shown in Figure 6.5. Aside from the increase in the density of voids, two features are noteworthy. The first is that the void sizes in each material become more uniform with increasing rubber content. The second is that the void sizes become systematically larger, at a rate higher than the

increase in size of the rubber particles as the rubber content goes up. The first feature is simply due to the increased uniformity of the rubber particles, whereas the second is probably due to particle-particle interaction. To illustrate this point, a higher magnification SEM micrograph of the stress whitened region of 828-15(30) is examined (Figure 6.6). It is clear that the solid here resembles a closed-cell foam, and the voids are not spherical, but rather approach polyhedrons in shape. This is most likely a result of spherical void growth due to the net hydrostatic tension; the growth is retarded as the voids begin to "see" each other. The other possibility, i.e., void growth due to large shear strain, would have resulted in elongated voids.

Visual examinations of tensile fracture surfaces often reveal two fairly distinct regions as depicted in Figure 6.1, i.e., a visually smooth (but not mirror-like) area around a nucleus and a rough area around the first. The nucleus is often found near a surface, although it is depicted here in the interior of the specimen. In visual appearance the two regions correspond closely to the stress-whitened area and the fast-fracture area, respectively, of the SEN-3PB specimens. This similarity is examined in this section. The use of tensile tests to investigate toughening mechanisms in plane strain fracture is predicated upon the argument that the deformation mechanisms will be similar in both cases. This argument should be approximately correct for tensile fractures that propagate mainly in a plane; it is supported theoretically, in the case of materials whose tensile failures are preceded by inhomogeneous dilatation, in model calculations(22,44-46). More direct evidence to support this similarity is presented here. Figures 6.6 and 6.7 are high magnification SEM micrographs from the stress-whitened regions of SEN-3PB and tensile fracture surfaces of the 828-15 materials containing various amounts

of rubber (as noted in the figure captions), respectively. These specimens were tested at room temperature. The diameters of the voids are generally larger than those of the undeformed particles, as determined by TEM (see Figure 3.5 and 6.8). This is undoubtedly due to the cavitation of the particles and the matrix surrounding them. Figure 6.8 shows that cavitation of the particles caused increases in diameter from ca. 50-200% in the case of the SEN-3PB fracture surfaces. The same figures shows that the diameter of tensile fracture voids are larger than the undeformed particles by at least 50%, at 5 and 10 phr rubber. However, at 20 phr the rubber particles are virtually unchanged in diameter to within measurement uncertainty. This is undoubtedly due to the fact that at such a high rubber content, the tensile deformation is essentially by shear. (see 5.2). The fractured rubber particles are notably different in the two types of surfaces. Figure 6.7 shows that in the tensile case, the particles appear to have failed in a cup-and-cone type of fracture, presumably after a cavity has been initiated in the center of the particle. However, these cup-and-cone pairs appear to be, in turn, surrounded by disc-shaped cavities which may originally have been deeper just prior to total separation but have elastically relaxed afterwards. Note that the epoxy matrix around these voids is very flat, showing little sign of plastic flow. The steps on the surface hint at the existence of sub-surface damage. Many of these features are corroborated by OM and TEM in later sections. In the SEN-3PB case, (Figure 6.6) the rubber particles appear to have failed by cavitation. The voids are all concave. Most voids also have a clearly defined hole in the center. As noted before, the voids are significantly larger than the undeformed particles. The matrix surrounding the voids exhibits notable deformation, viz., the sloping inward at the edge of the voids. This plastic deformation becomes larger as the particle-particle distance decreases, which,

as noted in the previous section, is clear evidence for particle-particle interaction. In Figure 6.6c and d, where the voids are quite close together, the sloping zones actually intersect each other, forming fairly sharp ridges between neighboring voids. The features observed on the two types of fracture surfaces can be qualitatively described by theoretical models on ductile fracture in voidy elasto-plastic solids.(22,46) The application of this type of theory to the present study is presented in the final section. In spite of the differences noted, the two types of fracture surfaces are actually quite similar, thus lending credence to the tensile dilatometry experiments. Two energy dissipation processes are observed in these SEMs: the cavitation and fracture of the rubber particles, and the dilatation and the plastic deformation of the surrounding matrix near the surface.

### 6.3 828-8 System

Figures 6.9 and 6.10 are SEM micrographs from both the slow and the fast crack growth regions of tensile and SEN-3PB fracture surfaces of the 828-8 materials. These specimens were also tested at room temperature. Here the fracture surfaces of the two types of specimens are virtually indistinguishable. Both slow crack growth regions show hemispherical voids. Both fast crack growth regions show very shallow disc-shaped cavities. The slow-growth voids are larger in diameter than those in the fast crack regions, where the particle sizes remain about the same as the undeformed particles as determined by TEM. The fracture morphology of these CTBN-8 particles is in strong contrast to that of the CTBN-15 particles. The CTBN-8 cavities are quite smooth and featureless, but the wall of the voids is actually lined with a layer of rubber. This will be shown to be the case when the back-scattered electron analysis is presented later. Thus, the rubber particles appear to have

cavitated and then "ballooned" out with the growing void in the matrix. The difference in the cavitation and failure behavior of the CTBN-15 and CTBN-8 rubber particles may be attributed to the difference in effective cross-link densities. As mentioned previously, the 828-15 system precipitates out larger volume fractions of rubber than predicted by calculations based on total precipitation of the pure rubber phase. This can be caused by the incorporation of DGEBA molecules into the rubber, forming a copolymer.(47) These relatively rigid polymeric segments, whether or not they form microdomains, can act as physical cross-links, thus increasing the cohesive strength and cavitation resistance of the rubber. Despite these differences in the behavior of the two types of rubber particles, the volume dilatometry results are quite similar, and the fracture toughness values are comparable. These observations suggest that the rubber type is not very important, as long as it is able to form a distinct dispersed phase.

#### 6.4 BPA-Modified System

The BPA-modified system forms very small ( $.1-.6 \mu$ ) rubber particles at rubber contents up to 10 phr. At 15 phr large rubber particles with epoxy sub-inclusions are found. The SEN-3PB fracture surface micrographs of the 5,10, and 15 phr materials are shown in Figure 6.11 and 6.12a,c. These were all taken from the stress-whitened region. At 5 and 10 phr, except for the much smaller size, the voids are very similar in appearance to those of the 828-8 system. A very similar type of rubber cavitation and failure process is thus indicated. At 15 phr, the large particles are often within one diameter of each other; furthermore, very small (approximately  $.1 \mu$ ) particles populate the interstitial space between the large particles. The particles give no apparent indications of interaction. Comparison of higher magnification

micrographs from the stress-whitened and the fast fracture regions (Figure 6.12) reveal the now familiar difference in the depth of the voids. The sub-micron voids in both micrographs do not appear to be smeared out or otherwise show signs of having enhanced plastic flow on this scale. The source of the enhanced toughness of this system may lie in the higher ductility on a much grosser scale. SEM micrographs of the stress-whitened region at low magnification of the three material systems, in decreasing order of toughness, i.e., 828-BPA(24)-8(15), 828-8(20) and 828-15(20), are shown in Figure 6.13. (Note the differences in magnification.) It is evident that a significantly larger amount of plastic flow has taken place on the fracture surface of the BPA-modified system. In retrospect, this seems consistent with the lower tensile yield stress and the higher ductility of this system. It is tempting to attribute the higher ductility to the larger rubber volume fraction(10), because of inclusions, or to the bimodal rubber particle size distribution (9). But it appears that matrix deformation and flow behavior must be considered, among other things, as exerting stronger influence. This will be considered in the final section.

#### 6.5 Back-Scattered Electron Analysis

Observations of the fracture surface SEM of the 828-8 system can easily lead one to the conclusion that the cavities are what remain after the rubber particles have somehow been ejected from the fracture surface. To determine whether the cavities are rubber-lined or empty, the fractured specimens were stained with  $\text{OsO}_4$ . Since  $\text{OsO}_4$  preferentially adds to the unsaturated rubber, a technique that can detect the areal distribution of Os would locate the rubber. The back-scattered electron analysis measures the extent to which electrons are elastically scattered from the surface. Since Os has a

significantly larger scattering cross section than organic polymers, it can be readily detected by the higher intensity of back-scattered electrons. In Figure 6.14 are micrographs of fracture surfaces of 828-BPA(24)-8(15), 828-8(10), and 828-15(10). The Os stained areas appear light in these micrographs. The internal structure of the rubber particles in the BPA-modified system is clearly discernible. The sub-micron voids that populate the interstitial space between the large rubber particles also appear to be lined with rubber. The similarity between Figure 6.12c and Figure 6.14a is striking. This micrograph unambiguously demonstrates the efficacy of the technique. The voids in the 828-8 and 828-15 systems are likewise lined with rubber. Some sub-surface particles are also faintly discernible in these micrographs as diffuse light spots. The micrographs conclusively prove that the voids have formed from the cavitation and fracture of the rubber particles. A detailed discussion of the back-scattered electron analysis technique can be found in Reference(48).

## 6.6 Low Temperature Fracture

The low temperature tensile dilatation data of the 828-15 system exhibit the most dramatic volume strain behavior found in these studies. The succinct features of the data in Figure 5.7 are recalled here. The volume strain rate is initially constant. Then, at some critical strain, which increases with rubber content, the volume strain rate suddenly increases. Finally, and just as suddenly, the volume strain rate again decreases, but to a value higher than the initial volume strain rate. The final volume strain rate is higher than the initial rate by an amount predicted by assuming that the "Poisson's ratio" of the material is reduced by a factor equal to the volume fraction of the epoxy matrix. This assumption is in fact the rule of mixture. For a matrix of Poisson's ratio  $\nu_1$  and volume fraction  $\theta_1$ , and a filler of Poisson's

ratio  $\nu_2$  and volume fraction  $\theta_2$ , the rule of mixture predicts the Poisson's ratio of the composite,  $\nu_c$ , to be:

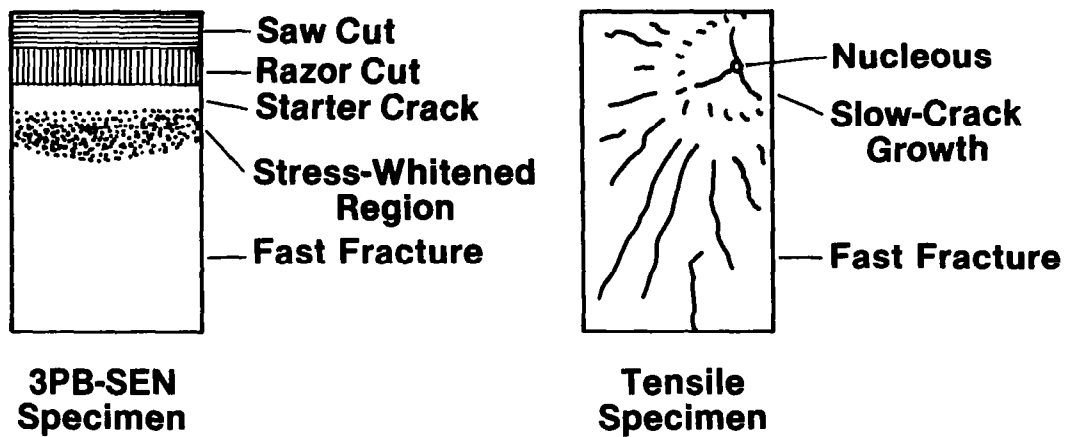
$$\nu_c = \theta_1 \nu_1 + \theta_2 \nu_2 \quad (6.1)$$

Equation 6.1 almost certainly overestimates the effect of spherical filler particles because it is a parallel model. If, in this case, it is assumed that the Poisson's ratio of the voids is zero, then  $\nu_c = \theta_1 \nu_1$ . This situation is depicted in Figure 6.15. The fact that this equation predicts so well the behavior in Figure 6.15 is, however, perhaps not entirely fortuitous. Figure 6.16, which shows the fracture surfaces in tensile specimens of 828-15(20) and 828-15(30), provides some clues. The voids, which in all cases examined in previous sections are hemispheres, are now all shallow disc-shaped. The cup-and-cone or cup-and-cup rubber fractures previously found are seen only rarely here. It should be emphasized here that these fracture surface features are dissimilar to those found in the stress-whitened areas of SEN-3PB specimens at room temperature. The fractures appear to have initiated from the interior of the rubber particles, then cut across the equatorial planes. This step in the deformation process would correspond to the rapidly rising volume strain portion. It is well known that rubber can fracture at very low strains when a large hydrostatic tension exists(49). This hydrostatic tension can arise from a combination of differential thermal shrinkage and mismatch in the Poisson's ratio. The opening of the equatorial cracks would relieve the lateral stress due to the differential Poisson's ratio, and at the same time cause the composite to act temporarily like one with a low Poisson's ratio. When the equatorial cracks reach the rubber-matrix interface, they are abruptly stopped, and the composite now behaves like a solid filled with disc-shaped voids. The

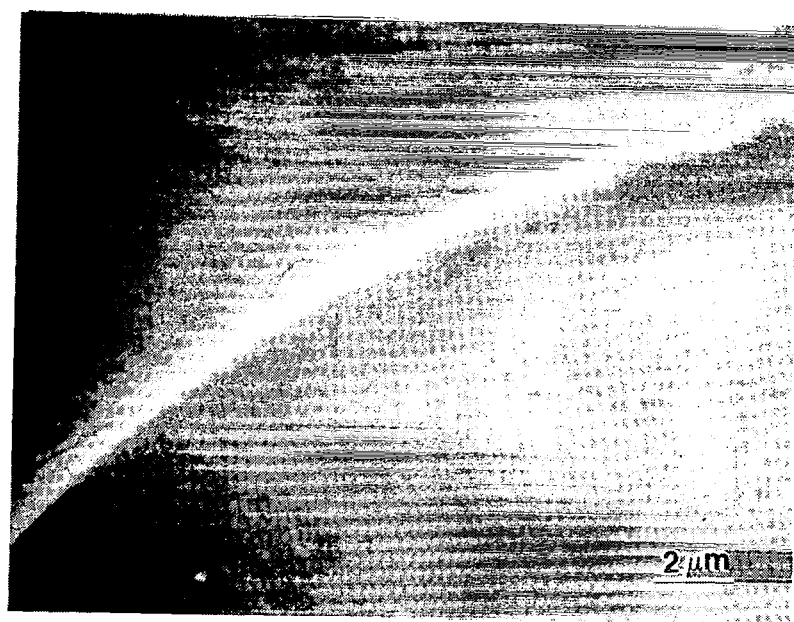
volume strain behavior of this composite should resemble that of a solid filled with the same volume fraction of crazes(50), which obeys the rule of mixtures (Eq. 6.1). The abrupt change in the slope of the stress-strain curves is consistent with the above model.

It can be argued that, since the volume strain behavior discussed above is similar to that of a solid containing crazes, crazing may in fact be taking place in this deformation process. The evidence presented in this section certainly does not preclude it. The central question, however, is whether massive crazing is a major toughening mechanism in room temperature fracture. The evidences presented thus far indicate the negative. As shown in the early parts of this section, only the tensile fracture surfaces at room temperature resemble closely those of the SEN-3PB specimens. Thus, the room temperature tensile dilatometry results also reflect qualitatively, if not quantitatively, the type of deformation mechanisms that are operative in fracture. The volume strain curves all indicate initial homogeneous deformation followed by some voiding and fracture of the rubber particles, and finally shear flow. These, then, appear to be the major toughening mechanisms.

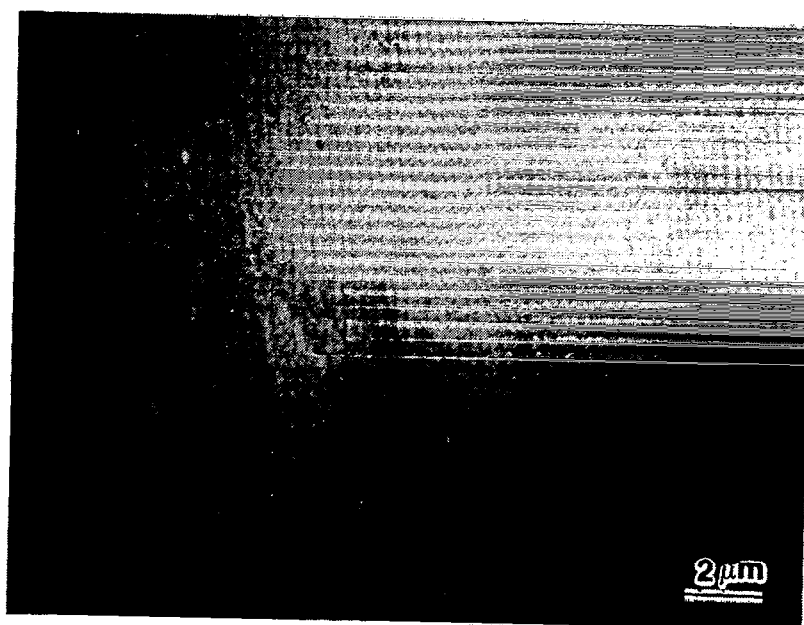
The validity of the above discussion should be tempered by the fact that surface deformation accounts for only a fraction of the total energy of most solids. Sub-surface deformation can dissipate significant amounts of energy. These deformations are studied in the next section.



#### 6.1 Schematic Representation of SEN-3PB and Tensile Fracture Surfaces of Rubber Modified Materials

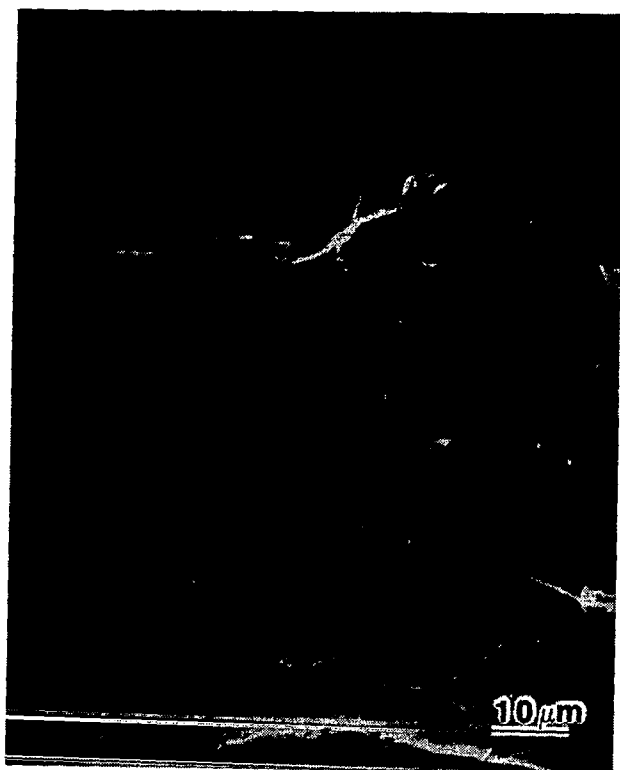


(a)



(b)

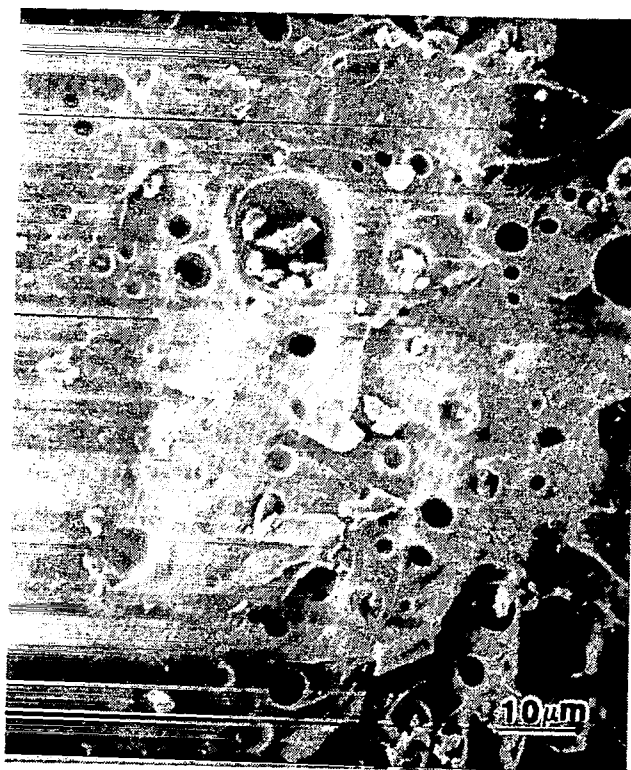
6.2 SEM of Fracture Surfaces of (a) Control Epon 828 and (b) 828-13(5) tested in SEN-3PB



(a)

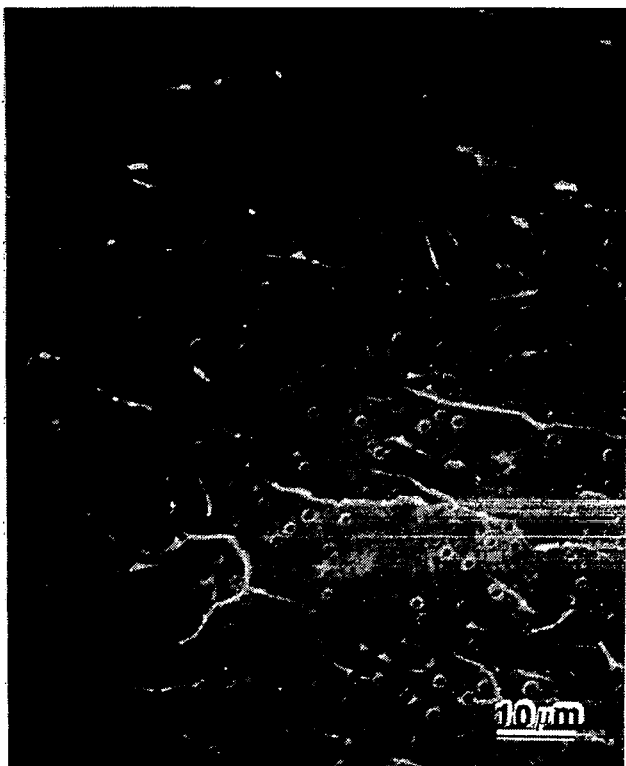


(b)



(c)

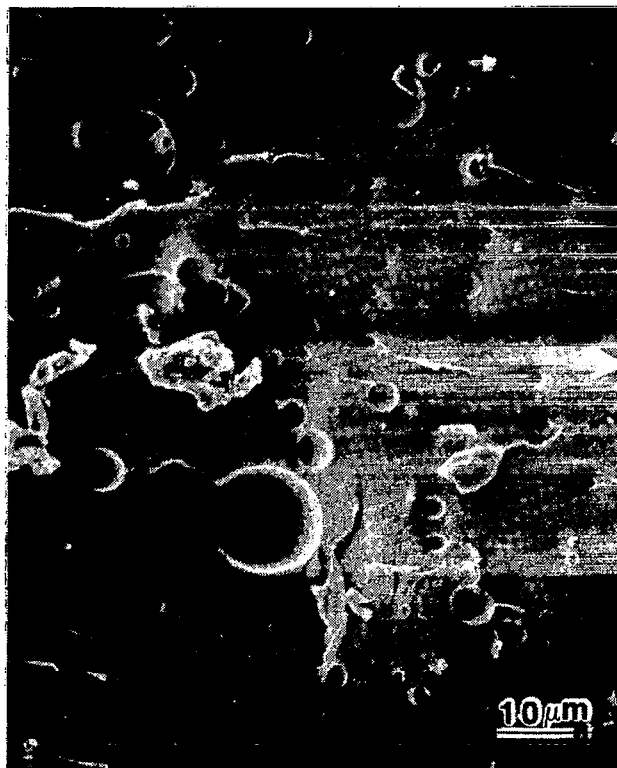
6.3 SEM from the Stress-Whitened Areas of the SEN-3PB Fracture Surface of (a) 828-8(5); (b) 828-BPA(24)-8(5); (c) 828-15(5)



(a)

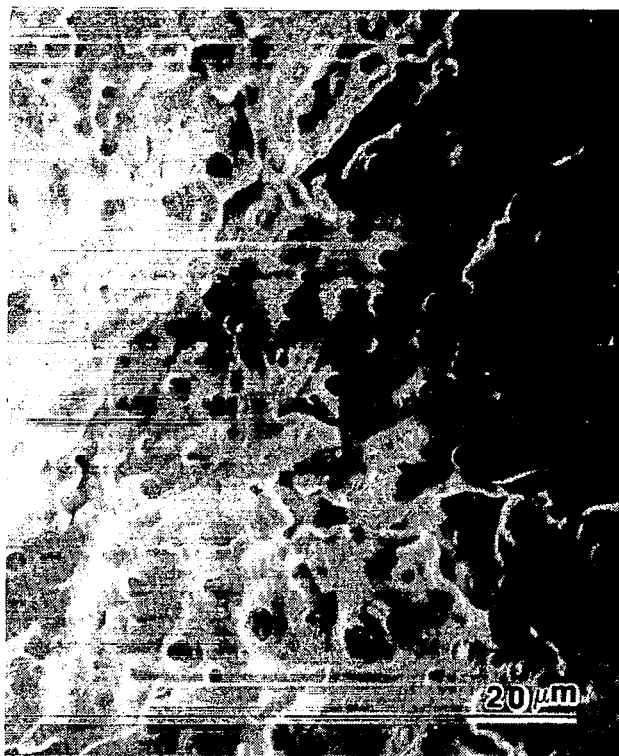


(b)

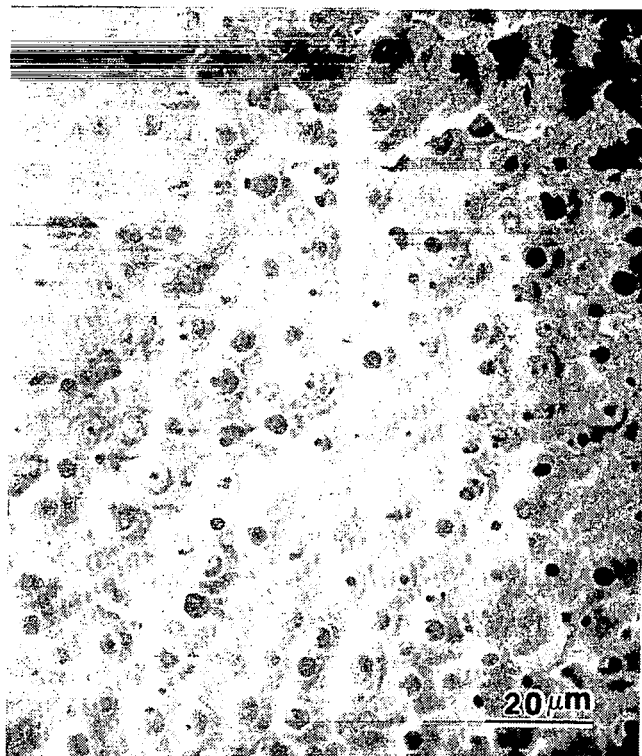


(c)

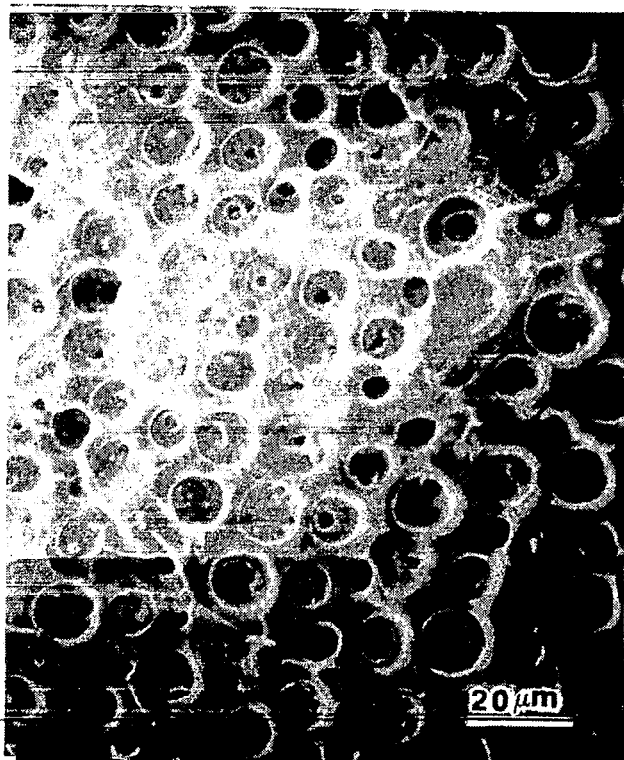
6.4 SEM from the Fast Fracture Areas of the SEN-3PB Fracture Surfaces  
of (a) 828-8(5); (b) 828-BPA(24)-8(5); (c) 828-15(5)



(a)



(b)



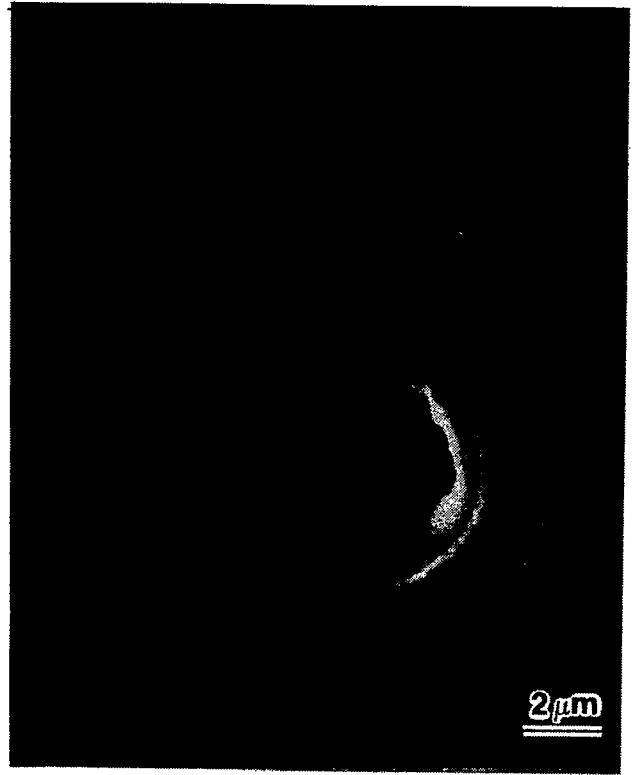
(c)

6.5 SEM From the Stress Whitened Areas of the SEN-3PB Fracture Surfaces  
of (a) 828-15(10); (b) 828-15(20); (c) 828-15(30)

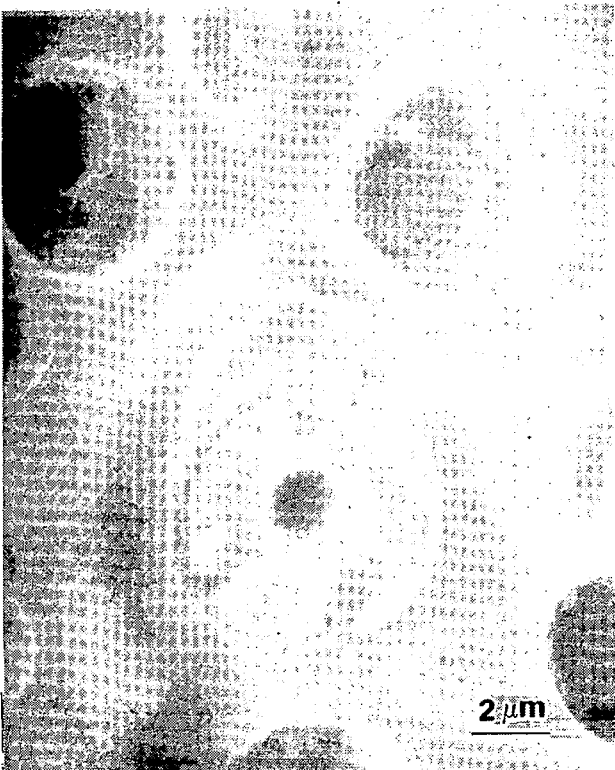
(a)



(b)



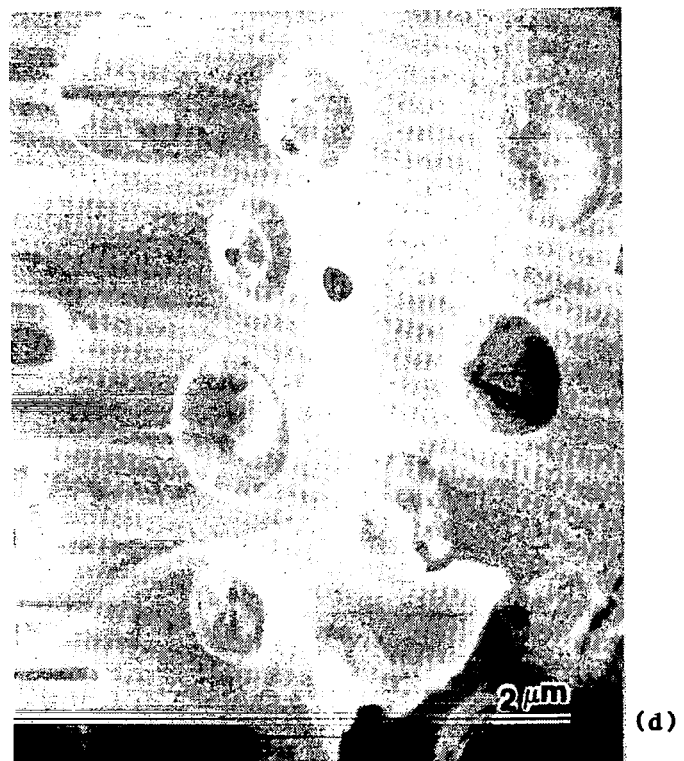
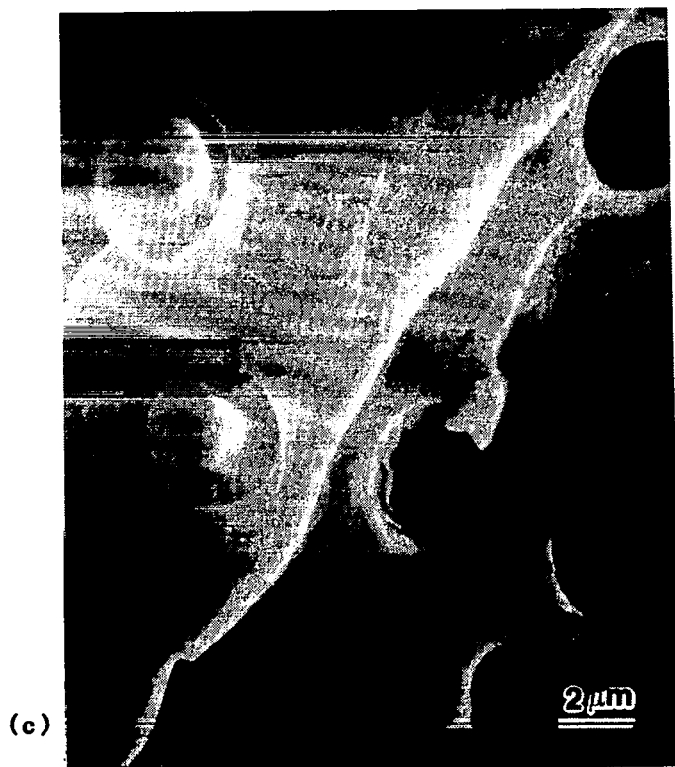
(c)



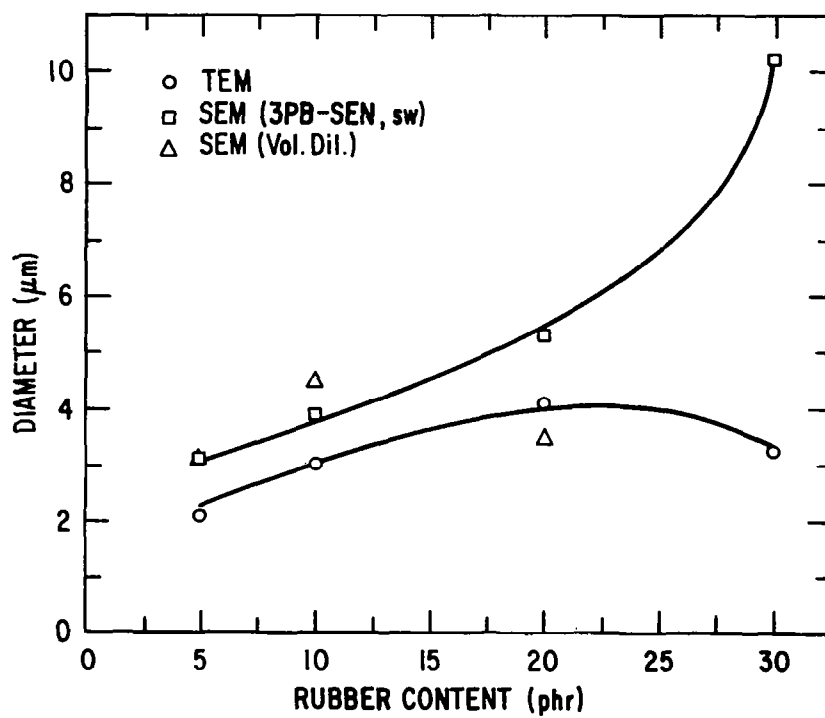
(d)



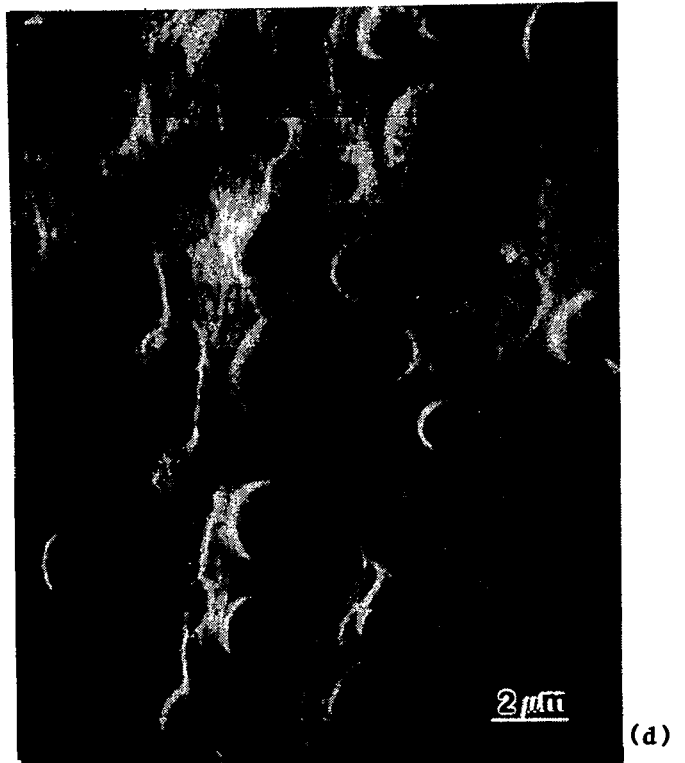
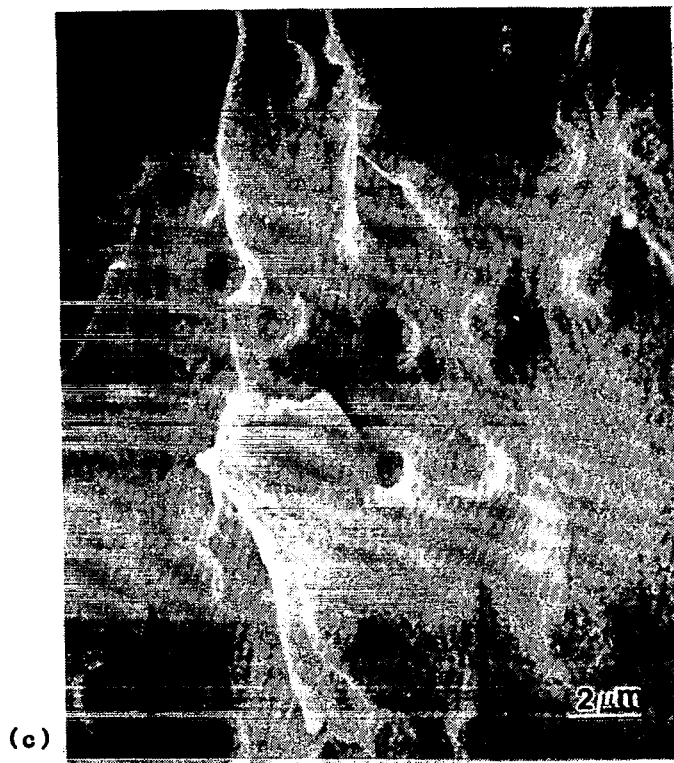
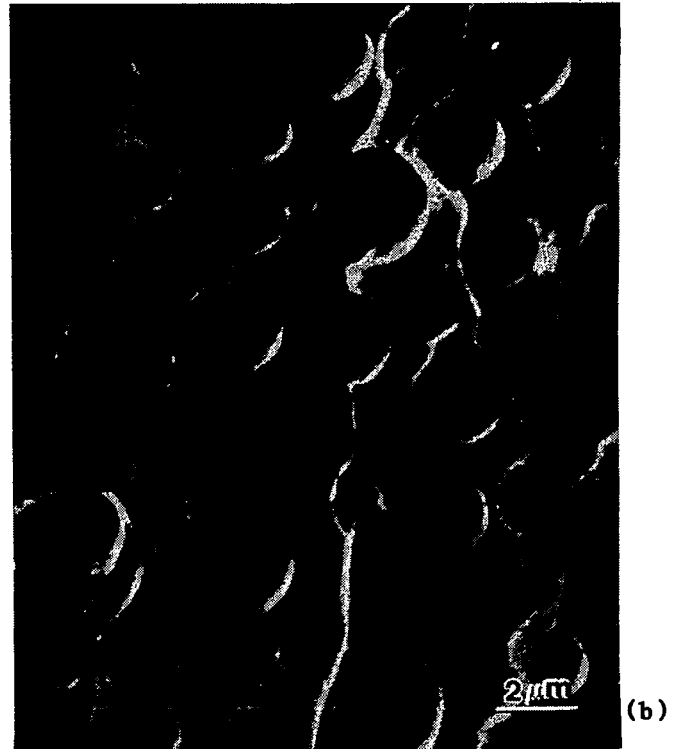
**6.6 Higher Magnification SEM From the Stress Whitened Areas of the 3PB-SEN Fracture Surfaces of (a) 828-15(5); (b) 828-15(10); (c) 828-15(20); (d) 828-15(30)**



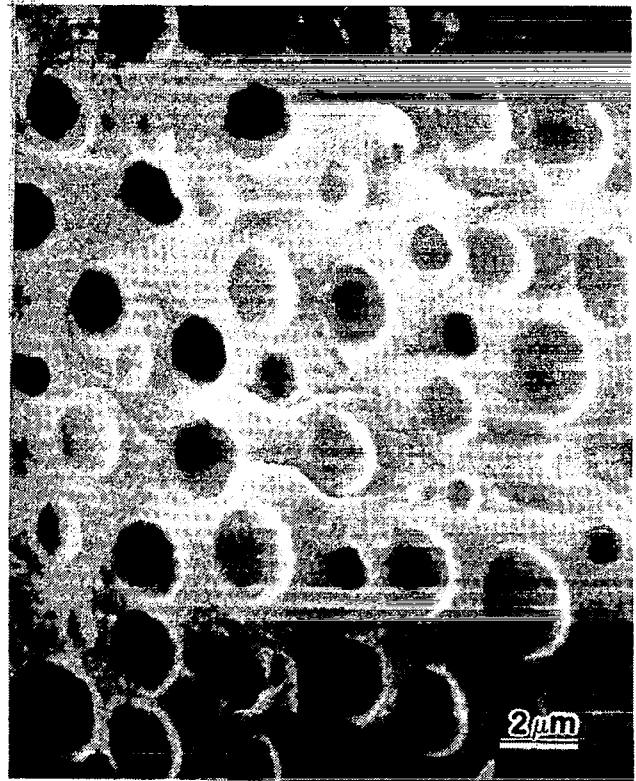
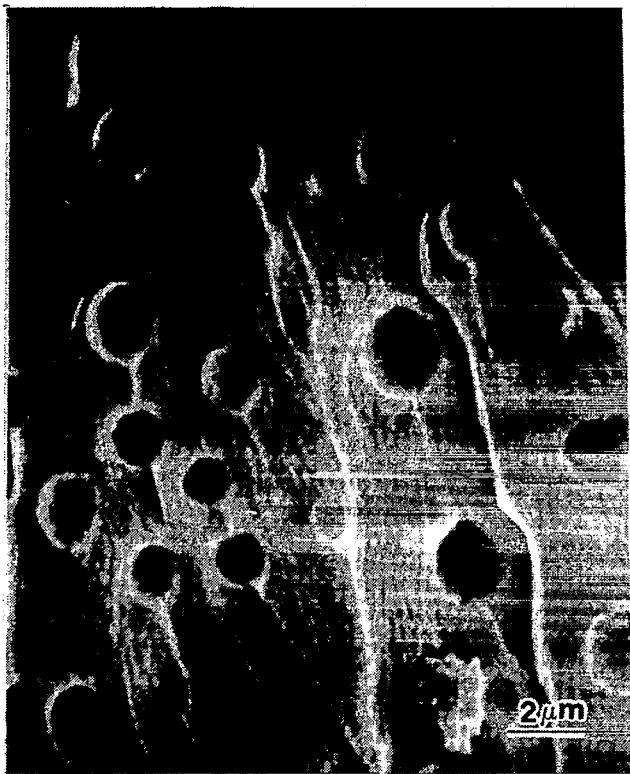
6.7 Higher Magnification SEM From the Tensile Fracture Surfaces of (a) 828-15(5); (b) 828-15(10); (c) 828-15(15); (d) 828-15(20)



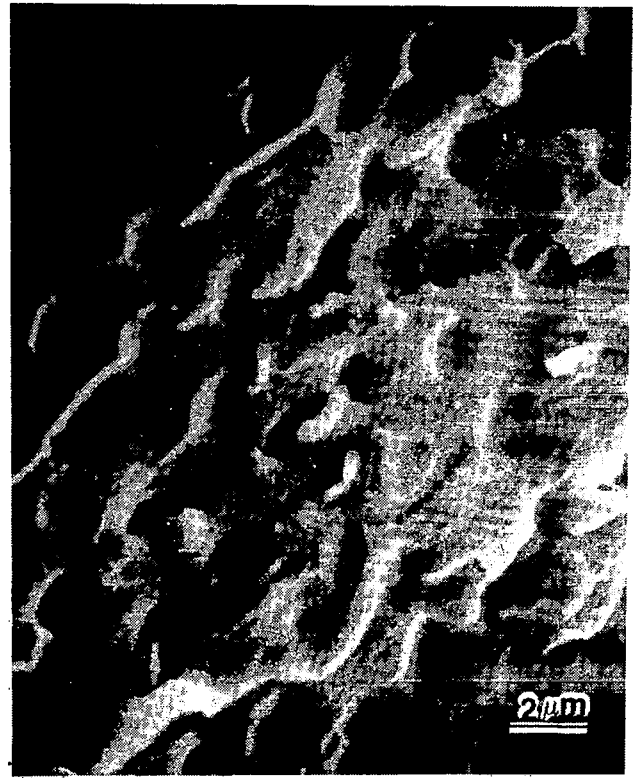
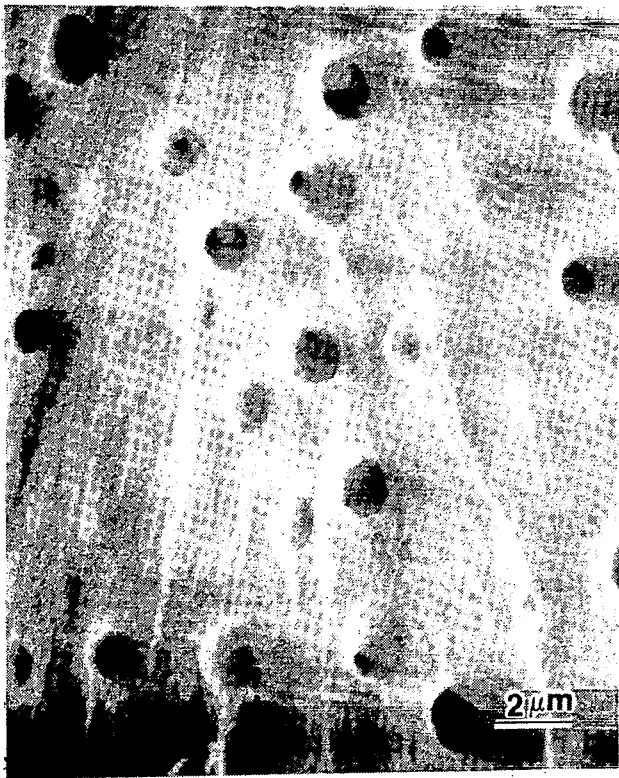
6.8 Plot of the Mean Diameters of Particles and Voids vs. Rubber Content



6.9 SEM of the Stress Whitened and Fast Fracture Areas of the SEN-3PB Fracture Surfaces of (a) 828-8(10); (b) 828-8(20)

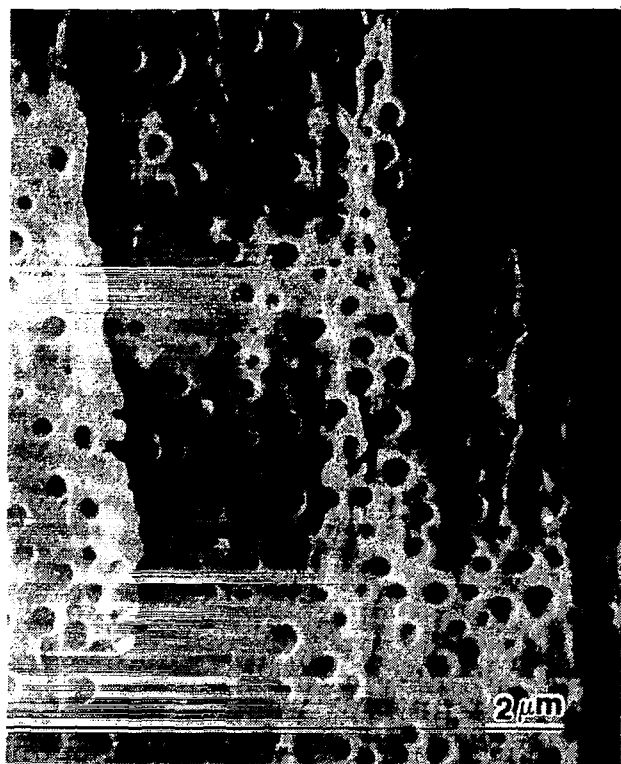
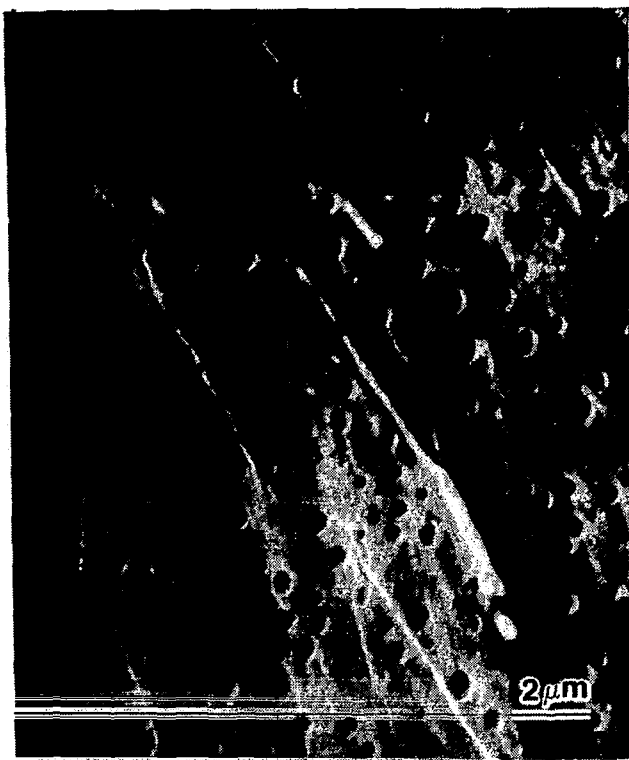


(a)

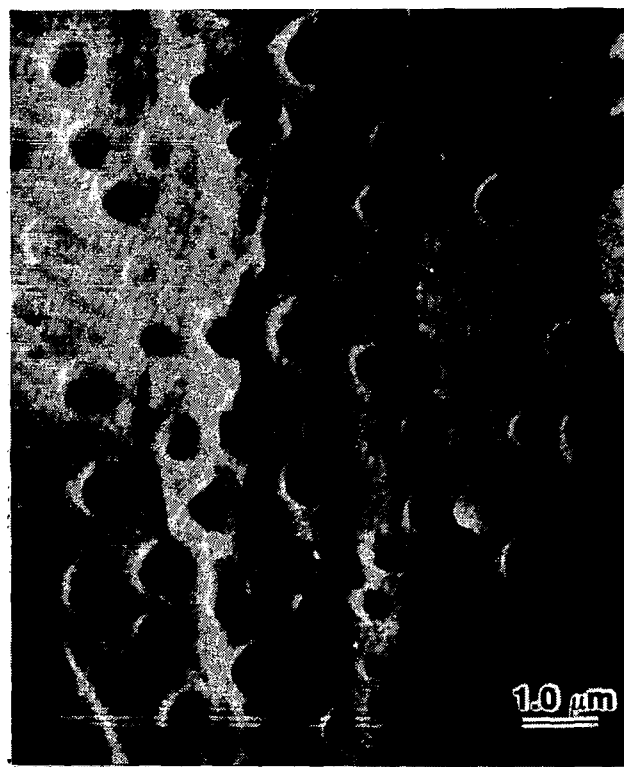


(b)

6.10 SEM of the Slow Crack Growth and Fast Crack Growth Regions of Tensile Fracture Surfaces of (a) 828-8(10); (b) 828-8(20)



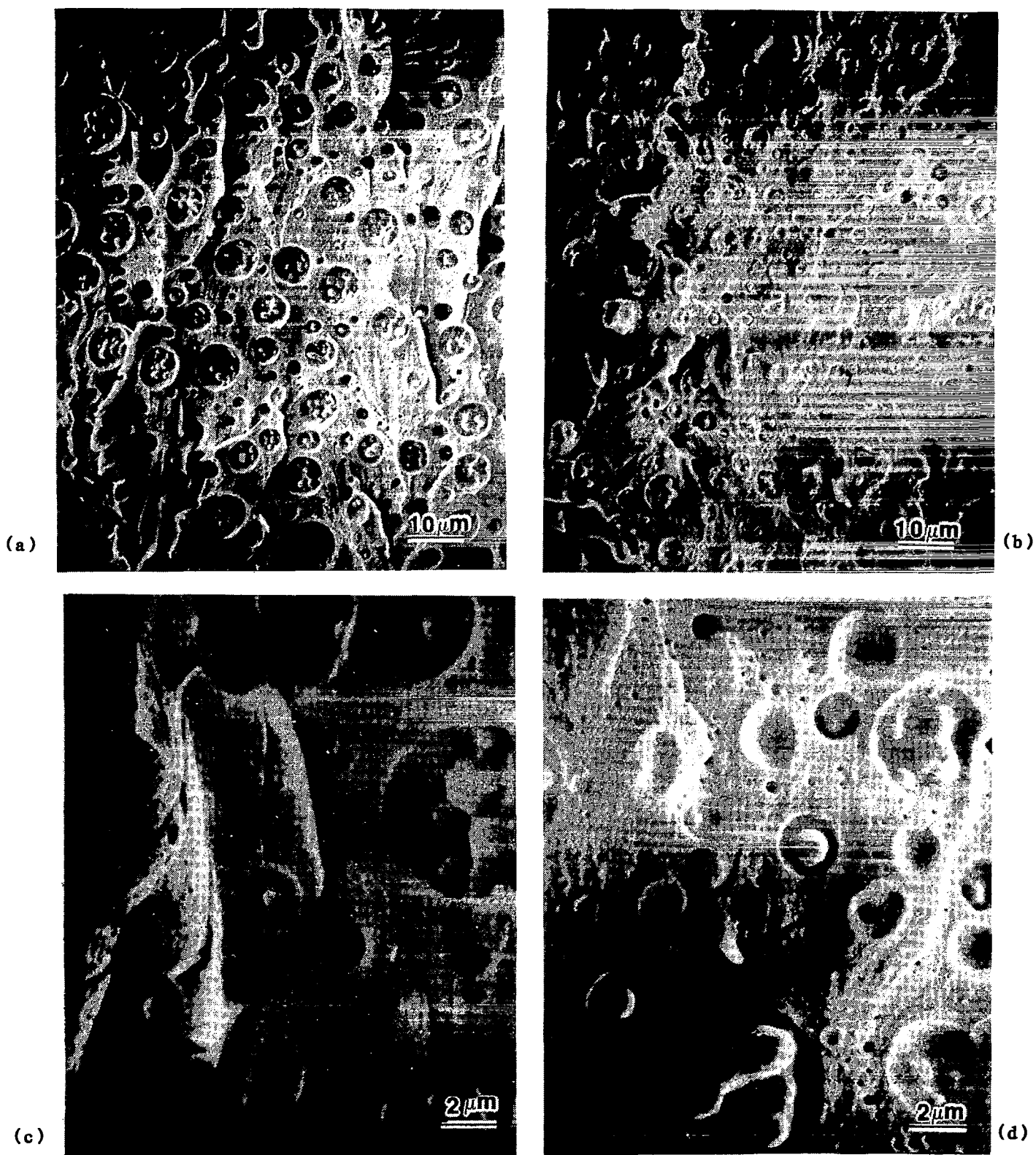
(a)



(b)

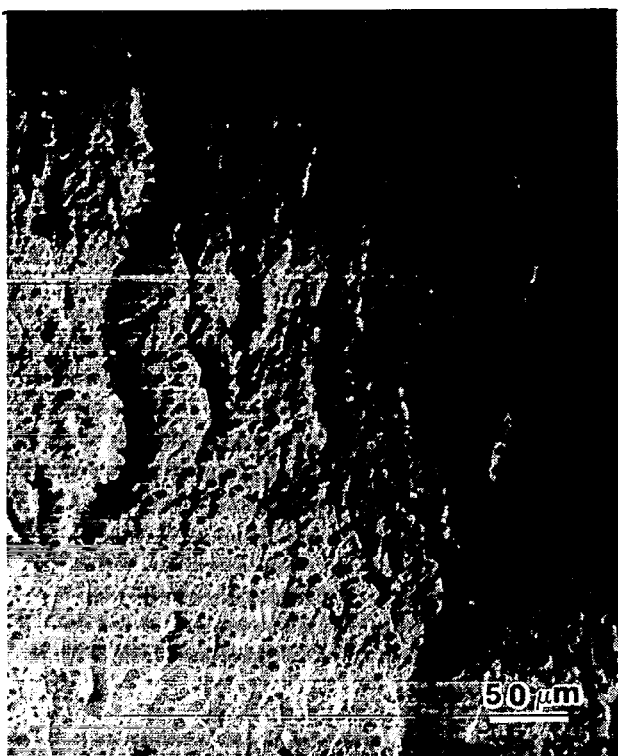
6.11 SEM of the Stress Whitened Region of the SEN-3PB Fracture Surfaces of

(a) 828-BPA(24)-8(5); (b) 828-BPA(24)-8(10)

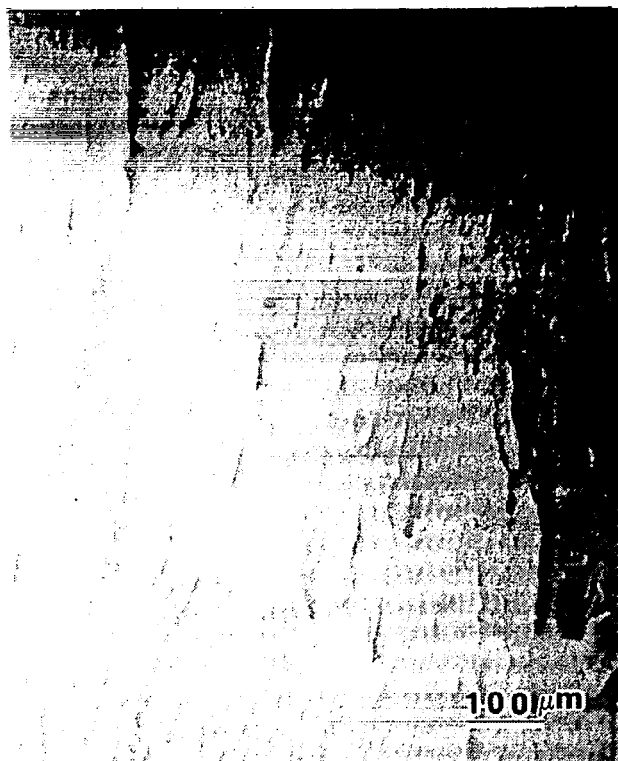


6.12 SEM of the Stress Whitened and Fast Fracture Regions of the SEN-3PB

Fracture Surfaces of 828-BPA(24)-8(15): (a),(c) Stress Whitened Region;  
 (b),(d) Fast Fracture



(a)

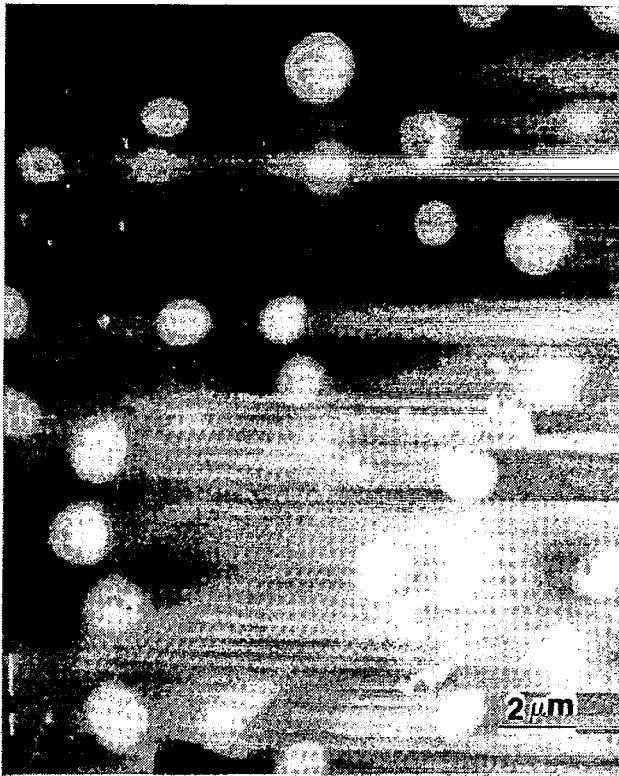


(b)

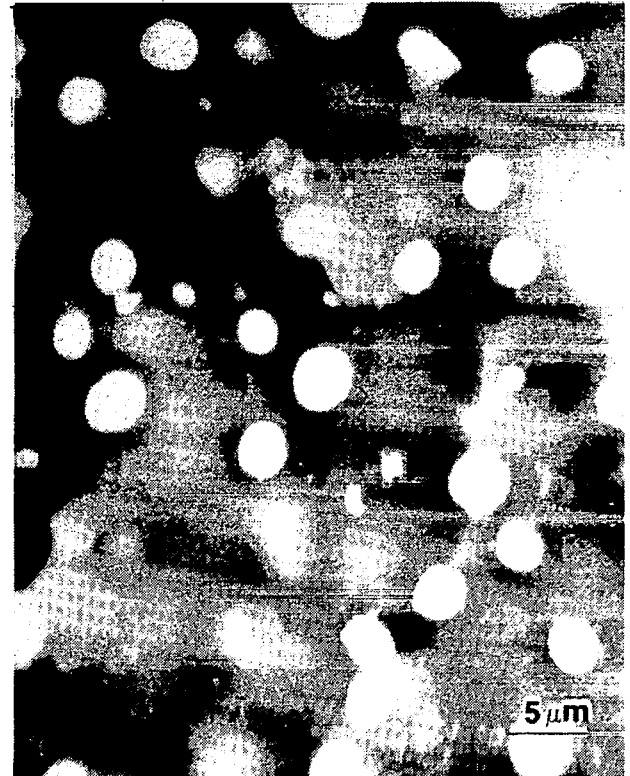


(c)

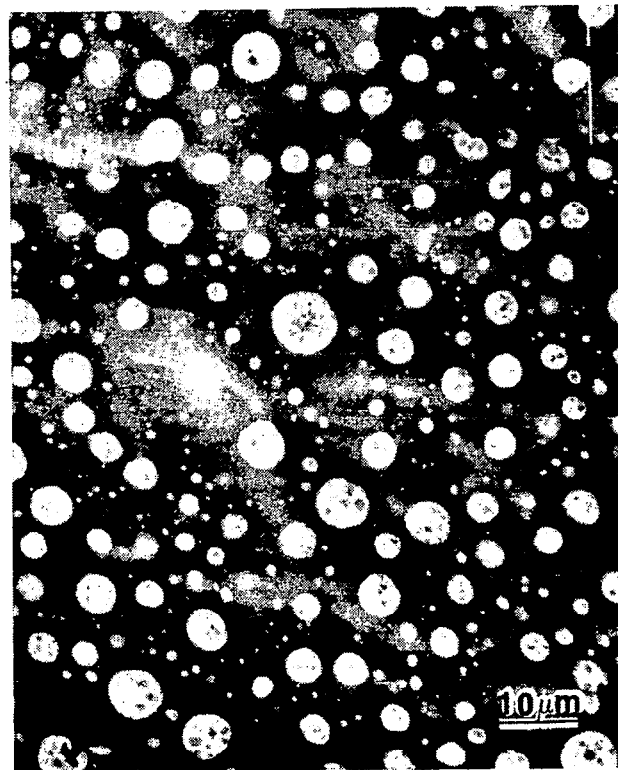
6.13 Low Magnification SEM of Stress Whitened Regions of the SEN-3PB Fracture Surface of (a) 828-BPA(24)-8(15); (b) 828-8(20); (c) 828-15(20)



(a)

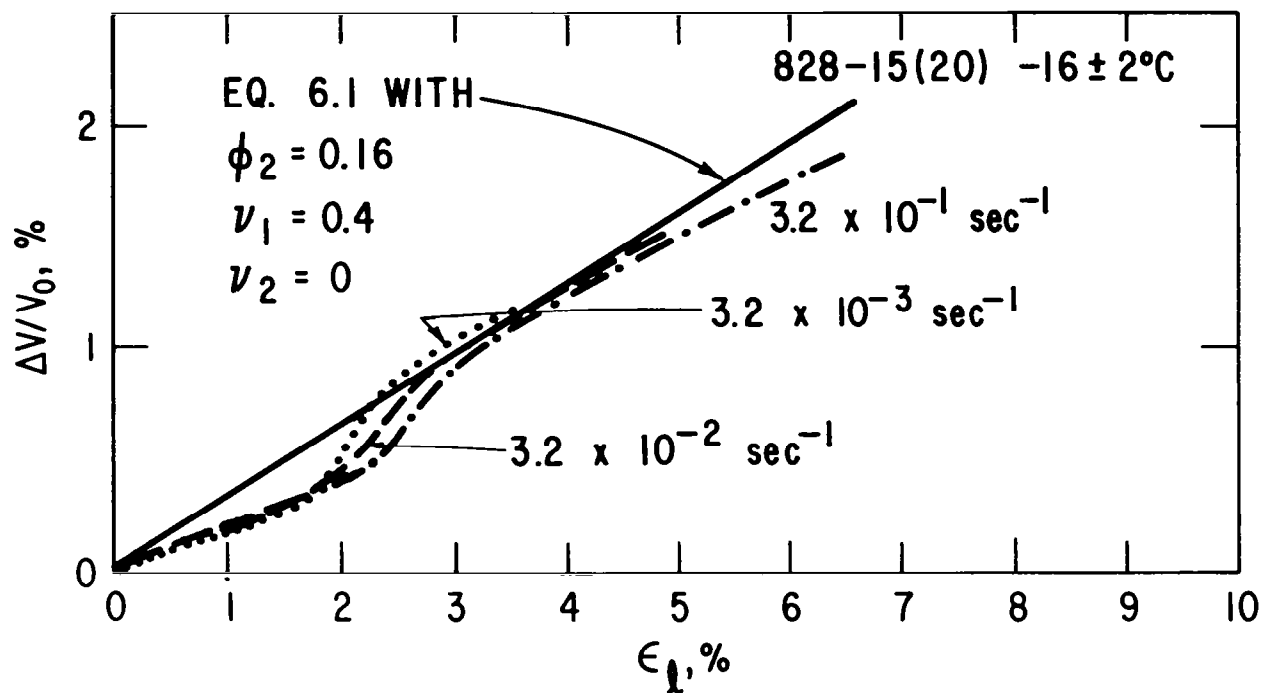


(b)



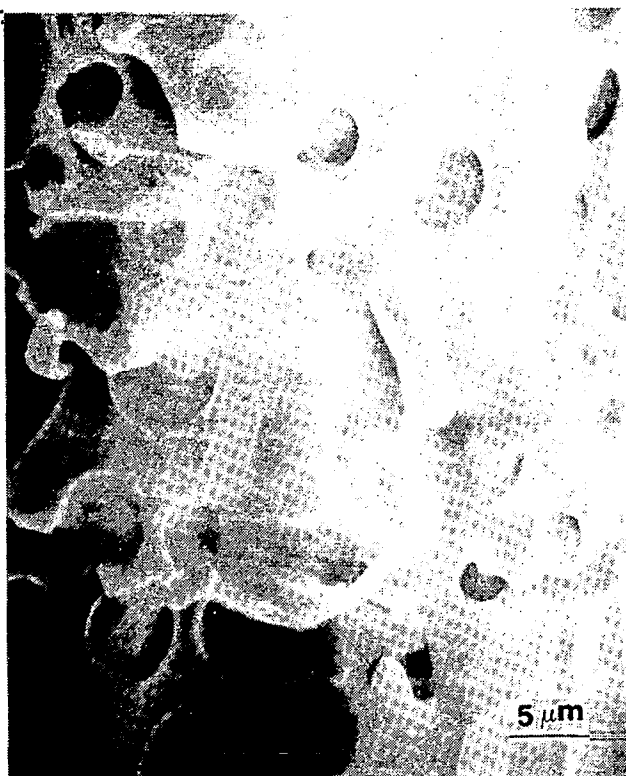
(c)

6.14 Back Scattered Electron SEM of SEN-3PB Fracture Surfaces of (a) 828-8(10); (b) 828-15(10); (c) 828-BPA(24)-8(15)

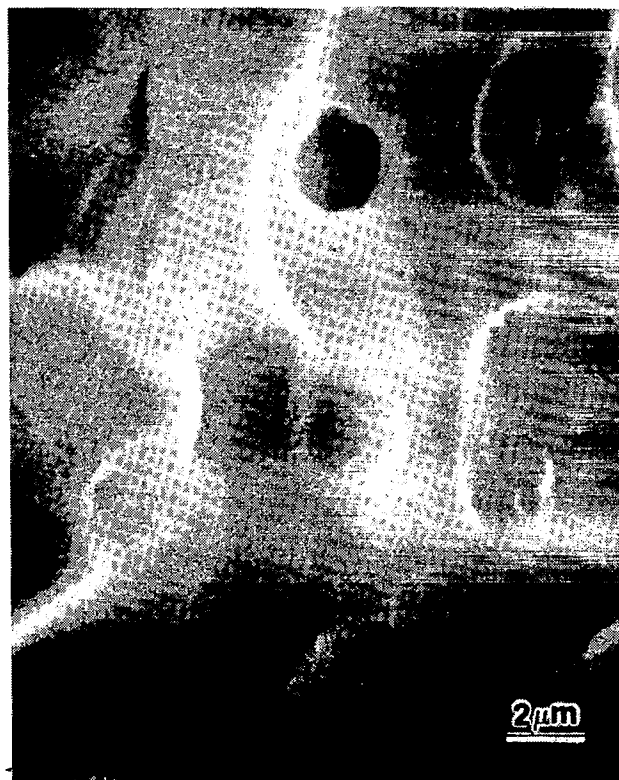
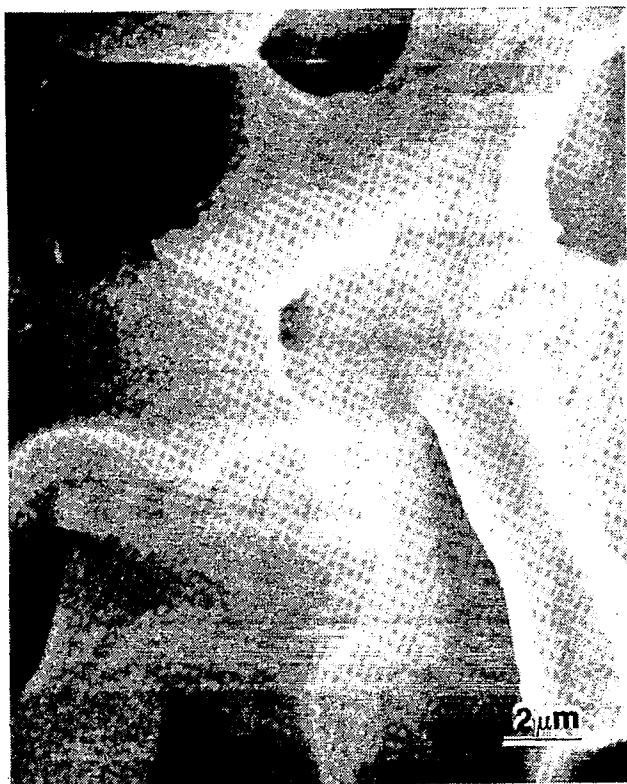


6.15 Equation 6.1 with  $\nu_1 = .40$ ,  $\phi_1 = .84$ ,  $\nu_2 = 0$ ,

$\phi_2 = .16$



(a)



(b)

6.16 SEM of Tensile Fractured ( $-16 \pm 2^\circ\text{C}$ ) Surfaces of (a)

828-15(20); (b) 828-15(30)

## 7. SUB-SURFACE DAMAGE

With few exceptions most solids do not fracture in the manner idealized by Griffith(51). The fracture surface morphologies investigated in the last section leave no doubt that sub-surface damage exists. In fact, since stress-whitening is visible on most of the fracture surfaces, a substantial damage layer in at least the  $\mu\text{m}$  range undoubtedly exists. The nature of the damage, however, cannot be unambiguously determined from SEM of surfaces. Remnants of broken craze fibrils are usually extremely difficult to view on the fracture surface. Shear bands do not usually produce sufficiently sharp surface topography. This section is devoted to investigations of subsurface damage by optical microscopy (OM), small angle X-ray scattering (SAXS), and transmission electron microscopy (TEM).

### 7.1 Optical Microscopy

OM is useful for observing deformations that induce birefringence. SEN-3PB fractured specimens are discussed here. In order to view damage below the surface, a thin section perpendicular to the fracture surface is obtained by metallographic techniques. The specimen is first embedded in clear epoxy. The two side surfaces of the specimen perpendicular to the fracture surface are gradually removed by metallographic polishing, until a thin slice from the central section of about  $25\ \mu\text{m}$  thickness remains. This thin section is then viewed in a Zeiss microscope with transmitted light with or without crossed polarizers. This technique is described in more detail in Reference (52). Figures 7.1 and 7.2 are OM micrographs from 828-8(20) and 828-BPA(24)-8(15), respectively. These micrographs show a strongly birefringent damage zone that is from 100 to  $150\ \mu\text{m}$  in thickness. Figure 7.2 shows a fracture surface that

contains many steps, indicating that the crack has traveled along different planes. Figures 7.3 and 7.4 are higher magnification micrographs taken from the same two specimens. The fracture surface in Figure 7.4 is at the upper right hand corner. In these micrographs, thick bands of highly birefringent material are seen to meander from particle to particle. These bands are as a whole not parallel to the plane of the fracture. Farther away from the fracture surface, where there are fewer bands, it is easier to see that these birefringent bands are distinctly inclined with respect to the fracture surface. Note that in Figure 7.3 the crack has travelled from right to left; the bands in the lower portion of the micrograph are predominately aligned along a direction from the lower left hand corner to the center of the right hand edge of the micrograph. An important feature to note is that few bands are observed in the lower portion of the micrograph with the opposite inclination, i.e., along a direction from the lower right hand corner to the center of the left edge of the micrograph. The inclination of these bands is characteristic of shear bands. Again in Figure 7.3 near the fracture surface, the rubber particles appear to be significantly larger than those outside the plastic zone. The limited resolution of OM makes it impossible to ascertain the exact size of these enlarged particles, nor is it possible to determine if cavitation has occurred. But cavitation or debonding of the particles must have occurred, judging by the intense stress whitening.

Some of the particles in Figure 7.4 are quite large, and they contain sub-inclusions. This feature has already been observed earlier. The particles near the fracture surface are slightly elongated; they scatter light whenever the birefringent bands pass through them. The scattering may be due to internal voiding. Again the limited resolution of OM does not allow for

precise determination of these features. Here, too, the intense stress whitening indicates that voiding or debonding must have occurred. Near the fracture surface (upper right hand corner), the bands coalesce so that they form patches of birefringence. In the black and white photographs shown, they have a mottled appearance.

Figure 7.5(a-d) are transmission optical micrographs of the subsurface damage beneath the fracture surface of typical 828-15(10) SEN test specimens and volume dilation specimens. The lower rubber content and large rubber particles bring out certain features observed in the higher rubber content systems. Figure 7.5a is a bright field micrograph, of the subsurface damage which exists under the stress whitened region of a fractured SEN specimen. Internally voided rubber particles appear black due to the scattering of visible light by the voids. This same section viewed between crossed polarizers is shown in Figure 7.5b. The highly birefringent bands radiating from the voided rubber particles are due to the sheared material. These micrographs are further evidence for the proposed toughening mechanism of internal voiding and enhanced shear band formation. Figures 7.5c and 7.5d are transmission optical micrographs of the subsurface damage beneath the fracture surface of a volume dilation specimen. Again, the same two types of subsurface damage are observed: internal voiding and shear band formation. These results support the assumption that the deformations measured by tensile dilatometry are similar to the deformations occurring at the crack tip.

To sum up the OM observations, the formation of thick plastic zones appear to be associated with the presence of a high volume fraction of rubber particles. Close proximity of the rubber particles to each other appears to facilitate the formation of birefringent bands between the particles.

Particle-particle interaction is thus indicated. These bands have none of the characteristics conventionally associated with crazes in thermoplastics. They have the characteristics of shear bands. The shear bands form in planes inclined with respect to the fracture surface. The inclination of these planes is similar to what is predicted by slow crack growth in linear elastic solids. The bands always pass through particles that scatter light, but not all particles that scatter light have bands emanating from them. The light scattering property of the particles is most likely caused by internal cavitation. Thus, the deformation process is one of cavitation of the particles followed by shear bands that form between the particles.

The deformation process can be hypothesized from the above observations. It appears that the sharp starter crack is first blunted by an initial plastic zone. The sharp crack is now replaced by one with a much larger effective crack tip radius. A larger plastic zone grows as the stress is increased. When plastic constraint in the center of this zone develops, a triaxial tensile stress is generated, resulting eventually in cohesive failure along a plane perpendicular to the major principal tensile stress. It seems plausible that the initial plastic zone that blunts the starter crack is a zone of voided material. But as soon as the shear bands form they become the dominant mode of deformation until crack propagation resumes. According to this line of reasoning, then, the principal energy absorbing mechanism appears to be shear banding, which is made possible by the void blunting of the crack.

## 7.2 SAXS

In spite of the fact that none of the experimental observations made thus far positively demonstrate the existence of crazing in these materials, the

possibility that some form of crazing or precursors to crazing exists cannot be entirely excluded. Since crazes contain many voids, those density fluctuations in the range of several nm to several hundred nm can be detected by SAXS. Measurements have been made on several fractured tensile specimens by Dr. LeGrand of this Laboratory. The detailed results will be published in a future report. Some of the observations are briefly presented here.

The measurements were made on a SAXS apparatus which has a detecting system consisting of a linear array of 1024 detectors. The specimen was placed in the X-ray beam collimated by a horizontal slit. The detector array, which was also horizontal, was placed behind the specimen. The specimen was displaced vertically for scanning. The scattered radiation was detected and counted by a multi-channel analyzer. The large amount of data accumulated was transmitted to a computer. The areal scattering intensity was reconstructed by the computer. Computer graphics techniques were then employed to enhance the intensity scale and assign different colors to correspond to different intensities. The color pattern was displayed on a color video monitor.

A black and white photograph of such a display is shown in Figure 7.6a. The specimen was a fractured 828-8(10) tensile bar whose two halves had been reattached using adhesive tape. The fracture plane is the dark line (red in the color display) that runs horizontally across the photograph. This dark color represents the highest scattering intensity. Note that this dark line has a substantial width over much of its length, indicating that a layer with a high concentration of scattering centers exists below the fracture surface. The dark line is surrounded by a light-colored (yellow) zone, which represents medium scattering intensity. Farther away from the fracture surface this light-colored zone is in turn replaced by a dark-colored (green) zone, which

represents still lower, essentially background-type, scattering intensity. This photograph demonstrates that scattering centers extend far below the fracture surface. A photograph of a magnified portion of the above display is shown in Figure 7.6b. In this photograph a dark, (high intensity) line is seen running parallel to but below the fracture surface near the left edge. The width of this line is 25  $\mu\text{m}$ , which is one side of a detector areal element. Thus, there appears to be a high concentration of scattering centers within this horizontal 25  $\mu\text{m}$  band.

It is tempting to equate these horizontal concentrations of scattering centers to crazing. Voids in the rubber particles, if they exist this far below the fracture surface, are most likely too large ( $> 1\mu\text{m}$ ) to be seen by SAXS. Scattering off small rubber particles merely forms the background. The observed scattering pattern is due to scattering centers too small in size to be observed by the micrographic techniques presented thus far. The scattering centers are probably areas of lower density caused by the combination of fluctuations in cross-link density and rubber particles acting as stress concentrators. One thing is quite certain, though. The scattering centers have not aggregated closely enough together to form horizontal bands sufficiently large to be behaving mechanically like crazes. If crazing were the case the volume dilatation curves would have exhibited typical crazing behavior. Since crazes absorb most of their energy by the growth and extension of the craze fibrils, it seems safe to conclude that, despite the existence of what appears to be craze precursors, this mode of microdeformation does not contribute significantly to toughening.

### 7.3 TEM

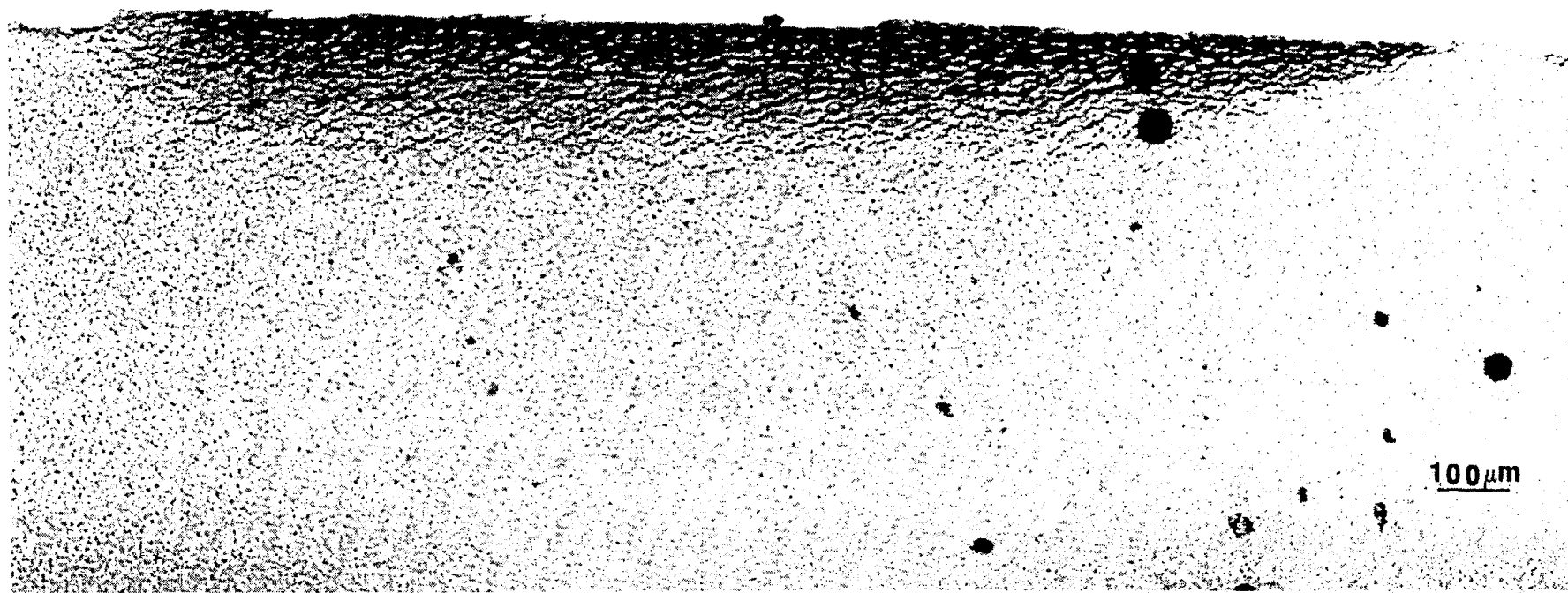
Two crucial questions brought out by the OM and the SAXS results need to be answered. The OM results on the 828-15 and the 828-BPA-8 systems indicate that the rubber particles below the fracture surface may not have cavitated. In the case of the small particles in the 828-8 system, the micrographs have insufficient resolution to provide useful information. The SAXS results indicate the existence of low density scattering centers in the size range from several nm to several hundred nm. It would be useful to observe these scattering centers and determine how they aggregate in the matrix. It was proposed that the use of TEM might be able to provide some answers to these problems.

The specimen preparation technique is the same as discussed before in 3.2, except that the ultra-thin sections were taken from the same planes as the OM specimens, i.e., perpendicular to the fracture surface of the SEN-3PB specimens. Care was taken to microtome the thin-sections in a direction perpendicular or at  $60^\circ$  to the fracture surface. A typical TEM micrograph is shown in Figure 7.7. With few exceptions, the rubber particles are torn easily from the matrix if they are very near the fracture surface. But the  $\text{OsO}_4$  stained rubber particles far away from the surface are cut without any tearing. This indicates that the particles near the surface have much lower mechanical integrity. It can be surmised that they have undergone cavitation or debonding. The matrix exhibits no crazing or voiding of any kind. It is possible that the technique used in sample preparation is not sufficiently refined to allow extremely small voids or crazes to be detected. What is more likely, though, is that the density fluctuation is not sufficiently high to be detected by the TEM technique.

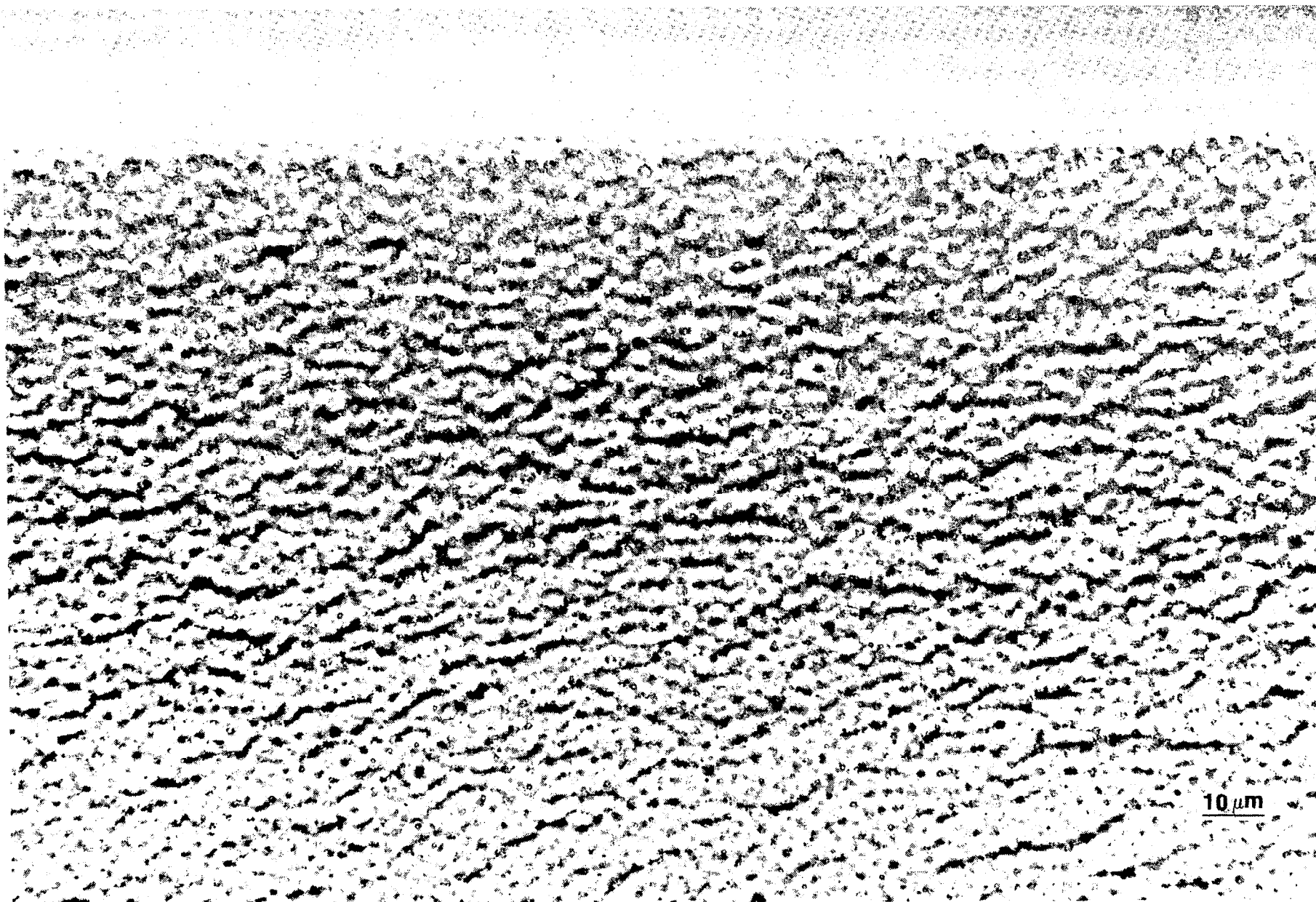
A high-magnification micrograph showing a subsurface damage region. The image is divided into two main horizontal sections. The upper section is a bright, granular layer, likely the stress-whitened region. The lower section is a darker, more uniform area. A sharp, dark, curved line separates the two sections, indicating a boundary or crack. The overall texture is grainy and speckled.

100  $\mu$ m

7.1 OM of Subsurface Damage in 3PB-SEN Stress Whitened Region of 828-8(20)

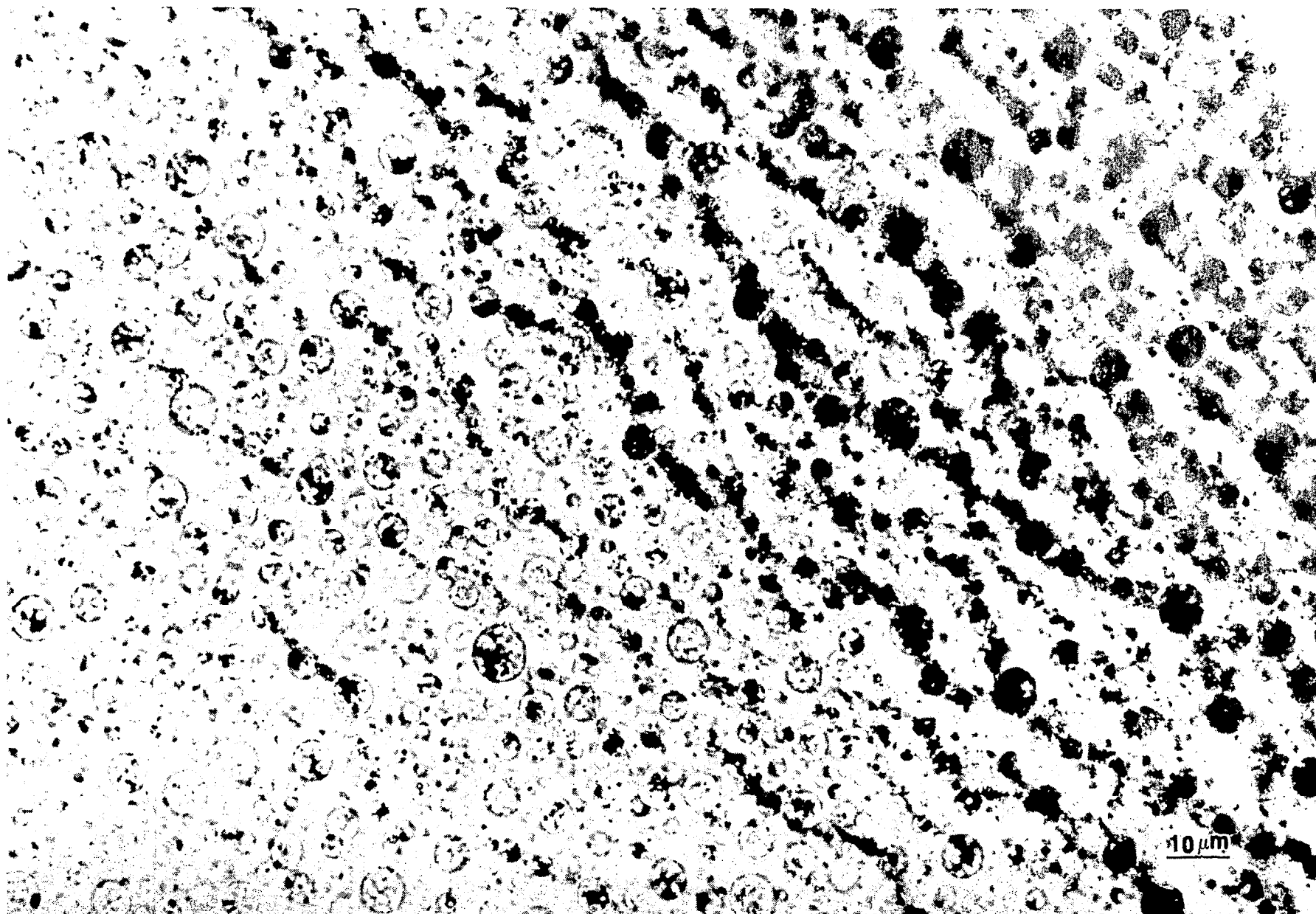


7.2 OM of Subsurface Damage in the SEN-3PB Stress Whitened Region of  
828-BPA(24)-8(15)



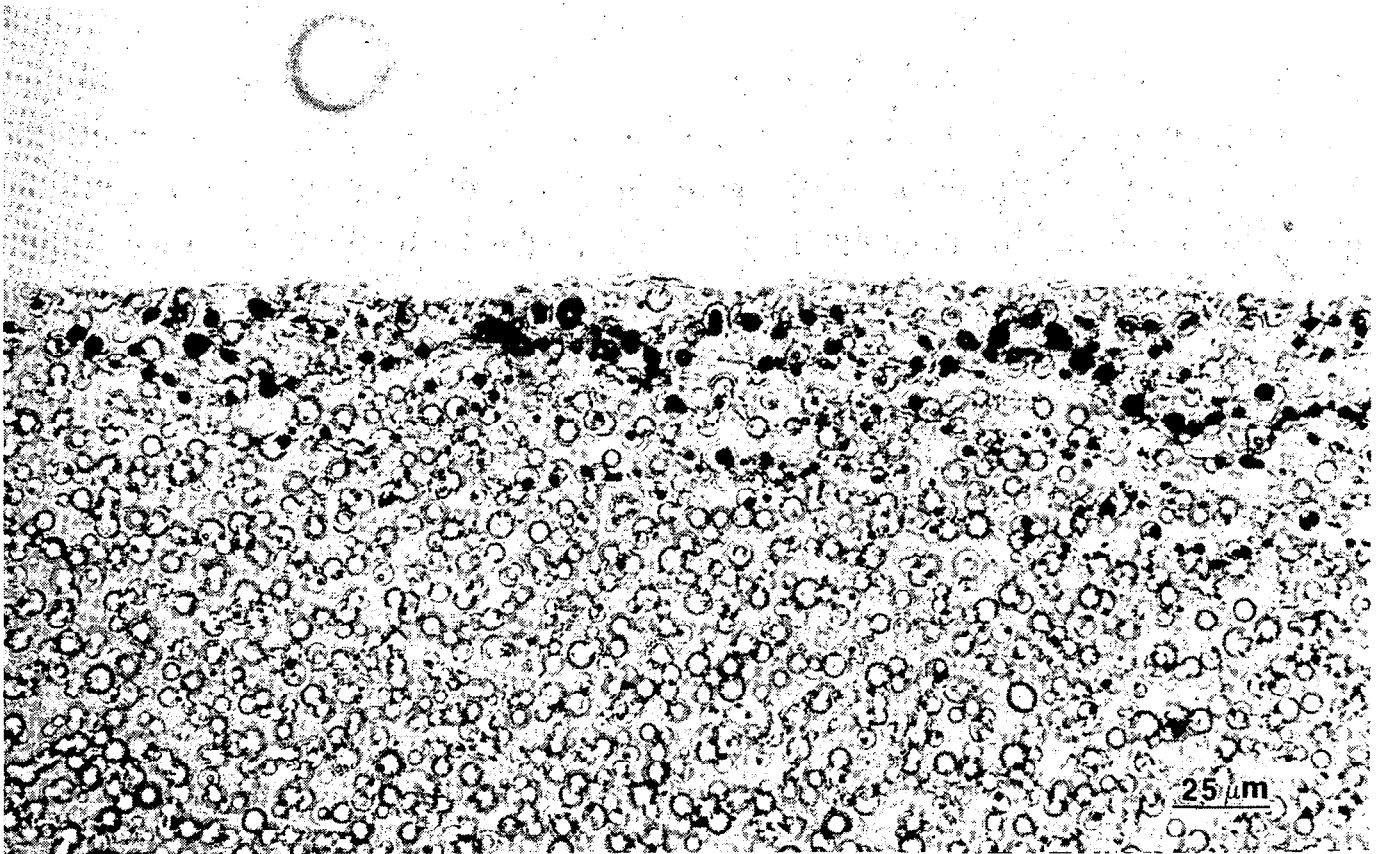
7.3 Higher Magnification OM of Subsurface Damage in the SEN-3PB Stress

Whitened Region of 828-8(20)



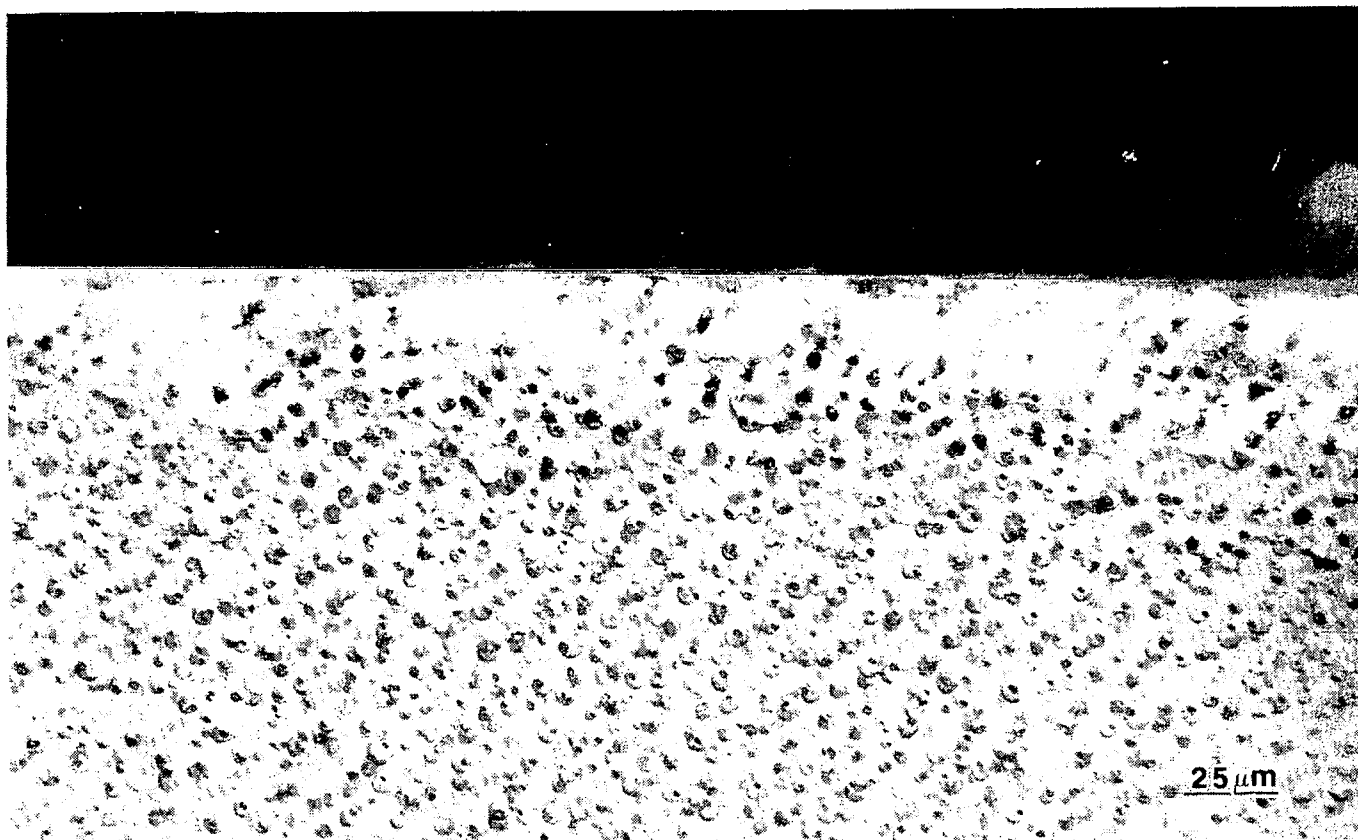
7.4 Higher Magnification OM of Subsurface Damage in the SEN-3PB Stress

Whitened Region of 828-BPA(24)-8(15)

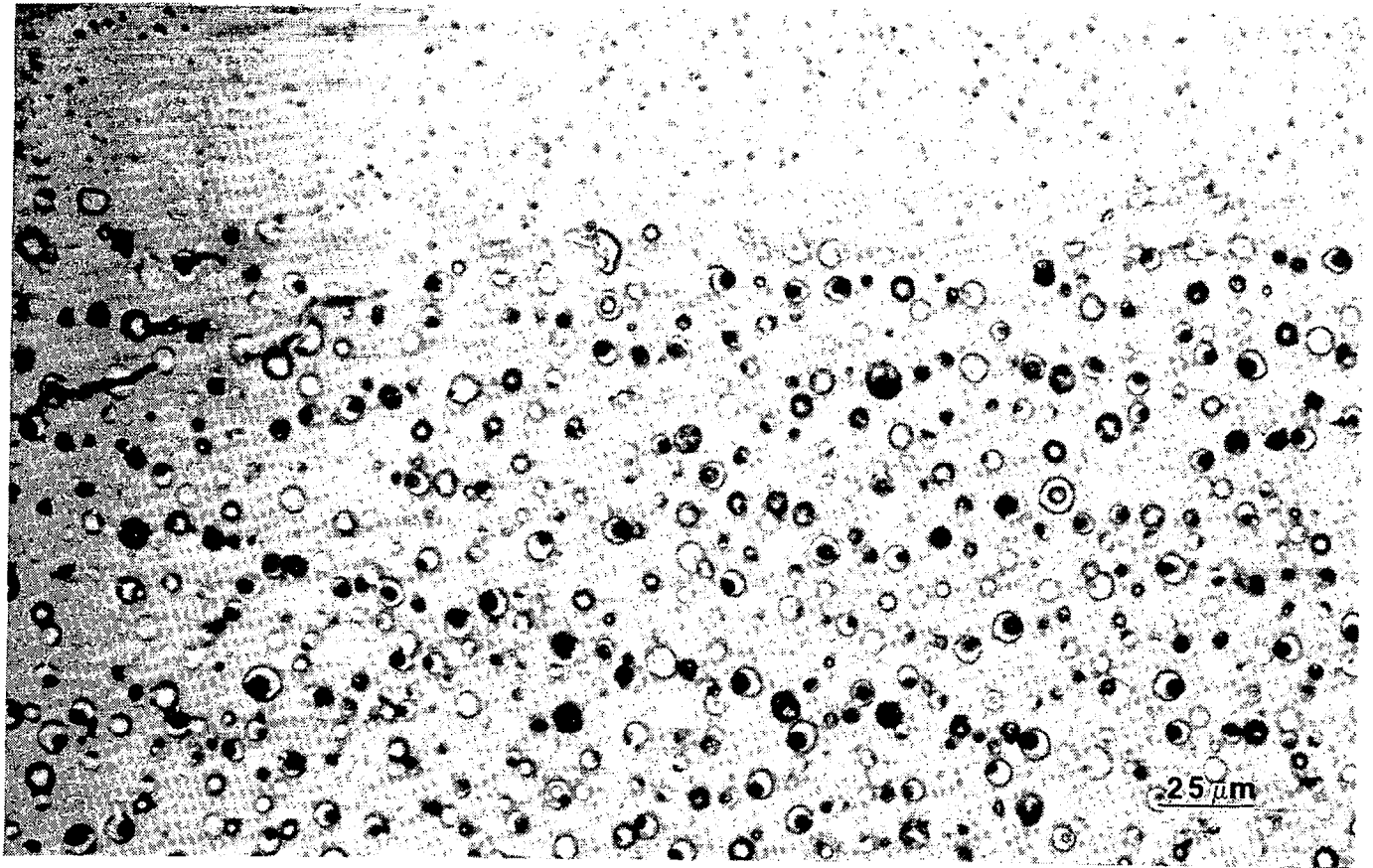


**7.5 Transmission Optical Micrograph of the Subsurface Damage of Fracture:**

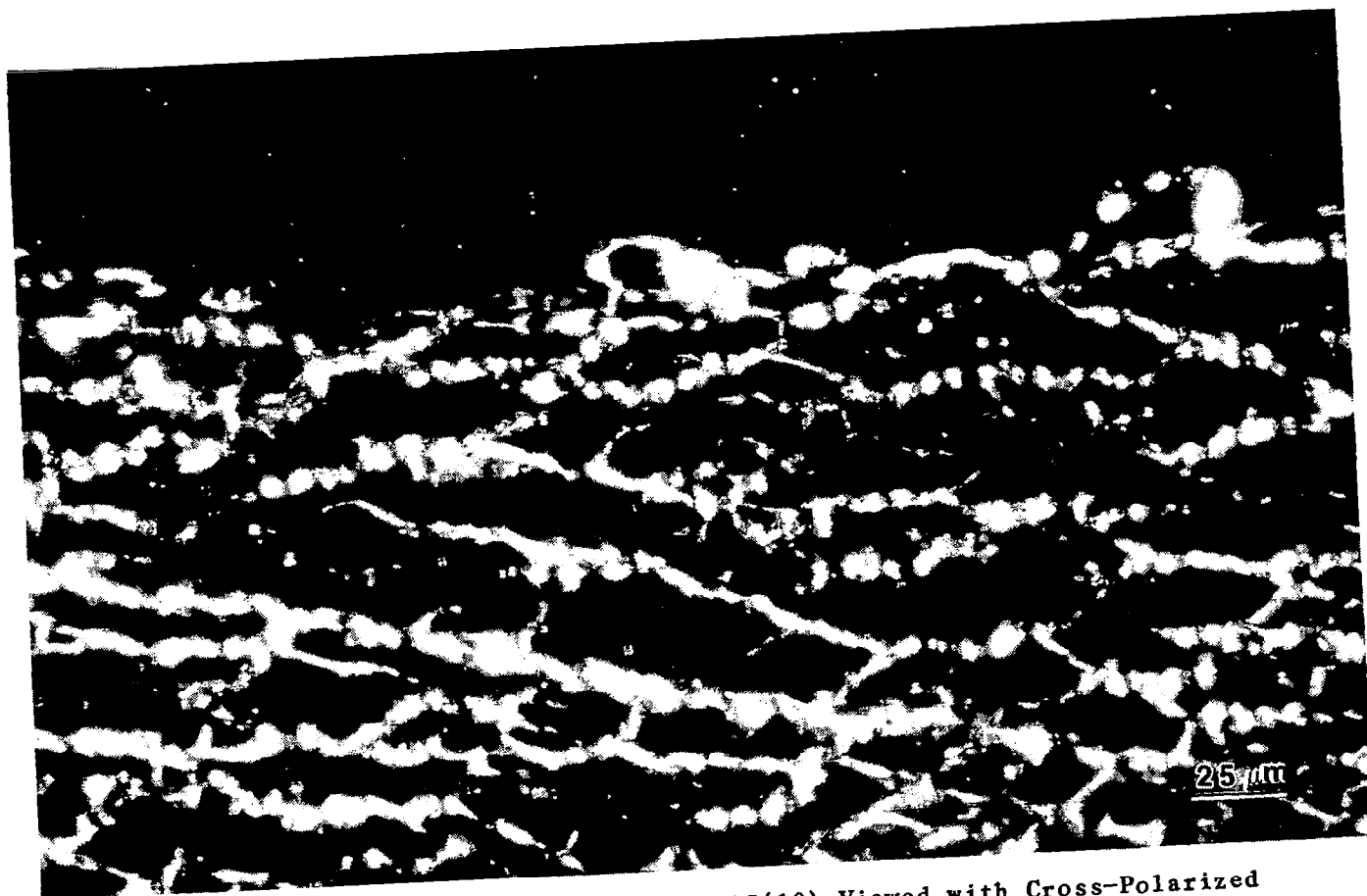
**(a) SEN-3PB Specimen of 828-15(10) Viewed in Bright Field**



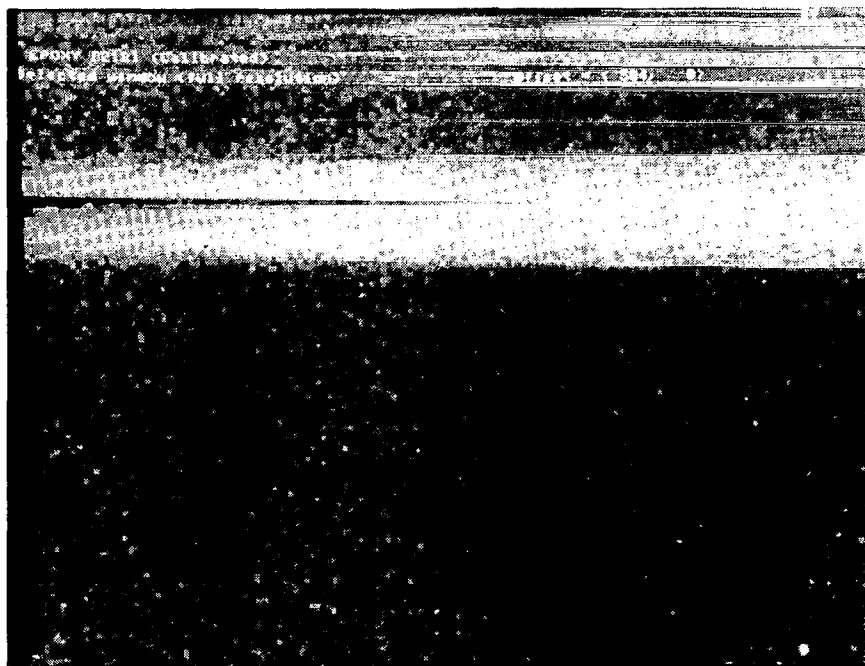
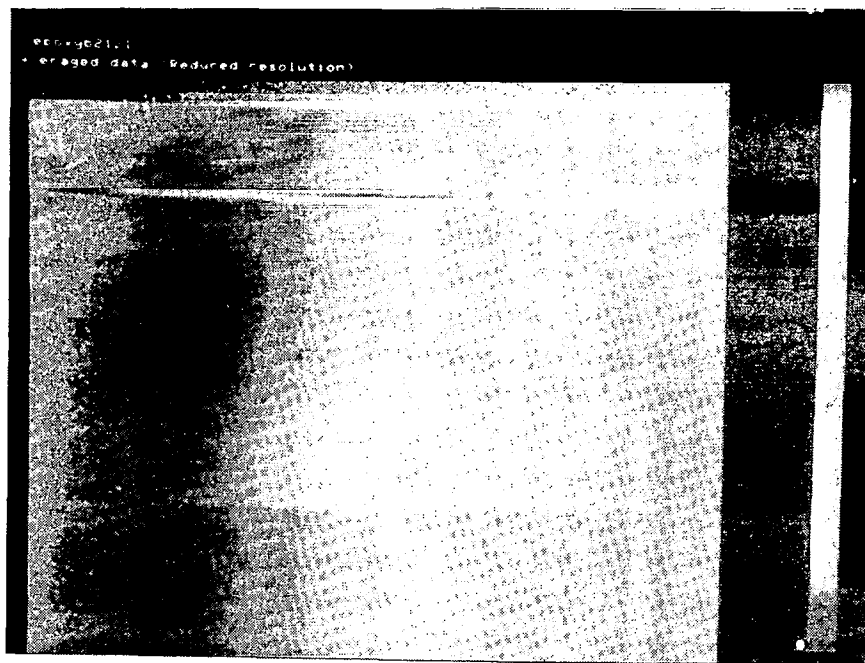
(b) SEN-3PB Specimen of 828-15(10) Viewed with Cross-Polarized Light.



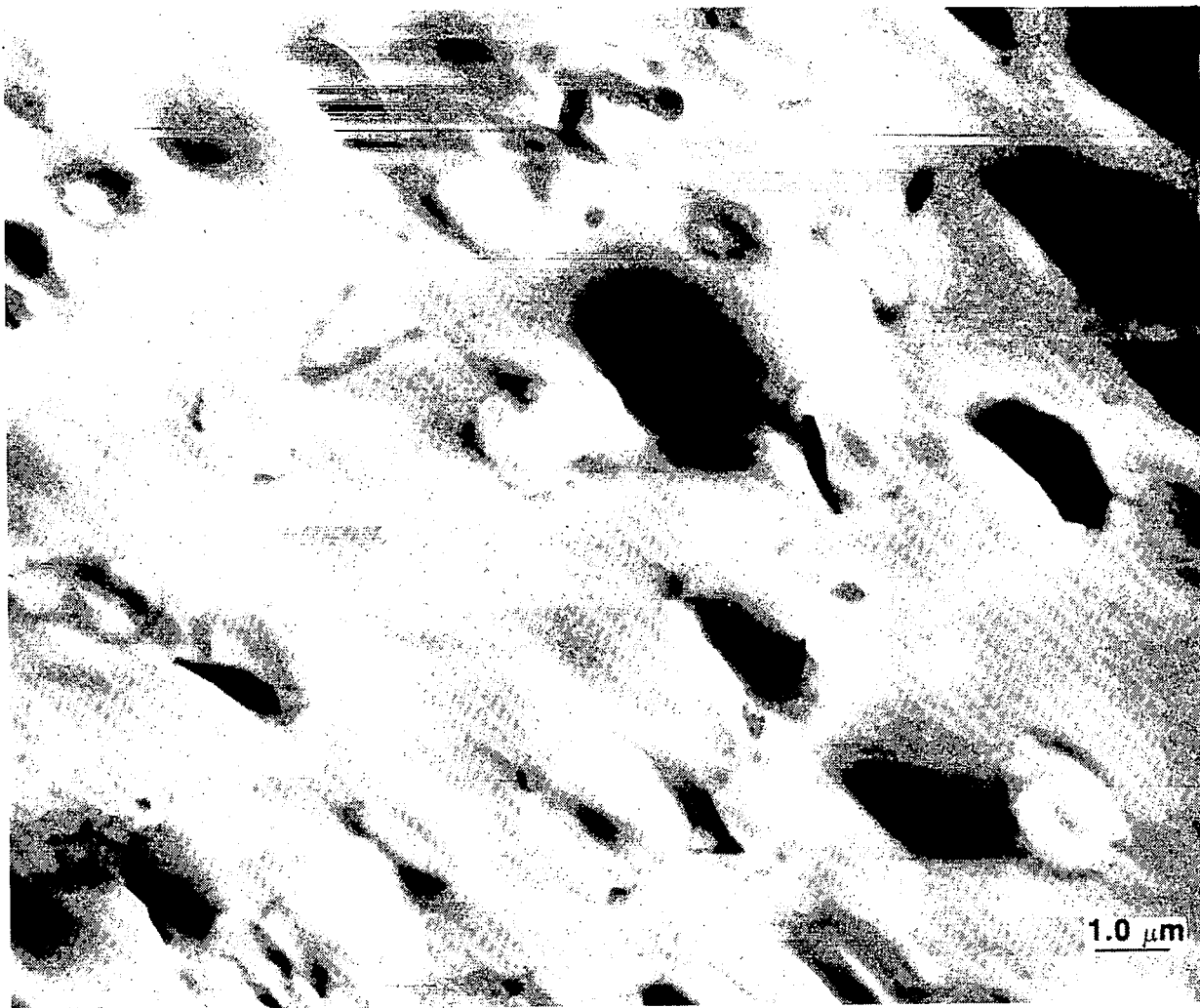
(c) Volume Dilation Specimen of 828-15(10) Viewed in Bright Field.



(d) Volume Dilation Specimen of 828-15(10) Viewed with Cross-Polarized Light.



7.6 SAXS of Fractured Tensile Specimen of 828-8(10) (a)  
Reduced Resolution (b) Full Resolution



7.7 TEM of typical sub-surface damage zone.

## 8. GENERAL SUMMARY AND DISCUSSION

With the exception of the 828-13 system, the rubber-modified epoxies have been shown to be toughened over the neat resins by over an order of magnitude. The toughening effect was made possible by the formation of a two phase system, the rubber having precipitated out of the mixture during the polymerization process. The difference in the solubility and molecular weight of the rubbers caused the rubber to precipitate out into spherical particles with diameters ranging between 0.1 and 10  $\mu\text{m}$ . The toughness was found to be primarily a function of rubber content. The effect of rubber particle size was, on the whole, not significant. On the other hand, the BPA-modified matrix, which has a slightly lower modulus and yield stress, produced small but significant increases in toughness. At room temperature and above, the uniaxial stress-strain behavior of the neat resins exhibited a surprising amount of ductility. These materials yielded with a maximum in the true stress, followed by intrinsic strain softening. The strain softening was caused by the formation of shear bands.(41,42) The localization of the shear deformation showed up in the volume strain as a maximum. This maximum occurred at increasingly high strains as the strain rate increased. The retardation of the shear localization process by increasing strain rates is undoubtedly an important factor in the brittleness of the neat resins in crack propagation. While the shear localization process was retarded, the volume strain increased. The bulk strain energy increased roughly as the square of the volume strain, so the inability of the shear localization process to take place exacts a penalty in the building up of bulk energy. Thus, any mechanism that facilitates the shear localization process, or, alternatively, dissipates the bulk strain energy, would enhance the toughness. The rubber particles

appear to do both.

The room temperature tensile volume dilatation of the two-phase rubber-modified epoxies appear to be very similar to the neat resins at low rates. The rubber particles definitely enhance the shear localization process, as evidenced by the maximum in the volume strain following Poisson's effect dilatation. At sufficiently high rates, however, when the neat resin typically dilatates at a nearly constant rate almost up to the yield point, the rubber particles cause the material to expand at a higher rate than the neat resin. SEM micrographs suggest that this expansion is caused by cavitation of the rubber particles. The cavitation is followed by the onset of the shear localization process, which would not have taken place in the neat resin under the same conditions. Thus, the rubber particles dissipate the bulk strain energy by cavitation; and, at the same time, the shear strain energy is allowed to build up to the point where shear yielding can take place. The voids left behind by the cavitated rubber particles act further as stress concentrators. Theoretical model calculations show that they reduce the octahedral shear stress to yield (46) and they grow and promote the formation of plastic zones between voids;(22) shear band formation is enhanced in such a voidy solid.(53,54) All these theoretical predictions are consistent in the main with the observations made here.

In the fracture of these materials containing sharp cracks, the stress configuration is somewhat different from the tensile case. A zone of high hydrostatic tension exists ahead of the crack tip, and the crack eventually propagates along a plane of maximum hydrostatic tension. The hydrostatic tension causes rapid cavitation of the rubber and growth of the resultant voids, as shown by fracture surface SEM's. In the tensile dilatometric studies,

cavitation of the rubber occurred at a tensile strain of ca. 2-3%, and the maximum additional volume strain caused by the cavitation was but a fraction of a percent. Under the influence of hydrostatic tension, however, these voids grew generally by 20-40% in diameter and, in the extreme case of the 828-15(20) system, by nearly 300%. This rapid void growth is consistent with theoretical calculations, which show that void growth rate increases exponentially with increasing hydrostatic tension.(44,45) However, beneath the plane directly ahead of the crack plane, the hydrostatic tension rapidly diminishes, resulting in a concomitant rapid decrease in the void size. This may be the reason why the OM and TEM micrographs of the sub-surface plastic zones do not show dramatic dilatation of the rubber particles. Another contributing factor may be that the micrographs are of specimens that had undergone post-fracture elastic recovery. In any case, it is reasonable to surmise from the tensile dilatometry results that a zone of voids is formed ahead of the crack tip as soon as stress is applied to open up the crack faces. This voided zone, part of which may have been unavoidably created by the process of introducing the sharp crack, blunts the crack, causing it to behave as if it had a much larger crack tip radius. This blunt notch, upon the application of further tension, causes an even larger plastic zone to form. The shear bands are clearly observable as the birefringent bands in OM. Thus, a large volume of material above and below the crack plane is caused to undergo plastic flow. It is probably the creation of this plastic zone that is the principal toughening mechanism. The crack, in the meantime, propagates through the voided plane because the ligament between the voids can no longer support the tensile stress. The fracture process described above is schematically depicted in Figure 8.1.

The proposal advanced here, that plastic zone formation is the principal toughening mechanism, finds support also in the work by Bascom and coworkers (7) on the fracture toughness of rubber-modified epoxy adhesive joints. These workers found that the fracture toughness of epoxy adhesive joints is strongly dependent on the thickness of the joint. When the joint thickness is too small, the fracture toughness is low. Maximum toughness is attained when the joint thickness is about the same as the height of the plastic zone.

A myriad of deformation mechanisms have been observed in these studies: the rubber particles cavitate and fracture; the resultant voids in the matrix grow and coalesce; the matrix produces SAXS scattering patterns similar to those created by crazes; finally, the matrix also forms shear bands. The contributions to toughness of these mechanisms is now discussed.

The rubber particles undoubtedly also stretch and tear, but, at least in the systems studied here, not to the extent observed by Kunz and Beaumont.(1,2,34) By themselves these rubber particles probably absorb relatively little energy--even Kunz and Beaumont's model calculations show a contribution of only several hundred  $\text{J/m}^2$  at high rubber contents. Nevertheless, the particles appear to play an important role. They first enhance shear localization by acting as stress concentrators. Then, as bulk strain energy increases, cavitation takes over and dissipates the energy, making further shear localization possible. Although the different types of rubber produce particles of different sizes, distributions and internal structures, the role played by them appear to be quite similar. No major effects due to particle size differences have been observed. This result contradicts the conclusions of Sultan and McGarry(5). But it should be pointed out that the smallest rubber particles they studied were  $0.040\text{ }\mu\text{m}$  in diameter, smaller than those

studied here. The 828-BPA(24)-8(15) system, which has a bimodal distribution in rubber particle sizes, shows high toughness; but the supposed extra toughness enhancement, most recently studied by Bascom et al., (9) is not conclusively demonstrated here.

The matrix scatters X-rays, and the scattering behavior is similar to that produced by crazes. There might well be stress activated craze-like density fluctuations. However, crazes in the conventional thermoplastic sense have not been found in these studies. They have not been found to any significant extent in the dilatometric studies, nor by using TEM techniques that in the past have been successful in locating crazes. Certainly, no evidence for massive crazing exists. These results contradict the conclusion of Bucknall and Yoshii(10), Sultan and McGarry(5), and Riew and co-workers (23,24). It should be emphasized that the possibility of crazing in cross-linked epoxies is not being discounted by the foregoing discussion. Based on available evidence, crazing is not an important energy dissipation mechanism in the toughening of these epoxies.

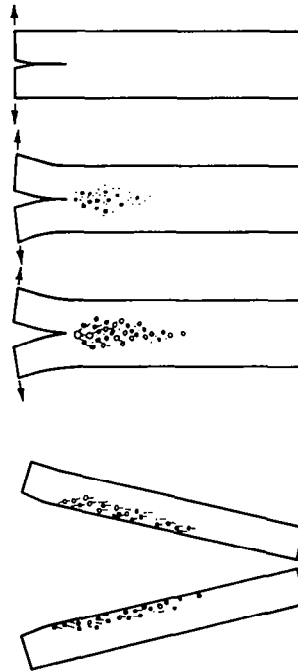
The difficult process of nucleating voids in a solid has apparently been facilitated by the presence of the rubber particles. Once formed the voids grow and dissipate bulk strain energy. They also concentrate stresses, and depending on the stress configuration and volume fraction cause either ductile fracture of the ligaments between adjacent voids aligned perpendicular to the major principal tensile stress, or cause shear localization (shear banding) to occur. They enable the formation of large plastic zones, which probably absorb most of the energy. These conclusions are in accord with those of Bascom and co-workers(6-8).

Ultimately, the toughness of the material lies in the ease with which the matrix can deform in shear, though not necessarily to form narrow and sharp shear bands. It seems reasonable to state that one helpful property would be a high Poisson's ratio, for then a higher proportion of the strain energy goes into shear. A high Poisson's ratio in a real solid does not mean that it is incompressible, merely that the bulk modulus is high relative to the shear modulus. It is not clear how the molecular structure of a glass relates to its Poisson's ratio. The effect of cross-link density, though, is perhaps easier to predict. Increasing the cross-link density should increase the bulk modulus much less rapidly than the shear modulus, thus, a lower cross-link density appears to be preferred from this standpoint.

The shear banding process is seen to be strongly influenced by the strain rate. It is, therefore, most likely related to a viscoelastic relaxation that has not too broad a relaxation time spectrum. Such a relaxation would likely have as its origin some sort of molecular rearrangement process that can be stress activated. It is interesting to note that if such an activated process can be described by an activation energy, then the higher the activation energy, the less sensitive the process would be to the strain rate or temperature. If the Epon 828 resin satisfied this requirement, then the low temperature brittleness might be avoidable.

#### ACKNOWLEDGEMENTS

The authors wish to acknowledge the generosity of Dr. K. Riew of B.F. Goodrich, Co., for providing the liquid rubbers and a plaque mold free of charge. Mr. C. Lizak kindly provided first hand information on the preparation of the epoxy plaques.



**8.1 Schematic representation of the crack blunting process.**

The authors also wish to thank Dr. S. Kunz of Sandia Laboratories for providing two copies of her PhD thesis and for samples of rubber-modified epoxy plaques. Dr. R. LaGasse of Sandia Laboratories also provided epoxy plaques which were used in preliminary studies.

The authors are indebted to numerous scientists here at the General Electric Research and Development Center: Dr. D.G. LeGrand, for SAXS measurements and illuminating discussions; Mrs. V.H. Watkins, Drs. S.Y. Hobbs, E. Hall, and Messrs A. Holik and J. Grande for advice, help and discussions on microscopy techniques and results; and Dr. M.T. Takemori and Ms. M.A. Maxwell for stimulating discussions.

Dr. C.B. Bucknall of the Cranfield Institute of Technology generously gave of his invaluable experience and advice.

Dr. Howard Price was the Contract Monitor during the first phase of this work. The authors wish to thank him for his advice and encouragement.

Finally, the authors wish to thank Dr. N. Johnston of NASA-Langley, the Contract Monitor of this work, for his encouragement, stimulating questions, understanding, and patience.

#### REFERENCES

1. S. Kunz, "The Toughening of Epoxy-Rubber Particulate Composites", Ph.D Thesis, Churchill College, Cambridge (1978).
2. S. Kunz-Douglass, "A Model for the Toughness of Epoxy-Rubber Particulate Composites", P.W.R. Beaumont and M.F. Ashby, J. Mater. Sci., 15, 1109 (1980).

3. W.D. Bascom and D.L. Hunston, "Adhesive Fracture Behavior of CTBN-Modified Epoxy Polymers", Int. Conf. Toughening of Plastics, London 1978.
4. J.N. Sultan, R.C. Laible and F.J. McGarry, "Microstructure of Two-Phase Polymers", Appl. Polymer Symp. 16, 127 (1971).
5. J.N. Sultan and F.J. McGarry, "Effect of Rubber Particle Size on Deformation Mechanisms in Glassy Epoxy", J. Polym. Sci., 13, 29 (1973).
6. W.D. Bascom, R.L. Cottingham, R.L. Jones and P. Peyser, "The Fracture of Epoxy and Elastomer Modified Epoxy Polymers in Bulk and as Adhesives", J. Appl. Polym. Sci., 19, 2545 (1975).
7. W.D. Bascom and R.L. Cottingham, "Effect of Temperature on the Adhesive Fracture Behavior of an Elastomer", J. Adhesion, 7, 333 (1976).
8. W.D. Bascom, R.L. Cottingham, and C.O. Timmons, "Fracture Reliability of Structural Adhesives", J. Appl. Sci.: Appl. Polym. Symp., 32, 165 (1977).
9. W.D. Bascom, R.Y. Ting, R.J. Moulton, C.K. Riew and A.R. Siebert, "The Fracture of an Epoxy Containing Elastomeric Modifiers", J. Mater. Sci., 16, 2657 (1981).
10. C.B. Bucknall and T. Yoshii, "Relationship Between Structure and Mechanical Properties in Rubber-Toughened Epoxy Resins", Brit. Polymer J., 10, 53 (1978).
11. C.B. Bucknall and T. Yoshii, "Relationships Between Structure and Mechanical Properties in Rubber-Modified Epoxy Resins", 3rd Int. Conf. on Def., Yield and Fracture Polymers, Cambridge 1976.

12. R.N. Haward and D.R.J. Owen, "The Yielding of a Two-Dimensional Void Assembly in the Organic Glass", J. Mater. Sci., 8, 1136 (1973).
13. E.H. Andrews, Chapter 7 in "Physics of Glassy Polymers", R.N. Haward, ed., J. Wiley and Sons, New York, 1973.
14. S. Rabinowitz and P. Beardmore, "Craze Formation and Fracture in Glassy Polymers", CRC Critical Rev. in Macromol. Sci., 1, 1972, p. 1.
15. R.P. Kambour, "A Review of Crazing and Fracture in Thermoplastics", Macromol. Rev., 7, 134 (1971).
16. E.J. Kramer, p. 55 in "Developments in Polymer Fracture-1", E.H. Andrews, ed., Applied Science Pub., London, 1979.
17. S.S. Sternstein, "Mechanical Properties of Glassy Polymers", in "Treatise on Materials Science and Technology", Vol. 10, J.M. Schultz, ed., Academic Press, New York (1977), p. 541.
18. D.G. LeGrand, R.P. Kambour, and W.R. Haaf, "Low Angle X-Ray Scattering From Crazes and Fracture Surfaces in Polystyrene", J. Polym. Sci., Part A-2, 10, 1565 (1972).
19. S.S. Sternstein and L. Ongchin, ACS Polymer Prep. 10(2), 1117 (1969).
20. C.B. Bucknall, "Toughened Plastics", Applied Science, London, 1977.
21. R.W. Truss and G.A. Chadwick, "The Tensile Deformation Behavior of a Transparent ABS Polymer", J. Mater. Sci., 11, 111 (1976).
22. A. Needleman, "Void Growth in an Elastic-Plastic Medium", J. Appl. Mech., Trans. ASME, 964 (1972).

23. C.K. Riew, E.H. Rowe and A.R. Siebert, "Rubber Toughened Thermosets", ACS Adv. Chem. Ser., 154, 326 (1976).
24. E.H. Rowe, "Developments in Improved Crack Resistance of Thermoset Resins and Composites", p. 23-1 in Proceedings of Int. Conf. Toughening Plastics, London, 1978.
25. H. Breuer, F. Haaf and J. Stabenow, "Stress Whitening and Yielding Mechanisms of Rubber-Modified PVC", J. Macromol. Sci-Phys., B14(3), 387 (1977).
26. R. Ramsteiner, "Structural Changes During The Deformation of Thermoplastics in Relation to Impact Resistance", Polymer, 20, 839 (1979).
27. M.A. Maxwell and A.F. Yee, "The Effect of Strain Rate on the Toughening Mechanisms of Rubber-Modified Plastics", Polym. Engineering Sci., 21, 205 (1981).
28. A.F. Yee, W.V. Olszewski, and S. Miller, "Plane Strain and the Brittleness of Plastics", ACS Adv. Chem. Ser. 154, 97 (1976).
29. J. Mijovik and J.A. Koutsky, "Correlation Between Nodular Morphology and Fracture Properties of Cured Epoxy Resins", Polymer, 20, 1095 (1979).
30. R.J. Young, p. 183 in "Developments in Polymer Fracture-1", E.H. Andrews, ed., Applied Science Pub., London 1979.
31. J. Lilley and D.G. Holloway, "Correspondence: Crazeing in Epoxy Resins", Phil. Mag., 28, 215 (1973).
32. R.J. Morgan and J.E. O'Neal, p. 289 in "Chemistry and Properties of

- Crosslinked Polymers", S.S. Labana, ed., Academic Press, New York 1977.
33. A.C. Meeks, "Fracture and Mechanical Properties of Epoxy Resins and Rubber-Modified Epoxy Resins", *Polymer*, 15, 675 (1974).
  34. S.C. Kunz and P.W.R. Beaumont, "Low-Temperaure Behavior of Epoxy-Rubber Particulate Composites", *J. Mater. Sci.*, 16, 3141 (1981).
  35. E. Plati and J.G. Williams, "The Determination of the Fracture Parameters for Polymers in Impact", *Polymer Engineering and Science*, 15,, 470 (1975).
  36. J.G. Williams and M.W. Birch, "The Impact Testing of Polymers - A Reassessment", *Proc. 4th Int. Conf. Fracture*, Vol. 1, Part IV, p. 501, University of Waterloo, Canada 1977.
  37. H.R. Brown, "The Relationship Between Yield Point and Modulus For Glassy Polymers", *J. Material Sci.*, 8, 941 (1973).
  38. L.C. Cessna, Jr., and S.S. Sternstein, in "Fundamental Phenomena in the Materials Sciences", L.J. Bonis, J.J. Duga, and J.J. Gilman, eds., Vol. 4, pp. 45-79. Plenum Press, New York 1967.
  39. E.E. Underwood, p. 109 in "Quantitative Stereology", Addison Wesley Pub. Co., Reading, Mass, 1970.
  40. J.A. Sayre, R.A. Assink, and R.R. Lagasse, "Characterization of the Phase Structure of an Amide Cured Ruber Modified Epoxy", *Polymer*, 22, 87 (1981).
  41. P.B. Bowden, "A Criterion for Inhomogeneous Plastic Deformation", *Phil*

Mag., 22, 455 (1970).

42. P.B. Bowden, in "Physics of Glassy Polymers", R.N. Haward, ed., J. Wiley and Sons, New York 1973.
43. A. Melander and U. Staklberg, "The Effect of Void Size and Distribution on Ductile Fracture", Int. J. Fracture, 16, 431 (1980).
44. F.A. McClintock, "A Criterion for Ductile Fracture by the Growth of Holes", J. Appl. Mech., 35, 363 (1968).
45. J.R. Rice and D.M. Tracy, "On the Ductile Enlargement of Voids in Triaxial Stress Fields", J. Mech. Phys. Solids, 17, 201 (1969).
46. A.L. Gurson, "Continuum Theory of Ductile Rupture by Void Nucleation and Growth Part I: Yield Criteria and Flow Rules For Porous Ductile Media", J. Engineering Mat. Tech. Trans., ASME, 99, 2 (1977).
47. L.T. Manzione and J.K. Gillham, "Rubber-Modified Epoxies I. Transitions and Morphology", J. Appl. Polym. Sci., 26, 889 (1981).
48. S.Y. Hobbs and V.H. Watkins, "The Use of Chemical Contrast in the SEM Analysis of Polymeric Blends", J. Poly. Sci., 20, 651 (1982).
49. P.B. Lindley, "The Stiffness of Rubber Springs", Aust. Plast. Rubber J., 22, (260), 11 (1967).
50. D. Heikens, S. Kirksjoerdsma, and W. Jan Coumans, "A Mathematical Relation Between Volume Strain, Elongational Strain and Stress in Homogeneous Deformation, J. Mater. Sci., 16, 429 (1981).

51. A.S. Tetelman and A.J. McEvily, Jr., "Fracture of Structural Materials", J. Wiley and Sons, New York, 1967.
52. A.S. Holik, R.P. Kambour, S.Y. Hobbs, and D.G. Fink, "Grinding and Polishing Techniques for Thin Sections of Polymeric Materials for Transmission Light Microscopy", Microstructural Sci., 7, 357 (1979).
53. H. Yamamoto, "Conditions for Shear Localization in the Ductile Fracture of Void Containing Materials", Int. J. Fracture, 14, 347 (1978).
54. V. Tvergaard, "Influence of Voids on Shear Band Instabilities Under Plain Strain Conditions", Int. J. Fracture, 17, 389 (1981).

1. Report No. NASA CR-3718		2. Government Accession No.		3. Recipient's Catalog No.	
4. Title and Subtitle TOUGHENING MECHANISM IN ELASTOMER-MODIFIED EPOXY RESINS - PART 1				5. Report Date August 1983	
				6. Performing Organization Code	
7. Author(s) A.F. Yee and R.A. Pearson				8. Performing Organization Report No. 83-SRD-023	
9. Performing Organization Name and Address General Electric Company, Corporate Research and Development P.O. Box 8 Schenectady, NY 12301				10. Work Unit No.	
				11. Contract or Grant No. NAS1-16132	
12. Sponsoring Agency Name and Address National Aeronautics and Space Administration Washington, D. C. 20546				13. Type of Report and Period Covered Contractor Report (June 23, 1980-Dec. 31, 1981)	
				14. Sponsoring Agency Code	
15. Supplementary Notes NASA/Langley Technical Monitor: Norman J. Johnston Final Report on Part 1 only; a subsequent volume will cover Part 2 research.					
16. Abstract Several plaques of Epon 828, cured with piperidine, modified with Hycar <sup>R</sup> CTBN 1300X8, Hycar <sup>R</sup> CTBN 1300X13, and Hycar <sup>R</sup> CTBN 1300X15, and in some cases modified with bisphenol "A" (BPA), yielded properly toughened epoxies with rubber particle diameters ranging from 0.1 to 10 $\mu$ m. Fracture toughness experiments indicate that toughness was more a function of rubber content than the rubber particle size. Tensile volumetric behavior of the neat resin exhibits two regions: an initial region where the increase in volume strain was due to the Poisson's effect, and a second region where a slower rate of increase in volume strain was due to shear deformation. Tensile volumetric deformation of an elastomer-modified epoxy exhibits the same type of behavior to that of the neat resin at low rates ( $<3.2 \times 10^{-2}$ sec <sup>-1</sup> ). But at very high strain rates, which correspond more closely to the strain rates at the crack tip, there exists an increase in volume strain beyond the Poisson's effect. TEM, SEM and OM studies indicate that the rubber particles had voided. When a thin section from the deformed region is viewed under crossed-polarized light, shear bands are seen connecting voided rubber particles. From this information cavitation and enhanced shear band formation is proposed as the toughening mechanism.					
17. Key Words (Suggested by Author(s)) Epoxy, Rubber-modified epoxy, impact, fracture toughness, epoxy mechanical properties, polymer mechanical properties			18. Distribution Statement Unclassified - Unlimited  Subject Category 27		
19. Security Classif. (of this report) Unclassified		20. Security Classif. (of this page) Unclassified		21. No. of Pages 130	
				22. Price* A07	